

Perovskites for Next-Generation Optical Sources

Li Na Quan, Barry P. Rand, Richard H. Friend, Subodh Gautam
Mhaisalkar, Tae-Woo Lee, Edward H. Sargent

Version Post-print/accepted manuscript

Citation Quan LN, Rand BP, Friend RH, Mhaisalkar SG, Lee TW, Sargent EH.
(published version) Perovskites for Next-Generation Optical Sources. Chemical reviews.
2019 Apr 25.

Publisher's Statement This is the peer reviewed version of the following article:
Quan LN, Rand BP, Friend RH, Mhaisalkar SG, Lee TW, Sargent EH.
Perovskites for Next-Generation Optical Sources. Chemical reviews.
2019 Apr 25.

How to cite TSpace items

Always cite the **published version**, so the author(s) will receive recognition through services that track citation counts, e.g. Scopus. If you need to cite the page number of the **author manuscript from TSpace** because you cannot access the published version, then cite the TSpace version **in addition to** the published version using the permanent URI (handle) found on the record page.

This article was made openly accessible by U of T Faculty.
Please [tell us](#) how this access benefits you. Your story matters.



Perovskites for Next-Generation Optical Sources

Li Na Quan¹, Barry P. Rand², Richard H. Friend³, Subodh Gautam Mhaisalkar⁴,

Tae-Woo Lee⁵, Edward H. Sargent¹

1. Department of Electrical and Computer Engineering, University of Toronto, 10 King's College Road, Toronto, Ontario M5S 3G4, Canada.
2. Department of Electrical Engineering and Andlinger Center for Energy and the Environment, Princeton University, Princeton, NJ 08544, USA.
3. Cavendish Laboratory, University of Cambridge, JJ Thomson Avenue, Cambridge CB3 0HE, United Kingdom.
4. Energy Research Institute, Nanyang Technological University, Research Techno Plaza, X-Frontier Block, Level 5, 50 Nanyang Drive, 637553 Singapore.
5. Department of Materials Science and Engineering, Research Institute of Advanced Materials, Seoul National University, 1 Gwanak-ro, Gwanak-gu, Seoul 08826, Republic of Korea.

E-mail: ted.sargent@utoronto.ca

Next-generation displays and lighting technologies require efficient optical sources that combine brightness, color purity, stability, substrate flexibility and, in certain applications. Metal halide perovskites are potentially used in a wide range of applications, for they possess excellent charge transport, bandgap tunability and – in the most promising recent optical source materials – intense and efficient luminescence. This review links metal halide perovskites' performance as efficient light emitters with their underlying materials electronic and photophysical attributes.

CONTENTS

- 1. Introduction: Overview of perovskites and their optoelectronic properties**
- 2. Chemical and Structural Diversity in Perovskites**
 - 2.1 Effect of Organic and Inorganic Compounds

2.2 Effect of Dimensionality in Perovskites

2.2.1 Three-Dimensional Perovskites

2.2.2 Two-Dimensional Perovskites

2.2.3 Zero-Dimensional Perovskites

2.3 Lead-Free Perovskites

3. Perovskite Photophysical Properties

3.1 Recombination Mechanisms

3.2 Exciton and Free Carrier Dynamics

3.3 Photoluminescence Quantum Yield

4. Perovskite Light-Emitting Diodes (LEDs)

4.1 Perovskite Material Engineering for LEDs

4.1.1 Modulating Dimensionality in Perovskite for LEDs

4.1.2 Colloidally-Synthesized Perovskite Nanocrystals for LEDs

4.2 Engineering Perovskite LEDs Towards High Efficiency

4.2.1 Engineering Interfacial Layers

4.2.2 Comparison of Perovskite LED with QLED and OLEDs

4.3 Stability of Perovskite LEDs

4.3.1 Status and Mechanisms Underpinning Stability in Perovskite LEDs

4.3.2 Strategies to Improve LED Stability

5. Perovskites for Lasing

5.1 Optical Amplification Using Perovskites

5.1.1 Original Reports of Perovskite Lasing

5.1.2 Effects of Perovskite Crystal Structures

6. Conclusions and Outlook

1. Introduction: Overview of perovskites and their optoelectronic properties

Hybrid perovskites are an emerging class of semiconducting materials exhibiting outstanding opto-electronic properties. The general chemical formula for perovskite is ABX_3 , in which A and B are cations and X are anions that octahedrally coordinate to B. The large A-site cations and the smaller B-site cations, allowing $[BX_6]^{4-}$ octahedra to corner-share in a 3D framework, with the A-site cations located in the framework cavities. The canonical perovskite material is calcium titanate, discovered in by Gustav Rose in 1839 and named in honour of Lev Perovski (1792-1856).

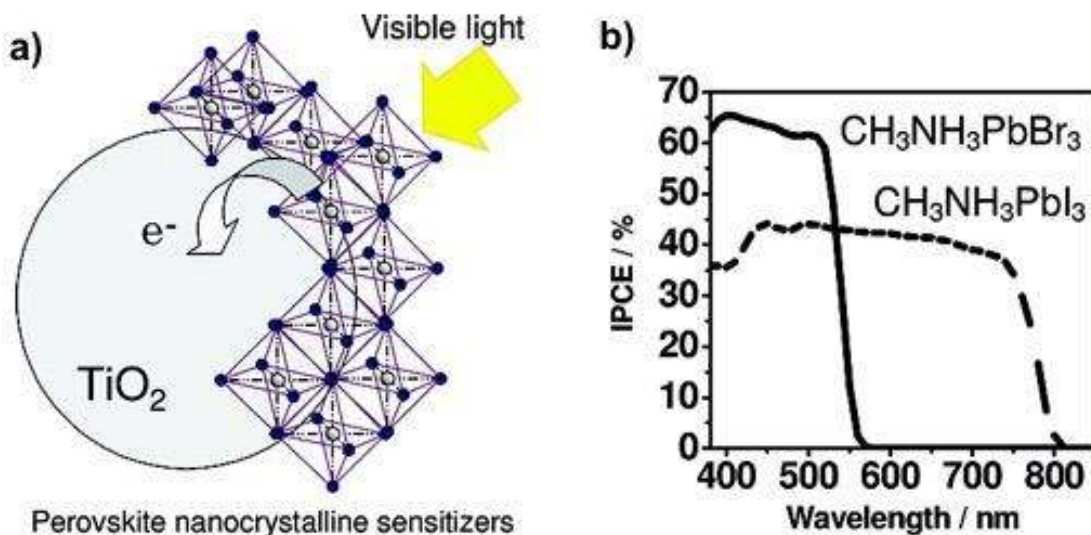


Figure 1. Perovskites a sensitizers of TiO_2 in solid-state dye-sensitized solar cells. b) Internal power conversion efficiency spectra of $CH_3NH_3PbBr_3$ and $CH_3NH_3PbI_3$ ¹. Reproduced from ref 1.

Copyright 2009, American Chemical Society.

Diverse perovskite materials exhibit ferroelectricity, superconductivity and magnetoresistance, to name a few of their intriguing properties. Metal halide perovskites exhibit

high absorption coefficients (in $\text{CH}_3\text{NH}_3\text{PbI}_3$ of order 10^4 cm^{-1}), high charge-carrier mobilities (exceeding $10 \text{ cm}^2 \text{ V}^{-1} \text{ s}^{-1}$), long minority carrier diffusion lengths ($1 \text{ }\mu\text{m}$ and greater), and low trap densities (lower than 10^{16} cm^{-3}). These impressive properties make halide perovskites excellent semiconductors for solar cells. Since Miyasaka and co-workers introduced halide perovskites in liquid-electrolyte solar cells in 2009, thousands of researchers have turned their attention to perovskite solar cells (PSCs) (Figure 1)¹⁻⁶. The certified power conversion efficiency of PSCs has risen in nine years from approximately 3% to greater than 23%⁷ (Figure 2).

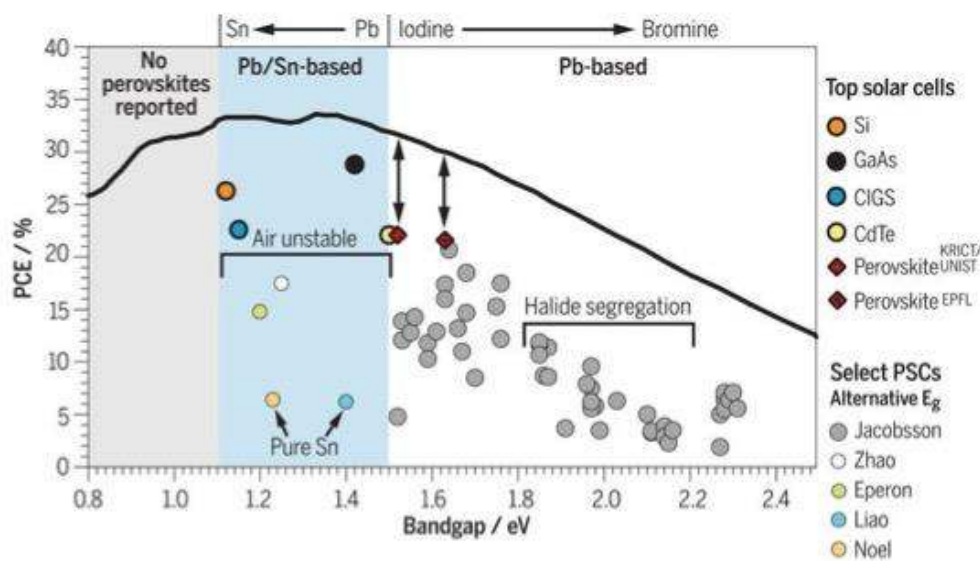


Figure 2. State-of-art perovskite solar cell efficiencies as a function of bandgap energy⁸. Reprinted with permission from ref 8. Copyright 2017, AAAS.

Halide perovskites also possess materials properties of interest for optical sources: bright photoluminescence, narrow light emission linewidth, tunable exciton binding energy and balanced charge carrier mobility^{9,10}. In the early 1990s, researchers applied layered structured halide perovskites (e.g. Ruddlesden-Popper phases) to create light-emitting diodes (LEDs) that operated at liquid nitrogen temperature¹¹. In 2012, room temperature halide perovskite LEDs were reported¹². In 2015, the first efficient perovskite LEDs (EQE~8.5 %) were reported¹³. Studies of perovskite optical sources have similarly intensified in the past 6 years.

This Review discusses the structural and materials processing degrees of freedom available in perovskites and their impact on light emission and photophysical properties. We discuss cases for, and the challenges in, the use of perovskites in optical sources. We address device architectures in perovskite LEDs as well as interface engineering therein. We seek to connect device performance with underlying photophysics and perovskites' distinctive optical properties.

2. Chemical and Structural Diversity in Perovskites

Three lattice positions in perovskites are referred to as the A, B and X sites. The highest symmetry phase perovskite occupies the $Pm3m$ space group in which the ions are perfectly packed and their ionic radii follow $r_A + r_X = \sqrt{2}(r_B + r_X)$ where r_A , r_B and r_X are the ionic radii of A, B and X. To study the stability of perovskites, Goldschmidt proposed the tolerance factor t and the octahedral factor μ . The tolerance factor indicates the state of distortion by $t = (r_A + r_X)/\sqrt{2}(r_B + r_X)$ and the octahedral factor is determined by the ratio of r_B/r_X for the BX_6 octahedron. In general, hybrid perovskites present $0.44 < \mu < 0.90$ and $0.81 < t < 1.11$. For the perovskite cubic structure, t falls between 0.9 and 1.0, whereas the 0.71 - 0.90 range exhibits tetragonal and orthorhombic structures (Figure 3). Many properties of perovskites effected by structural distortions and, as a consequence, partial or full cation and/or anion substitution can be used to tune the physical properties. In metal

halide perovskites, the B-site metal is typically a divalent cation (e.g., Pb^{2+} , Sn^{2+} , Ge^{2+} , Mg^{2+} , Ca^{2+} , Sr^{2+} , Cu^{2+} , Ni^{2+}), the A-site is a monovalent cation (e.g., Cs^+ , CH_3NH_3^+ (MA), $\text{HC}(\text{NH}_2)_2^+$ (FA) and the X-site is a halide or pseudohalide anion (e.g., I^- , Br^- , Cl^- *etc.*).

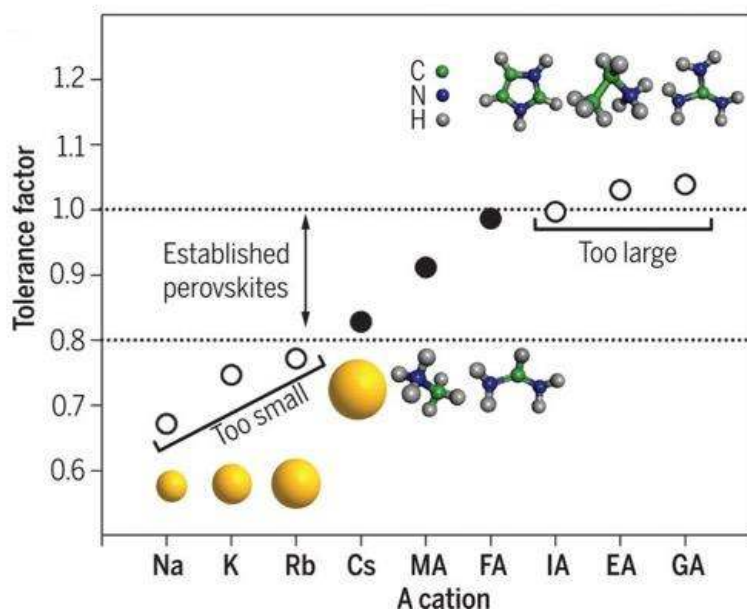


Figure 3. The tolerance factor in APbI_3 perovskites prohibits the use of Na, K, and Rb as A cations; whereas Cs, MA, and FA are widely used; and imidazolium (IA), ethylamine (EA), and guanidinium (GA)] are too large to fit into the 3D cage¹⁴. Reprinted with permission from ref 14. Copyright 2016, AAAS.

Accessing the lower-dimensional structural family, such as one-dimensional (1D) chained architectures and zero-dimensional (0D) isolated octahedra, adds further tuning through chemical and structural engineering. Modification of composition and structure in low-dimensional perovskites enables tuning of electronic bandgaps, exciton binding energies, and electronic transport properties.

2.1 Effect of Organic and Inorganic Compounds

To describe the symmetry of halide perovskites, one needs to consider the dynamic motion of organic A-sites and X-sites. Disordered A-site organic cations change hydrogen bonding and thus affect symmetry variations. The specific alignment of the A-site polar organic cation is induced by hydrogen bonding in the perovskite lattice, a fact that may result in bulk electric ordering¹⁵. This electronic ordering is dependent on the dipole moments of the A-site and the strength of the hydrogen bonds (Figure 4). Organic cations (MA ions) possess an electrical dipole of 2.3 D¹⁶, an aspect that impacts the observed properties and behavior of perovskite solar cells (Figure 5). For example, the dipolar disorder of MA cations contributes to high dielectric constants in MAPbX₃, a fact that assists in screening charged states¹⁷. The incorporation of MA does not necessarily reduce the formation of defects, but the incorporation of the dipolar MA cation in mixed cation mixed halide wide-bandgap perovskites heals deep trap defects, resulting in a more defect-tolerant material¹⁸. Quasielastic neutron scattering (QENS) measurements have directly measured the motions of MA ions within the inorganic lattice of the perovskite. Density functional theory (DFT) on lattice dynamics indicates that low-energy phonons are composed entirely of the motion of metals and halides¹⁹⁻²³, and that these are readily excited at lower temperatures and determine the ensuing physical properties.

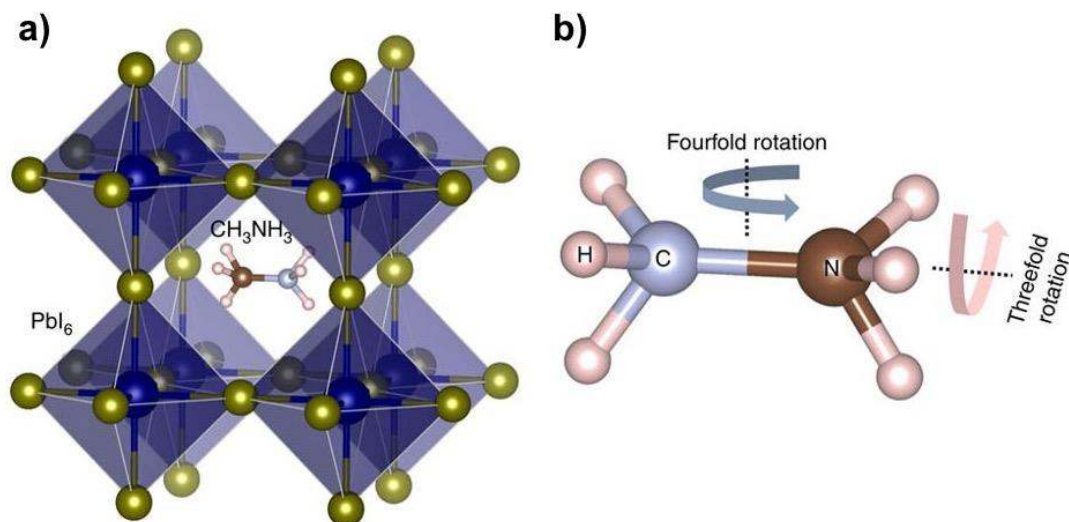


Figure 4. a) Schematic of the perovskite crystal structure. The figure depicts orientational disorder of organic cations in the centre of PbI_6 octahedral cage. b) Geometry of methylammonium illustrating threefold and fourfold jumping rotational modes²⁴. Reprinted with permission from ref 24. Copyright 2017, Nature Publishing Group.

In an ideal cubic halide perovskite, the B-site divalent metal is located at the body-centered position of the cube, and the anions occupy the six face-centered locations, forming an octahedral surrounding for the divalent metal, with the monovalent cations situated at the cube vertices. The chemical bonding between the metal and the halogen determines the bandgap and the dispersion of the energy bands in the material. Larger electronegativity differences correspond to a more ionic bond character, resulting in an electronic cloud less dispersed along the bond and located closer to the nuclei.

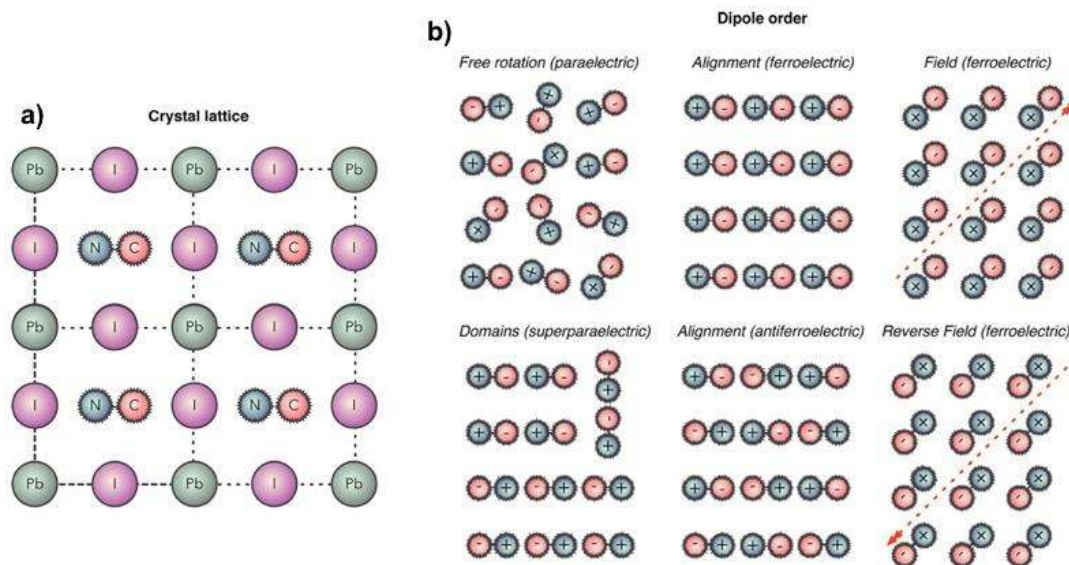


Figure 5. Schematic illustration of crystal structure in MAPbI_3 . a) Molecular dipole orientation in perovskite lattice, b) The molecular dipole of MA is 2.3 D, distinguishing it from spherical /

symmetric cations in inorganic perovskites such as CsSnI_3 ¹⁶. Reproduced from ref 16. Copyright 2014, American Chemical Society.

The inorganic metal cation at the B site is often chosen to be Pb^{2+} in light of the superior optoelectronic properties and solar cell performance of the resultant material. There is interest in finding ions to replace Pb in light of its environmental / toxicological properties²⁵. Engineering the choice of the B site cation also affects the dimensionality of the perovskite structure, particularly so in the case of trivalent and tetravalent metal cations.

The bandgap energy of perovskites is varied by the alternation of the anion (typically I^- and/or Br^-) and the use of mixed anions. For example, the absorbance spectrum of the $\text{MAPbI}_{3-x}\text{Br}_x$ perovskites blueshifts as the bromide concentration is increased – a fact related to the lower electronegativity of the smaller halogen atoms. The optical absorption is therefore readily tuned, via bandgap engineering in halide perovskites, across the visible spectrum.

2.2 Effect of Dimensionality in Perovskites

Reducing perovskite materials' dimensionality also modulates their optical properties²⁶. The structural freedom in reduced dimensional perovskite creates the possibility to create tunable photophysical and electronic properties. The ABX_3 structure has rigid structural constraints due to the corner-shared BX_6 octahedra crystal structure; whereas the reduced dimensional perovskites allows increased structural flexibility, influenced by the length of interlayer organic cations. As the ABX_3 perovskite structure is cut into layers, the size limitation and the tolerance factor seen in the bulk perovskites can be widely engineered. In two-dimensional (2D) derivatives of the perovskites, the interlayer A cation lengths are more easily tuned; and in the zero-dimensional

(0D) derivatives, size restrictions are not applicable, as the isolated MX_6 octahedra shift readily in relative position (Figure 6).

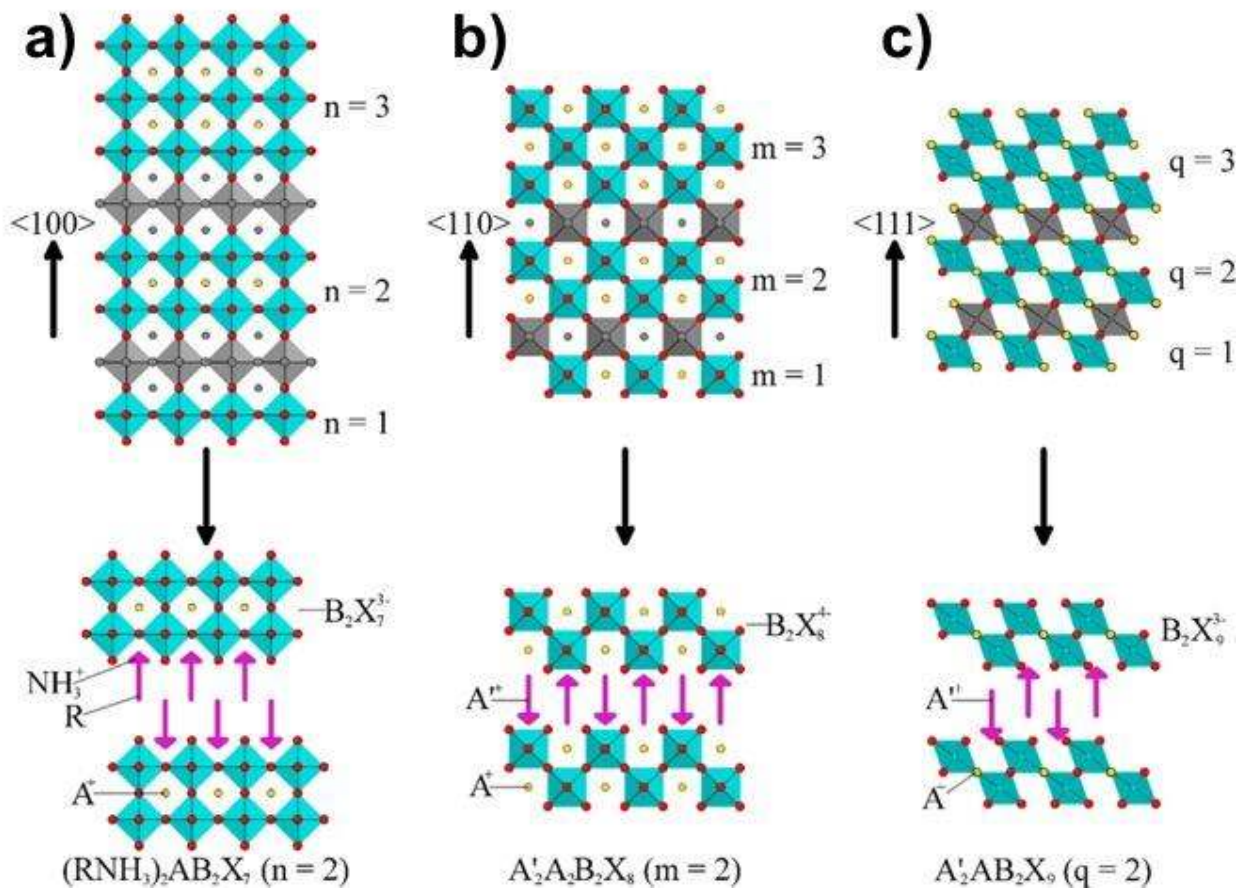


Figure 6. Crystal structures of low dimensional perovskites having different orientations. a) The $\langle 100 \rangle$ -oriented layered perovskites $(\text{RNH}_3)_2\text{A}_{n-1}\text{B}_n\text{X}_{3n+1}$. b) The $\langle 110 \rangle$ oriented layered perovskites $\text{A}'_2\text{A}_m\text{B}_m\text{X}_{3m+2}$. c) The $\langle 111 \rangle$ -oriented perovskites $\text{A}'_2\text{A}_{q-1}\text{B}_q\text{X}_{3q+3}$. Reproduced from ref 27. Copyright 2016, American Chemical Society.

2.2.1 Three-Dimensional Perovskites

Early embodiments of perovskite solar cells were demonstrated using three-dimensional (3D) MAPbI_3 compounds in 2009. The 3D perovskites exhibits a sharp optical absorption onset, with an absorption coefficient (α) exceeding 10^4 cm^{-1} near the bandedge²⁷. The bandgap of

MAPbI₃ is evaluated to be 1.50–1.55 eV using UV photoelectron spectroscopy. The MAPbI₃ single crystals shows exceptionally low trap-state densities on the order of 10⁹ cm⁻³ to 10¹⁰ cm⁻³ in – values comparable to those in crystalline silicon – and charge carrier diffusion lengths on the order of 3⁻¹⁰ μm have been reported^{9,28}. Charge mobilities in thin film MAPbI₃ were obtained as high as 0.5 cm²/Vs using field-effect transistor measurements (FETs)²⁹. However, the volatile nature of MA cations in perovskites may cause instability against moisture and heat – evaporation may be possible at temperatures as low as 85°C, and indeed such materials have been seen to degrade after exposure to moisture, heat and light soaking.

Replacing MA with other organic or inorganic cations tunes the bandgap of 3D lead halide perovskites. A new choice of A site cation changes the bandgap because of the modification of the lattice constant: FA is larger than MA, which in turn is larger than Cs, resulting in an increase of bandgap going from FA to Cs through MA. The A-site cation also influences the extent of metal-halide orbital overlap. This change in metal-halide bonding has a direct impact on valence and conduction band positions³⁰.

When one uses formamidinium (HC(NH₂)₂) as cation, the perovskite reduces in its bandgap by about 0.07 eV compared with MA perovskite, a fact that has been exploited in achieving the most recent photovoltaic performance advances. Because FA produces more thermally stable materials, FA-based perovskites are also promising materials for high-efficiency photovoltaics. However, the phase instability of FA perovskites makes it difficult to maintain the desired photoactive black phase at room temperature. This has led to a considerable recent focus on 3D perovskites in which the A cation is replaced with Cs⁺, and in which mixed triple cations (Cs/FA/MA) are employed to improve phase/thermal stability and performance in devices³¹.

Mixed halide perovskites are of interest also in view of their continuous bandgap tunability (approximately 1.7 to 1.9 eV). Unfortunately, bandgap instability due to photoinduced ion segregation occurs even when mixed halides are used in mixed-cation perovskites³². Recently, Stranks and co-workers demonstrated passivation of surface and grain boundaries in perovskite films to mitigate both non-radiative losses and photoinduced ion migration³³. Bandgap instability was substantially suppressed using interface approaches: Rand and co-workers reported a strategy to suppress halide ion migration using long organic alkyl ammonium capping layers, to reduce perovskite grains at the nanometer size scale³⁴.

Substituting Pb with Sn in the halide perovskites has been demonstrated to narrow the bandgap to 1.2–1.4 eV. Mixed Sn/Pb perovskites with the composition $\text{CsPb}_{1-x}\text{Sn}_x\text{IBr}_2$ have been fabricated via one-step antisolvent spin-coating methods³⁵. Sn substitution alters the driving force for phase segregation and increases the barrier for ionic diffusion, a factor that may contribute to enhanced phase stability.

The remarkable performance of perovskite solar cells and LEDs is correlated with their long excited state lifetimes and high photoluminescence (PL) efficiencies. High-quality perovskite films exhibit longer PL lifetimes, and it has been demonstrated that grain boundaries plays an important on physical properties. Ginger and co-workers used confocal fluorescence microscopy correlated with scanning electron microscopy to resolve spatially the PL decay dynamics of $\text{MAPbI}_3(\text{Cl})$ perovskite films. They observed that PL intensity and lifetime differ among the grains in the perovskite films. The grain boundaries in the perovskite film were dimmer and exhibited faster nonradiative decay. Chemical treatment with pyridine activated the dark grain boundaries and provided passivation that led to brighter materials³⁶.

2.2.2 Two-Dimensional Perovskites

Long-chain alkyl ammonium organic/inorganic lead halide perovskites were fabricated, early in perovskite studies, producing materials with the formula of A'_2MX_4 , and often known as two-dimensional (2D) perovskites. Here A' is the long organic alkylammonium cation, M a divalent metal cation, and X a halide anion. Most reported 2D perovskite derivatives feature mono- and diammonium cations, with general formula of $(NH_3RNH_3)MX_4$ or $(RNH_3)_2MX_4$, R represents an organic functional group. The crystal structure is expressed with reference to the orientation and configuration of the organic³⁷.

Low-dimensional perovskites are formed with slicing the 3D compounds in different crystallographic directions, and the organic cation and reaction stoichiometry play an important role in determining the crystal orientation. Tuning of the dimensionality affects physical properties: the bandgap of the compounds increases as the dimensionality of the structure is reduced, as in thin quantum wells of other semiconductors. Early research on low-dimensional perovskites included pioneering reports on the compound $(C_4H_9NH_3)_2(CH_3NH_3)_{n-1}Sn_nI_{3n+1}$ ³⁸. The 3D perovskite $CH_3NH_3SnI_3$ is a small-bandgap semiconductor; whereas the $n = 1$ compound $(C_4H_9NH_3)_2SnI_4$ is a larger bandgap semiconductor³⁸. Unfortunately, $(C_4H_9NH_3)_2SnI_4$ is sensitive to air, and degradation occurs within several hours. Material synthesis to device testing must be carried out in an inert atmosphere.

These layered materials are natural quantum-well structures, and they possess large exciton binding energies (>100 meV) due to strong electron–hole interactions originating from the distinct dielectric environment in the well vs. the barrier. This enhances photoluminescence intensity, and the high quantum yield also benefits from diminished forbidden electronic transitions. The strong confinement in wide range of structural flexibility, layered perovskites are well-suited to light-emitting applications.

Electroluminescence (EL) was observed from $(\text{C}_6\text{H}_5\text{C}_2\text{H}_4\text{NH}_3)_2(\text{CH}_3\text{NH}_3)\text{Pb}_2\text{I}_7$ in early 1990; however, this was observed only at 200 K and with the application of a 10 kV/cm electric field³⁹. Thermal quenching of the exciton was the main reason for the reduction of EL near room temperature⁴⁰.

More recently, low-dimensional perovskites have attracted renewed interest for solid-state lighting applications. Higher-number layered compounds $(\text{A}')_2\text{A}_{n-1}\text{Pb}_n\text{X}_{3n+1}$ with $n=2, 3, 4$, etc. are formed through mixture of cations of different sizes, capable of forming mixed 3D and layered perovskite structures⁴¹⁻⁴³. By making films consisting of a range of n , one can produce energy funneling through a collection of grains having different bandgaps. This has been found to enhance luminescence properties at room temperature⁴¹⁻⁴⁵.

Low-dimensional perovskites with the formula $(\text{A}')_2(\text{CH}_3\text{NH}_3)_{n-1}\text{Pb}_n\text{X}_{3n+1}$ have also been demonstrated to stabilize solar cell performance against moisture, a finding explained by the increased formation energy compared with their 3D bulk perovskite counterparts^{26,46,47}. The low-dimensional perovskites typically feature different cuts from the 3-D structure along the $\langle 100 \rangle$, $\langle 110 \rangle$ and $\langle 111 \rangle$ directions. $\langle 100 \rangle$ -oriented perovskites are obtained by removing the metal (Pb) component from the inorganic framework. In contrast to the $\langle 100 \rangle$ -oriented perovskite hybrid that represents today the most richly-explored member of the reduced-dimensional perovskite family, the $\langle 110 \rangle$ - and $\langle 111 \rangle$ - oriented perovskites have rarely been reported. $\langle 110 \rangle$ -oriented organic–inorganic perovskites have the formula $[\text{NH}_2\text{-C(I)NH}_2]_2(\text{CH}_3\text{NH}_3)_n\text{Sn}_n\text{I}_{3n+1}$ ($n=1-4$) and were reported by Mitzi and co-workers⁴⁸. These perovskites were stabilized via the incorporation of methylammonium and iodoformamidinium cations. Differently-dimensioned inorganic sheets are obtained by modulating the proportions of the two ligands. When $n>2$, the methylammonium cations occupy the channel position defined by the corner-sharing metal halide octahedra. The

iodoformamidinium cations play an important role in directing the self-assembly of <110>-oriented perovskites.

The <111>-oriented perovskites are obtained with the formula of $A'_2A_{n-1}B_nX_{3n+3}$, where A' and A are interlayer and intralayer organic cations. An example $n=1$ member is $(H_23\text{-AMP})_2PbBr_6$ (AMP= (aminomethyl)pyridinium). These have a higher presence of the more distorted $PbBr_6$ octahedra, increasing the bandgap. Reported $n=2$ members, including $(NH_4)_3Sb_2I_9$, $(CH_3NH_3)_3Bi_2Br_9$, $[NH_2(CH_3)_2]_3Sb_2Cl_9$, $[NH(CH_3)_3]_3Sb_2Cl_9$, and $(CH_3NH_3)_3Sb_2I_9$, also feature small inorganic cations with $Cs_3Sb_2I_9$ ⁴⁹⁻⁵².

2.2.3 Zero-Dimensional Perovskites

Structurally-distorted perovskites can be considered zero-dimensional (0D) analogs. Karunadasa and co-workers reported $(NMEDA)PbBr_4$ and $(EDBE)PbX_4$ (N-MEDA=N1-methylethane-1,2-diammonium; EDBE=2,2-(ethylenedioxy)bis(ethylammonium)), materials that exhibited white light emission^{53,54}. The wide PL linewidth was impacted by the structural distortion, indicated by the distortion of the $PbBr_6$ octahedron⁵⁵. White light emission was attributed to self-trapped excitons localized in the inorganic lattice. Mao *et. al.*, reported white light-emitting perovskites with composition $(DMEN)PbBr_4$ (DMEN=2-(dimethylamino)ethylamine); $(DMPA)PbBr_4$ (DMPA=3-(dimethylamino)-1-propylamine); $(DMABA)PbBr_4$ (DMABA = 4-dimethylaminobutylamine)⁵⁶ (Figure 7). Among these compounds, $(DMEN)PbBr_4$ has the largest distortion ($\Delta d_{avg} = 17.4 \times 10^{-4}$) and showed broad emission.

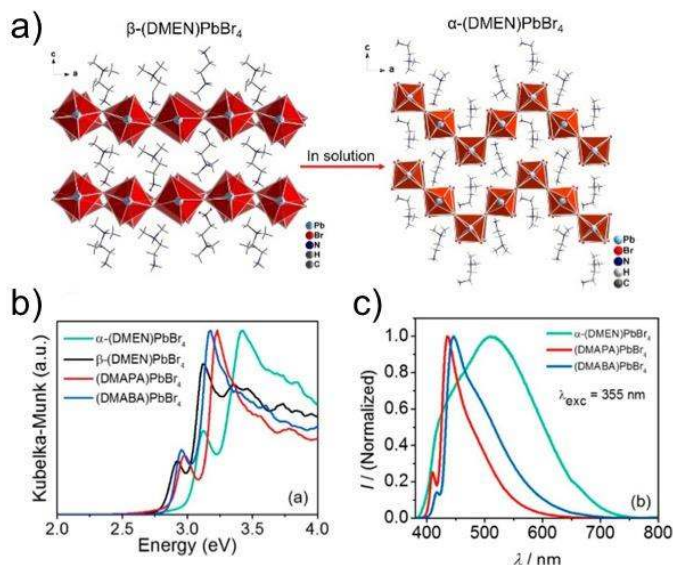


Figure 7. Structural distortion induced 0D perovskites with white light emission⁵⁷. a) Transformation of β -(DMEN)PbBr₄ to α -(DMEN)PbBr₄ in the liquor solution. b) Optical absorption spectra of α -(DMEN)PbBr₄, β -(DMEN)PbBr₄, (DMAPA)PbBr₄, and (DMABA)PbBr₄. c) Steady-state PL emission spectra of α -(DMEN)PbBr₄, (DMAPA)PbBr₄, and (DMABA)PbBr₄ excited at 355 nm. Reproduced from ref 57. Copyright 2017, American Chemical Society.

The perovskite-related Cs₄PbBr₆ structure – first synthesized in 1999 by Nikl *et. al.*⁵⁸ – presents a zero-dimensional (0D) crystalline structure in which adjacent [PbBr₆]⁴⁻ octahedra do not share corners (Figure 8). Manna and co-workers pioneered a facile fabrication strategy to produce Cs₄PbBr₆, starting from CsPbBr₃ NCs: they added different amines to obtain 0D Cs₄PbBr₆ NCs at room temperature⁵⁹. The stability of these NCs in solution was rather low – the particles aggregated in a few minutes. The optical properties measured after the transformation from CsPbBr₃ NCs reveal a sharp absorption at 317 nm which indicates transformation to the Cs₄PbBr₆ phase. Cs₄PbBr₆ NCs have also been prepared in a Cs-rich environment via a hot-injection method⁶⁰. Chemical transformation from non-luminescent Cs₄PbX₆ to emissive CsPbX₃ was triggered by chemical transformation, and this was accompanied by increased air stability and

tunable optical properties. The extraction of CsX from Cs_4PbX_6 can be achieved either by thermal annealing (a physical approach) or by a chemical reaction with Prussian Blue (chemical approach)⁶¹. Alivisatos and co-workers have synthesized another derivative of CsPbBr_3 NCs: they formed lead-halide-depleted perovskite derivative Cs_4PbBr_6 NCs. The transformation is governed by a two-step dissolution-recrystallization mechanism and mediated by the influence of the ligand shell environment on the crystal surface⁶².

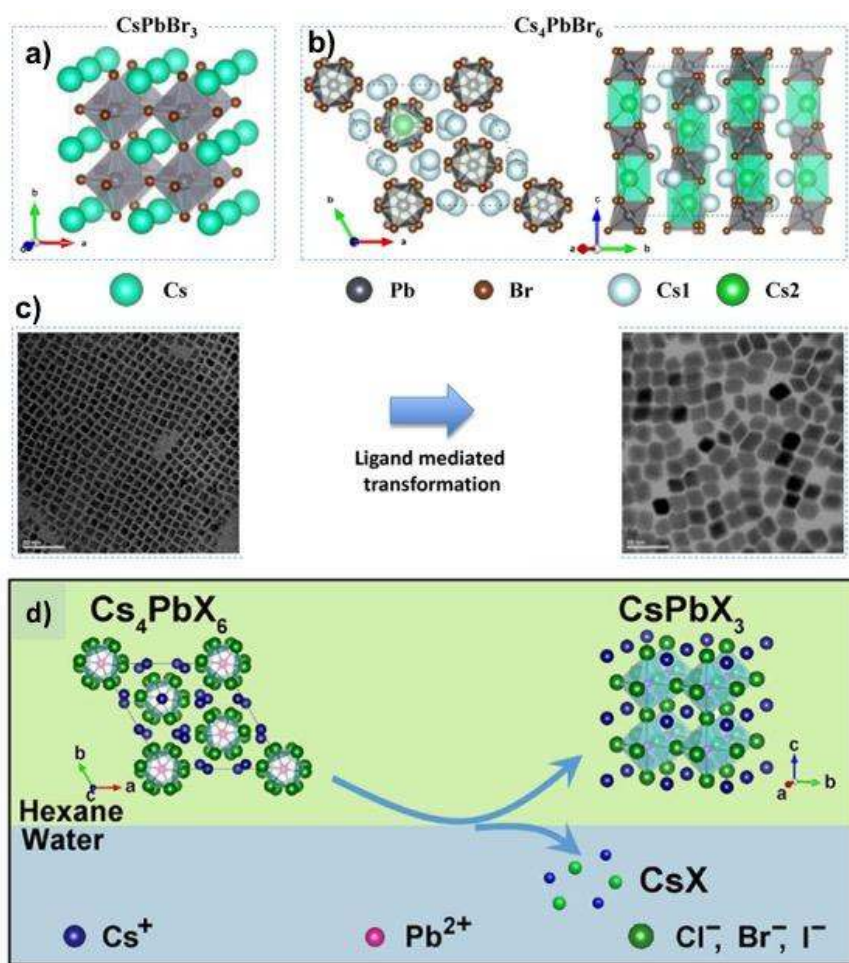


Figure 8. Schematic crystal structure of a) CsPbBr_3 and 0D Cs_4PbBr_6 (b) along and perpendicular to c axis. c) Typical TEM image of CsPbBr_3 and Cs_4PbBr_6 nanocrystals, and images of nanocrystals dispersed in hexane⁶². Reproduced from ref 62. Copyright 2017, American Chemical

Society. d) Schematic illustration of change in the crystal structure going from Cs_4PbBr_6 to CsPbBr_3 ⁶⁰. Reproduced from ref 60. Copyright 2017, American Chemical Society.

Since Cs_4PbBr_6 shows a large bandgap, researchers recently explored the incorporation of perovskite nanocrystal emitters into another crystalline transport phase⁶³. CsPbBr_3 quantum dots embedded in a robust and air-stable Cs_4PbBr_6 microcrystal phase resulted in high luminescence properties, specifically PLQY exceeding 90% in the solid state. The authors demonstrated the role of a lattice match between CsPbBr_3 and the Cs_4PbBr_6 matrix. Chen *et. al.* reported a related study involving CsPbBr_3 embedded in a Cs_4PbBr_6 matrix and reported high efficiency and wide color gamut prototype white light-emitting diodes⁶⁴.

2.3 Lead-Free Perovskites

The regulated nature of lead (Pb) may limit the application of otherwise-promising perovskites. Therefore, there is considerable interest in identifying promising lead-free alternatives. One such case is a class of materials known as double perovskites, in which two metals (*e.g.* metals with 1^+ and 3^+ oxidation states) are combined to yield the overall charge balance as seen in conventional single-metal-cation perovskites⁶⁵⁻⁶⁷. One example is the cubic $\text{Fm}\bar{3}\text{m}$ double perovskite synthesized in the form of $\text{Cs}_2\text{AgBiBr}_6$, having an estimated indirect bandgap of 1.95 eV (as obtained from UV-Vis spectroscopy)⁶⁸.

Tin (Sn), closely analogous in many respects to Pb, has been investigated as a possible alternative to produce lead-free perovskites. Pb and Sn have a similar ionic radii (Pb 1.49 Å and Sn 1.35 Å), and analogous relativistic effects⁶⁹. Sn can therefore substitute Pb with no significant perturbation in the lattice structure. However, Sn^{2+} can be easily oxidized to Sn^{4+} in air, and this can progress further to produce unacceptably high free carrier densities. Seok and co-workers

reported a method to bind SnF_2 strongly with pyrazine: the SnF_2 accepts lone pairs from the N atoms in pyrazine, and this combination of SnF_2 -pyrazine reduces Sn vacancies⁷⁰. The additive SnF_2 furthermore prevented Sn^{2+} from being oxidized to Sn^{4+} , reducing the charge carrier density in FASnI_3 perovskites⁷¹.

All-inorganic CsSnX_3 perovskites have been reported and applied to LEDs⁷². Thin SnX_2 and CsX films were sequentially deposited by vapor deposition then annealed to form uniform CsSnX_3 films via interdiffusion. Smooth, uniform films CsSnBr_3 exhibiting full coverage and very small grain size (60 nm) were achieved; these exhibited an external quantum efficiency (EQE) of 0.34% in red-emitting LEDs.

The 2D $(\text{PEA})_2\text{SnI}_4$ exhibits superior PL properties compared to conventional 3D $\text{CH}_3\text{NH}_3\text{SnI}_3$, as reported by Haque and co-workers. These authors found that the 2D $(\text{PEA})_2\text{SnI}_4$ perovskite displays improved stability compared to $\text{CH}_3\text{NH}_3\text{SnI}_3$ when aged in an air ambient in the dark⁷³. Kanatzidis and co-workers – using CsGeI_3 perovskites based on the trigonal pyramidal $[\text{GeI}_3]^-$ building block by tuning A-cations⁷⁴. Moreover, Ge-based perovskites exhibit a large second harmonic generation (SHG) due to the sp-hybrid orbitals of germanium and iodide.

Ternary Sb^{3+} and Bi^{3+} have also attracted considerable interest in view of their structural flexibility and low toxicity. The $\text{A}_3\text{Bi}_2\text{I}_9$ perovskites involve a 1/3 bi-deficient layered perovskite with bi-octahedral $(\text{Bi}_2\text{I}_9)^{3-}$ clusters surrounded by A^+ (Cs^+ or MA^+). However, trivalent bismuth and antimony perovskites result in 2D structure and shows wider bandgaps than their 3D analogues. To maintain the 3D perovskite structure, an alternative approach was developed, one wherein Pb^{2+} was replaced to form a double perovskite structure of $\text{A}^{\text{I}}_2\text{B}^{\text{I}}\text{B}^{\text{III}}\text{X}_6$, by combining a monovalent cation and a trivalent cation having an ordered metal site arrangement⁷⁵. However, from Tauc plot measurements, the perovskite showed an indirect bandgap, indicating that it may

not be well-suited to efficient light emission. Solis-Ibarra and co-workers developed $\text{Cs}_4\text{CuSb}_2\text{Cl}_{12}$ perovskite, a mixed-metal $\langle 111 \rangle$ -oriented layered structure incorporating Cu^{2+} and Sb^{3+} into layers ($n = 3$)⁷⁶. This material was a semiconductor with a direct bandgap 1.0 eV and a conductivity 1 order of magnitude greater than that of MAPbI_3 .

Recently, $\text{MA}_3\text{Bi}_2\text{X}_9$ ($\text{X}=\text{Cl}, \text{Br}, \text{I}$) perovskite quantum dots were synthesized by Tang and co-workers⁷⁷ (Figure 9). These authors used a strategy based on re-precipitation assisted by ligands that enabled them to tune the PL emission peak wavelength from 360 to 540 nm via halide compositional control. The $\text{MA}_3\text{Bi}_2\text{Br}_9$ QDs had diameter circa 3 nm and – for emission at 430 nm – the PLQY was an encouraging 12%.

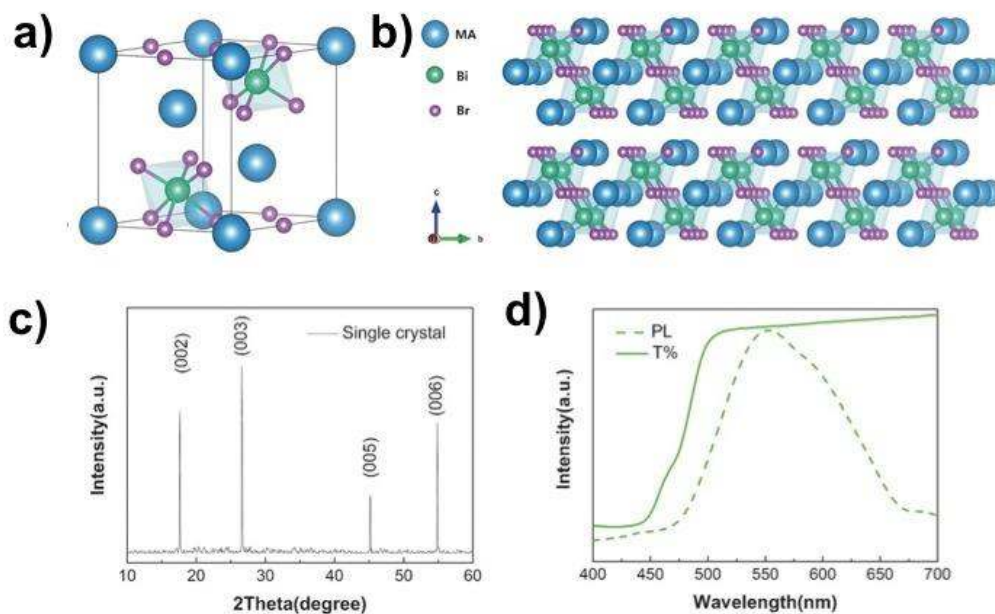


Figure 9. a, b) Schematic structure of single-crystalline $\text{MA}_3\text{Bi}_2\text{Br}_9$, c) Powder X-ray diffraction (XRD) spectra of single crystal $\text{MA}_3\text{Bi}_2\text{Br}_9$. d) Transmission (solid) and PL (dashed) spectra of $\text{MA}_3\text{Bi}_2\text{Br}_9$ single crystal⁷⁷. Reprinted with permission from ref 77. Copyright 2016, Wiley-VCH.

3 Perovskite Photophysical Properties

Of critical importance in the operation of electronic devices are processes such as the generation of charge carriers and excitons; and also the diffusion and recombination of these photoexcited states. The rates of recombination of electrons and holes are lower than in prior single-crystalline inorganic semiconductors.⁷⁸ Films based on polycrystalline perovskite constituents have shown impressive diffusion lengths ($L_D > 1\ \mu\text{m}$) for minority carriers and correspondingly extended excited-state lifetimes ($\tau \geq 1\ \mu\text{s}$). They have combined these features with excellent mobilities ($\mu \approx 1\text{--}100\ \text{cm}^2\ \text{V}^{-1}\text{s}^{-1}$)⁷⁸⁻⁸¹, even in the presence of realistic defect states (traps).

Here we review the nature of photogenerated exciton/carriers within perovskites (Figure 10).

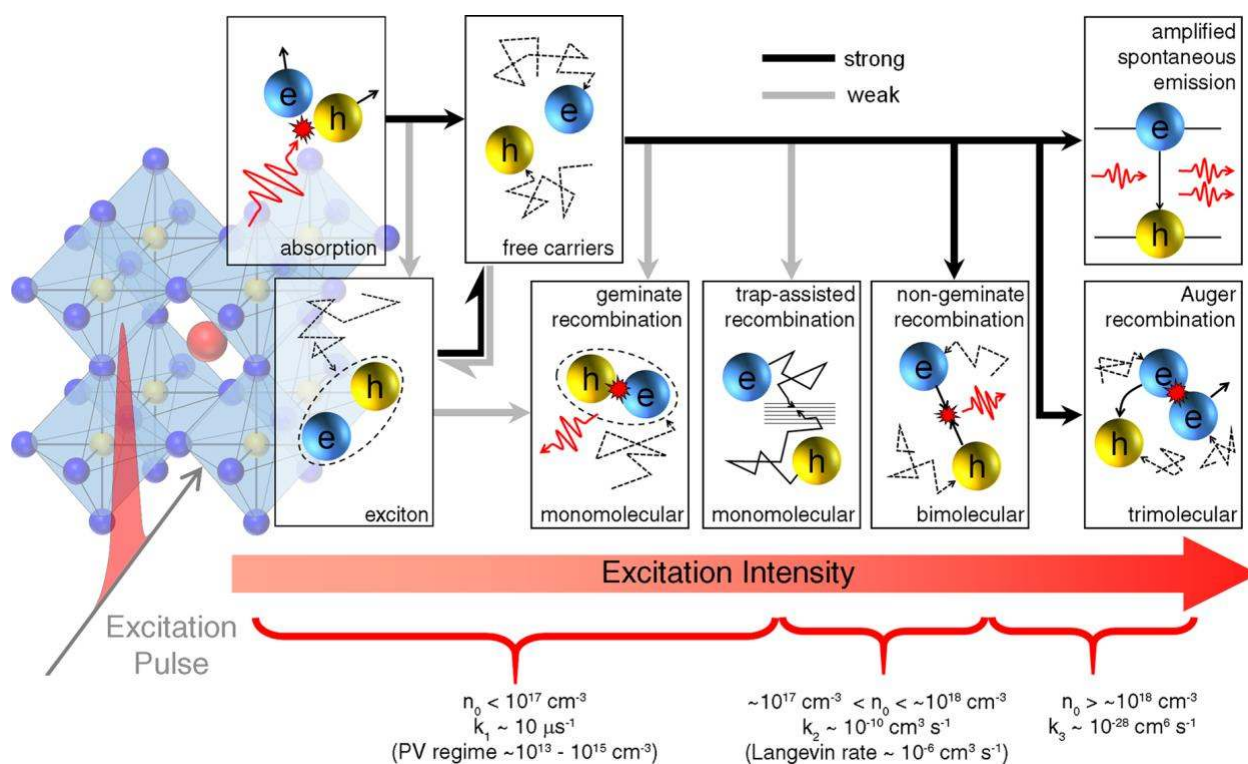


Figure 10. Rates of recombination, and photophysical processes, in MAPbI₃ over a range of carrier densities, n_0 ⁸². Reproduced from ref 82. Copyright 2016, American Chemical Society.

3.1 Recombination Mechanisms

Using transient absorption (TA) and time-resolved photoluminescence (TRPL) measurements, one may determine the bimolecular recombination rate⁸³⁻⁸⁷. In MAPbI₃ perovskites, the results of early spectroscopic investigations were accounted for by invoking the charge separated states, or excited charge transfer state⁸⁷. It is now widely held that excitons dissociate spontaneously into separated electrons and holes, a fact that contributes to the impressive performance of perovskite devices.

The photophysics of perovskites depends on excitation level. When the conditions of photoexcitation produce low carrier densities in the range $n_0 \approx 10^{13} - 10^{15} \text{ cm}^{-3}$ – these are of the level relevant to solar cells – monomolecular trap-assisted recombination or geminate recombination are each low in efficiency. They have a low first-order recombination coefficient in the vicinity of $k_1 \approx 10 \text{ } \mu\text{s}^{-1}$ ⁸⁸.

In contrast, when the photocarrier densities are higher at $n_0 \approx 10^{16} - 10^{18} \text{ cm}^{-3}$, effects associated with multiparticle processes, such as nongeminate recombination (bimolecular) and Auger recombination processes (trimolecular), gain in importance and indeed begin to dominate the excited state lifetime^{89,90}.

We write the rate equation for charge-carrier recombination in a way that takes account of both monomolecular and also higher-order processes (equation 4):

$$\frac{dn}{dt} = G - k_1 n - k_2 n^2 - k_3 n^3 = G - nR_T(n) \quad (4)$$

In this equation, G is the charge-density generation rate. The term k_1 provides the coefficient associated with monomolecular recombination. The coefficient k_2 functions as the constant of proportionality informing the bimolecular electron–hole recombination rate. Finally, k_3 quantifies the Auger rate.

Kamat and co-workers found that strong band-filling effects and bandgap renormalization observed from MAPbI₃ at high pump fluences⁸³. Ultrafast relaxation processes in thin films of the hybrid perovskite MAPbI₃ indicated a carrier-density-dependent blueshift and broadening of the 760 nm photogenerated ground state bleach, indicating charge carrier accumulation and explained on the basis of a Burstein–Moss shift (a dynamic one in this instance). The bandedge states lead to higher-energy optical transitions, a fact connected to the Pauli exclusion principle (Figure 11).

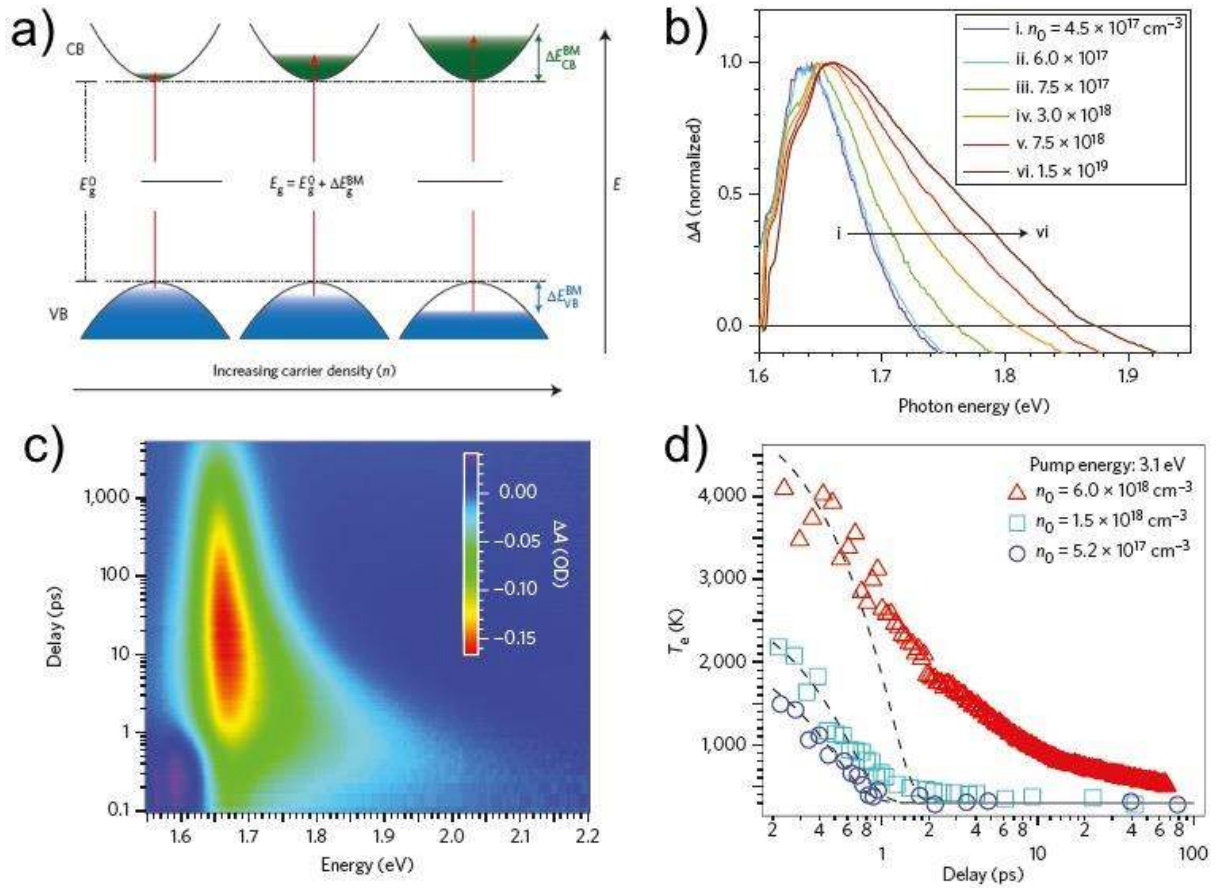


Figure 11. a) Schematic illustration of the Burstein–Moss effect in MAPbI₃ perovskites⁸³. Reprinted with permission from ref 83. Copyright 2014, Nature Publishing Group. b) Normalized spectra (TA) of the bandedge transition in MAPbI₃⁸³. c) Pseudocolour representation TA spectra shows hot carrier thermalization in MAPbI₃⁹¹. Reprinted with permission from ref 91. Copyright 2015, Nature Publishing Group. d) Time-dependent T_e with the same n_0 but varying $\hbar\omega_{\text{pump}}$, dashed

lines are calculated cooling curves⁹¹. Reprinted with permission from ref 91. Copyright 2015, Nature Publishing Group.

Yang *et. al.*, have quantitatively correlated the TA spectra with photophysical properties including carrier density, the carrier temperature bandgap renormalization and exciton binding energy, and demonstrated the interplay between free-carrier induced bleaching of the excitonic and continuum transitions near the band edge⁹¹. The carrier temperature can be extracted from the TA spectra and help to illuminate carrier cooling dynamics. Measurements have indicated slow hot-carrier cooling with high excitation density, attributed to a hot-phonon bottleneck. The observed phonon bottleneck slows hot carrier cooling above a critical injection carrier density of $\sim 5 \times 10^{17} \text{ cm}^{-3}$.

3.2 Exciton and Free Carrier Dynamics

Since hybrid halide perovskites at room temperature show free carriers, monomolecular recombination originating from trap-assisted processes are influenced by crystal formation processes and ensuing crystalline quality. In direct bandgap semiconductor, the bimolecular recombination process is an intrinsic property, and its coefficient resides typically between 0.6×10^{-10} to $14 \times 10^{-10} \text{ cm}^3 \text{ s}^{-1}$ at room temperature^{78,88,92}.

Photoinduced terahertz conductivity measurements of MAPbI_3 and $\text{MAPbI}_{3-x}\text{Cl}_x$ ⁸⁸ revealed the time-resolved behavior of excitations in perovskites, identified as free charge carriers. In the presence of free charges, the measured relative change in THz electric field transmission is proportional to the photoinduced conductivity in the material. The observed dynamics can be accounted for by invoking the photoconductivity of free charges alone.

Auger recombination is many-body process involving charge carriers and momentum transfer to another electron or hole⁹³. The average range of Auger recombination values in halide perovskite is about $k_3 = (0.2-1.6) \times 10^{-28} \text{ cm}^6 \text{ s}^{-1}$)^{78,88,92}, which is on average ~25 times higher than the Auger rate constant for GaAs⁹⁴.

The binding energies for excitons (E_b) in perovskites have seen considerable investigation⁹⁵⁻¹⁰³. At room temperature, the exciton binding energies are typically lower than the thermal energy kT required to dissociate excitons. E_b in MAPbI₃ perovskites is sufficiently low to be classed as the Wannier-Mott type (equation 5) :

$$E_n = -\frac{m_r^* e^4}{8h^2 \epsilon_0^2 \epsilon^2} \frac{1}{n^2} = -\frac{E_b}{n^2} \quad (5)$$

From the above equation 5, MAPbI₃ with a bandgap energy of (~1.6 eV) has an estimated exciton binding energy in the range 2–20 meV. The range of experimentally reported values of E_b for MAPbI₃ is in good agreement with this, spanning 2 to 62 meV^{95-97,99,103}. The temperature-dependence of luminescence can also be used to determine the exciton binding energy. Temperature-activated exciton dissociation induces a decrease in photoluminescence by increasing temperature. Here values have ranged from E_b of 19 meV¹⁰⁴ - 32 meV¹⁰¹ for MAPbI₃ and a higher 62 meV for MAPbI_{3-x}Cl_x¹⁰².

Another approach that one can use to obtain the exciton binding energy utilizes analysis of the absorption spectrum, focusing especially near the bandedge¹⁰⁰. From knowledge of the bandwidth of the bandedge absorption, and also when one obtains temperature-dependent measurements, one reaches the conclusion of an exciton binding energy in the range (55 ± 20) meV. A considerable diversity in E_b emerged again from the application of this method due to the incorporation of a lineshape broadening process, which add to fitting uncertainties¹⁰³. An

alternative approach based on fits to the absorption spectra near the onset, and normalized to a particular energy, is still sensitive to lineshape broadening¹⁰³.

Another way to measure the exciton binding energy has been reported based on high-field interband magneto-absorption measurements⁹⁹ (Figure 12). The measurements allow determination of the reduced effective mass, and this enables the study of multiple excitonic transitions for added precision.

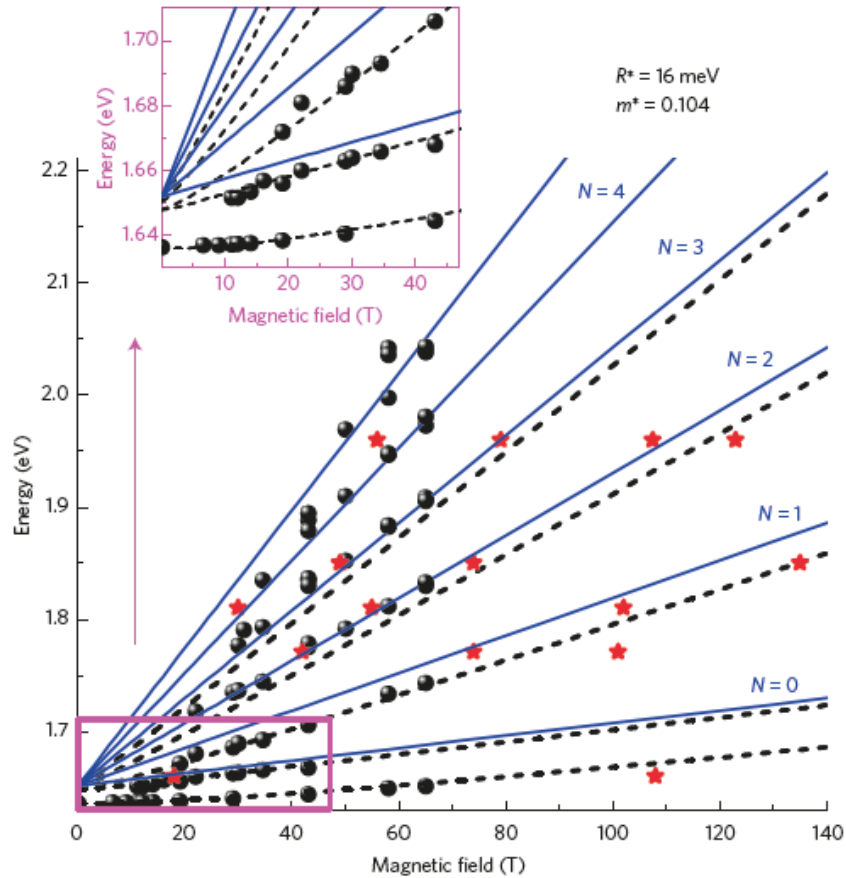


Figure 12. Measurement of exciton binding energy as a function of increase in magnetic field⁹⁹.

Reprinted with permission from ref 100. Copyright 2015, Nature Publishing Group.

In single grains of polycrystalline MAPbI₃ thin films, spatial heterogeneities on the nm length scale were investigated through study of free-carrier and exciton populations¹⁰⁵. Using transient

absorption microscopy, Harel and co-workers directly observed shifts of the bandedge absorption in different grains. Both excitons and free carriers were found to exist together, but segregated on the \sim hundred nm scale. In the case of low-dimensional perovskites, the confinement of excitons to the wells can be accounted for via the sizeable difference in dielectric constant for the organic barrier compared to the inorganic well. The exciton binding energies are high – 100s of meV – and the high radiative rate ensures that the reduced-dimensional perovskites are of particular interest in light-emission applications. Grozema and co-workers carried out a detailed temperature-dependent study of mobility and exciton dissociation in these materials¹⁰⁶ and reported an increase in charge carrier mobility when the temperature was lowered and bound excitons were favored. They saw as a result a further increase in the photoluminescence quantum yield at lower temperatures. This interconversion process is governed by E_b that depends strongly on the number of inorganic layers (n) in low-dimensional perovskites, ranging from ~ 370 meV to ~ 80 meV as a function of n from 1 to 4.

3.3 Photoluminescence Quantum Yield

Measurements of the photoluminescence quantum yield (PLQY) of high refractive index materials, such as thin films of polymeric semiconductors, take account of the angular distribution of emission, reflectivity, and absorbance. Adding to this complication are optical interference effects and potential photon recycling (reabsorption of emitted photons) that can occur in metal halide perovskites. A quantitative measurement of external PL efficiency¹⁰⁷ η is defined as:

$$\eta = \frac{\text{number of photons emitted}}{\text{number of photons absorbed}}$$

The power-dependent PLQY of thin films of $\text{MAPbI}_{3-x}\text{Cl}_x$ perovskites on glass were particularly revealing¹⁰⁸. The PLQY grew to an impressive 70% at high power excitation (100

mW/cm²), a result of radiative outcompeting nonradiative recombination: bimolecular radiative recombination dominated at the higher excitation intensities and defects became filled.

A variety of approaches have been applied to maximize PLQY, including strategies seeking to increase E_b and the oscillator strengths of the excitons. Charge confinement was introduced in MAPbBr₃ by reducing the grain size, which increased the radiative rate, and 36% PLQY was achieved in the visible region at 530 nm¹³. In the 2D PEA₂PbI₄ perovskites the PLQY was as low as 1% at room temperature, ascribed to thermal quenching of excitons^{40,41}. Mixed-phase low-dimensional perovskites exhibit much higher PLQY and LED EQE at room temperature^{41,42,44}. Surface traps in perovskite nanocrystals can cause a low PLQY, and passivating halide-ion pair ligands has been shown to improve performance¹⁰⁹. Near unity PLQY for CsPbI₃ perovskite nanocrystals reported by Liu *et.al.* were achieved by improving a synthetic protocol that involves the use of trioctylphosphine–PbI₂ as a precursor – an approach that also improved stability for the resulting CsPbI₃ nanocrystal solutions¹¹⁰.

4 Perovskite Light Emitting Diodes (LEDs)

4.1 Perovskite Material Engineering for LEDs

Material engineering of perovskites is crucial to achieve highly luminescent PL properties: materials crystal structure, composition, domain size and surface chemistry all influence optical properties. Below we discuss the effect of each on fundamental optical properties and also device-level performance (Table 1).

4.1.1 Modulating Dimensionality in Perovskite for LEDs

In the early 1990s, the Nurmikko and Saito groups^{11,39,111} reported LEDs based on layered 2D perovskites. The authors used a layered perovskite composition (C₆H₅C₂H₄NH₃)₂PbI₄ and

measured the electroluminescence (EL) spectrum at liquid nitrogen temperatures ~ 77 K (Figure 13). An increased scattering rate due to phonons at higher temperatures accounted for the observed thermal quenching.

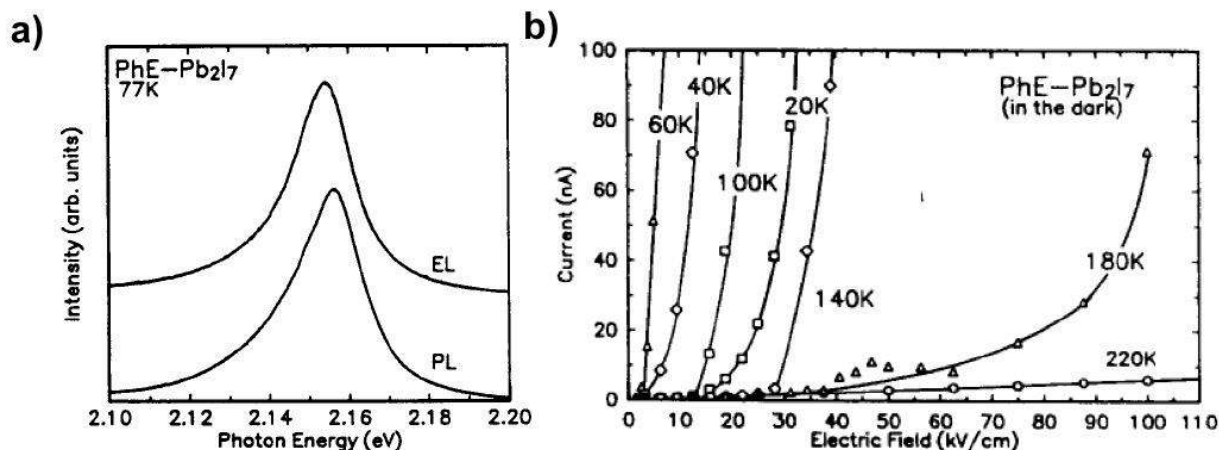


Figure 13. a) Electroluminescence and photoluminescence spectra of perovskite LEDs with $n=2$ layered perovskites. b) Current along the well plane as function of electric field for PhE-Pb₂I₇ perovskite at different temperatures³⁹. Reprinted with permission from ref 39. Copyright 1992, Elsevier.

In 2014, Friend and co-workers¹² reported room-temperature perovskite LEDs based on CH₃NH₃PbI_{3-x}Cl_x having an external quantum efficiency (EQE) of 0.76% and radiance of 13.2 W sr⁻¹m⁻² at a current density of 363 mA cm⁻². Lee and co-workers reported perovskite LEDs based on MAPbBr₃ and exhibiting a current efficiency (CE) of 0.577 cd A⁻¹, an EQE of 0.125%, and a maximum luminance of 417 cd m⁻² (Figure 14)¹¹². Multicolored LEDs were demonstrated by leveraging the mixing of halides (CH₃NH₃PbCl_xBr_yI_{3-x-y}). The perovskite layers were thin enough to confine electrons and holes for bimolecular recombination, enhancing electron-hole capture and increasing radiative recombination. Making pinhole-free films containing crystalline particles, with overall thickness less than 50 nm, was a challenge. One method to overcome this film-

formation challenge is to blend the perovskite precursors with a polymer that is also soluble in the solvents needed to process the metal halide and ammonium halide salts. For example, Li *et. al.* blended perovskites with insulating polyimide and deposited uniform thin films¹¹³. The perovskite grains provided for charge transport and light emission, while the dielectric polymer filled the surrounding pinholes and thus filled potential shunt paths. A similar approach with mixed perovskite/poly(ethylene oxide) films also facilitated perovskite film formation, producing LEDs with relatively high brightness ($4,064 \text{ cd m}^{-2}$)¹¹⁴. As the presence of metallic Pb atoms in MAPbBr₃ has been offered as a cause of trap-induced non-radiative recombination, Lee and co-workers addressed the film nonuniformity issue by providing excess MABr, reducing grain size and suppressing exciton quenching (Figure 15)¹³. The spatially confined MAPbBr₃ grains (average diameter of $\leq 100 \text{ nm}$) were formed by a nanocrystal pinning process with additional TPBi dissolved in the solvent used for the anti-solvent quench. Perovskite LEDs based on this approach had a maximum current efficiency of 43 cd A^{-1} corresponding to an EQE of 8.5%. Park *et. al.* further investigated the introduction of TPBi diluted in a volatile nonpolar solvent during the perovskite nanocrystal pinning process.¹¹⁵

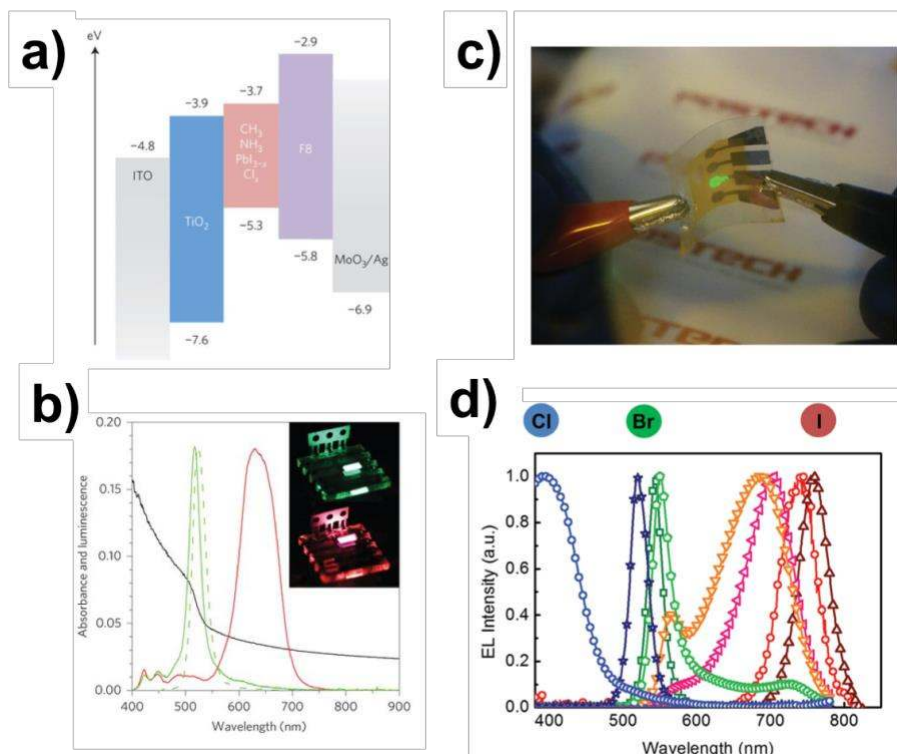


Figure 14. a) Device architecture of $\text{CH}_3\text{NH}_3\text{PbI}_{3-x}\text{Cl}_x$ perovskite LEDs. b) Electroluminescence spectrum of perovskite LED with $\text{CH}_3\text{NH}_3\text{PbBr}_2\text{I}$.¹² Reprinted with permission from ref 12. Copyright 2014, Nature Publishing Group. c) Photograph of perovskite LEDs on flexible PET substrate during bending. d) Electroluminescence spectra of perovskite LEDs with $\text{CH}_3\text{NH}_3\text{PbCl}_x\text{Br}_y\text{I}_{3-x-y}$.¹¹² Reprinted with permission from ref 115. Copyright 2015, Wiley-VCH.

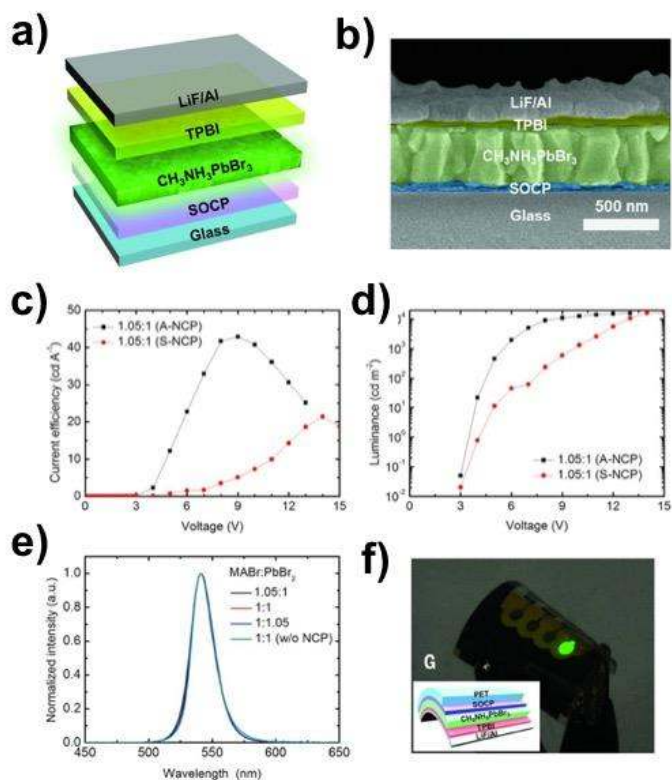


Figure 15. a) Device structure of perovskite LEDs and b) cross-sectional SEM image of perovskite LEDs. c, d) current efficiency and luminance efficiency as a function of voltage in perovskite LEDs based on grainsized controlled MAPbBr₃. e) EL spectra of perovskite LEDs. f) photograph of a flexible perovskite LEDs, and (g) its device structure¹³. Reprinted with permission from ref 13. Copyright 2015, AAAS.

Mixed Cs and FA cation perovskite LEDs developed by Cho *et. al.* incorporated Cs⁺ cations in FAPbBr₃ to reduce significantly the average grain size (from a wide 100-600 nm distribution to a more tightly-controlled average of 200 nm for FA:Cs = 90:10) and trap density; and increased the PLQY and PL lifetime in FA_{1-x}Cs_xPbBr₃ films and, correspondingly, the device performance increased from 1.7 to 3.1%. Incorporation of Cs also increased photostability of FA_{1-x}Cs_xPbBr₃ films due to the suppression of light-induced metastable states¹¹⁶.

Further exciton and carrier confinement was achieved using reduced-dimensional perovskites, as reported by Yuan *et. al.*, who used a perovskite composed of a series of differently quantum-size-tuned grains that funneled photoexcitations to the lowest-bandgap emitters in the mixture upon photoexcitation⁴¹ (Figure 16). Quasi-2D perovskites with a composition of $\text{PEA}_2(\text{CH}_3\text{NH}_3)_{n-1}\text{Pb}_n\text{I}_{3n+1}$ ($\text{PEA}=\text{C}_8\text{H}_9\text{NH}_3$) were used to tune the average layer numbers $\langle n \rangle$ by changing the ratio between PEA and $\text{CH}_3\text{NH}_3\text{I}$. Transient absorption (TA) and time-resolved PL spectroscopy enabled characterization of transport and recombination dynamics at ultrafast timescales. These studies of excitation dynamics revealed how multi-phased perovskite materials channel energy across an inhomogeneous energy landscape, concentrating excitons into the smaller-bandgap emitters (larger n). Perovskite LEDs with $\langle n \rangle = 5$ perovskite exhibited the best performance within this study, with an EQE of 8.8% and radiance of $80 \text{ W Sr}^{-1} \text{ m}^{-2}$, with emission at wavelength 750 nm.

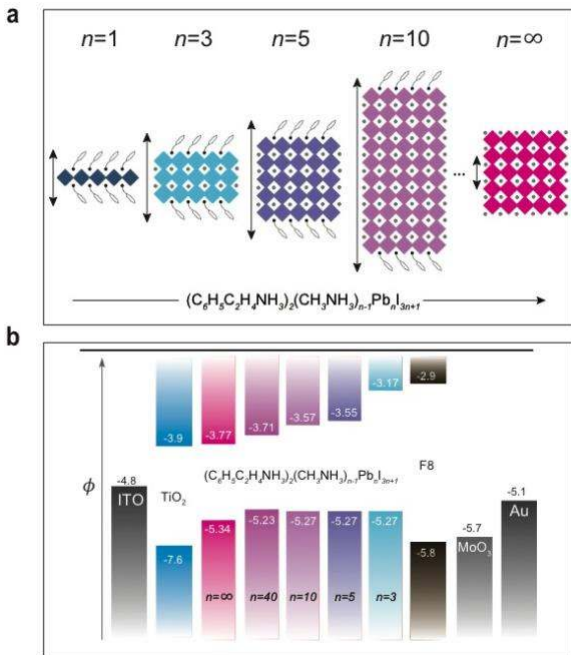


Figure 16. Schematic illustration of $(\text{C}_8\text{H}_9\text{NH}_3)_2(\text{CH}_3\text{NH}_3)_{n-1}\text{Pb}_n\text{I}_{3n+1}$ perovskite structure with different $\langle n \rangle$ values, from 2D ($n=1$) to 3D ($n=\infty$). b, Electronic bandstructure of perovskites with

different $\langle n \rangle$ values, and electronic bandstructure of each layer used in LEDs. ϕ , electric potential⁴¹.
Reprinted with permission from ref 41. Copyright 2016, Nature Publishing Group.

The energy landscape in quasi-2D materials was further engineered by manipulating the crystallization process. Quan *et. al.* tailored the composition of mixed-bandgap perovskites to direct energy transfer into the lowest-bandgap minority phase – a process that occurred faster than loss due to nonradiative centers, thus helping to increase PLQY⁴⁴. By optimizing the domain distribution, the authors achieved a high PLQY of 60% at low excitation fluences (1.8 mW cm^{-2}) in materials exhibiting green emission.

Multiple quantum well strategies explored by Wang *et. al.* used a mixture of 1-naphthylmethylammonium iodide (NMAI) and formamidinium iodide (FAI)^{43,117} (Figure 17). The mixed material showed a high PLQY of 60% since photogenerated excitons in small- n QWs were efficiently energy-transferred to large- n QWs. The mixed quantum well perovskite LEDs achieved narrow emission peaks at 736 nm, 685 nm, 664 nm, 611 nm or 518 nm via Br:I ratio tuning. The best-performing perovskite LEDs turned on at 1.3 V; and the devices achieved an EQE of 11.7% at 2.6 V with a current density of 38 mA cm^{-2} with an emission peak at 763 nm. Grain size engineering was further explored by Xiao *et. al.*⁴². Ammonium halides were added to the stoichiometric 3D perovskites, and these acted as surfactants that constrained the growth of 3D perovskites during film crystallization, resulting in perovskite grains exhibiting dimensions as small as 10 nm and ultra-smooth films with roughness of less than 1 nm (Figure 18). These nanometer-sized perovskite grains coated with longer-chain organic cations (butylammonium halides) yielded efficient perovskite emitters: the resulting LEDs operated with EQEs of 10.4% and 9.3% for perovskite films based on MAPbI_3 and MAPbBr_3 , respectively. They also featured

significantly improved device stability. The self-assembled long-chain butylammonium cations at the crystallite surface impeded ion migration during device operation, significantly reducing hysteresis.

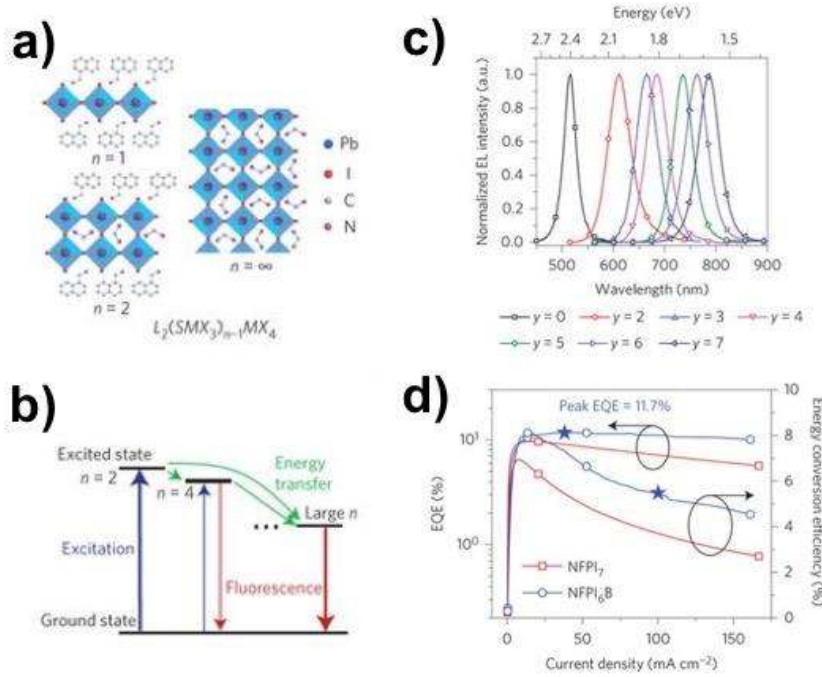


Figure 17. a) Schematic representation of layered lead halide perovskites with $n = 1$, $n = 2$ and $n = \infty$. b) Schematic of cascade energy transfer in multi-quantum well perovskites. Excitation energy is transferred downhill from smaller- n quantum wells to larger- n quantum wells, and the emission is mainly from larger- n quantum wells. c) EL spectra of MQW LEDs based on the $NFPI_yB_{7-y}$ films, $y = 0, 2, 3, 4, 5, 6$ and 7 , respectively. d) EQE and energy conversion efficiency versus current density⁴³. Reprinted with permission from ref 43. Copyright 2016, Nature Publishing Group.

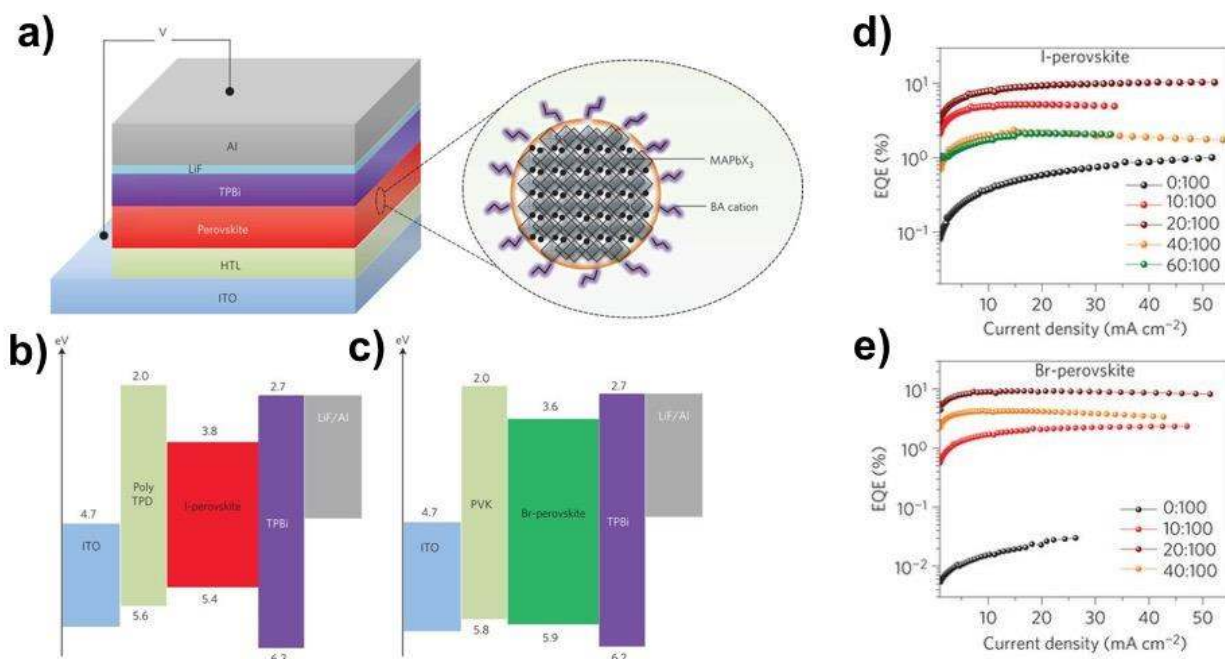


Figure 18. a) Device structure of perovskite LEDs with nanometre-sized perovskite grains. b, c) Energy diagram of I-perovskite and Br-perovskite LEDs. d) Device performance of I-perovskite LEDs with different BAI:MAPbI₃ molar ratios. e) Device performance of Br-perovskite LEDs with different BAbBr:MAPbBr₃ molar ratios⁴². Reprinted with permission from ref 42. Copyright 2016, Nature Publishing Group.

For pure red-emitting ($\lambda \approx 650$ nm) perovskite LEDs, mixed halides (Br/I) allow the needed tuning of the electronic bandgap. However, because of instability of MA and FA iodide/bromide perovskites,¹¹⁸ new approaches have been sought to suppress halide redistribution. These include the use of self-assembled large group ammonium capping layers at nanometer-sized grain surfaces³⁴. In mixed halide perovskite films, halide migration is suppressed by nanometer-sized grains and the use of long organic ligands as capping layers. Stable mixed-halide perovskite films enable fabrication of efficient and wavelength-tunable perovskite LEDs spanning the infrared to the green. Sneha *et. al.* tailored 3D perovskites to provide a near-monodispersed nanoparticle film

prepared using a one-step *in situ* deposition method¹¹⁹. Partially replacing MABr with OABr (octylammonium bromide; $\text{CH}_3(\text{CH}_2)_7\text{NH}_3\text{Br}$) in the perovskite precursor solution enabled controlled nanoparticle formation. An improved maximum brightness of $L_{\text{max}}=4578 \text{ cd m}^{-2}$ was achieved using this strategy.

4.1.2 Colloidally-Synthesized Perovskite Nanocrystals for LEDs

Kovalenko and co-workers pioneered all-inorganic cesium lead halide (CsPbX_3 ; X = Cl, Br, and I) nanocrystals, which exhibited excellent optical properties, with tunable bandgap and high PLQY¹²⁰ (Figure 19).

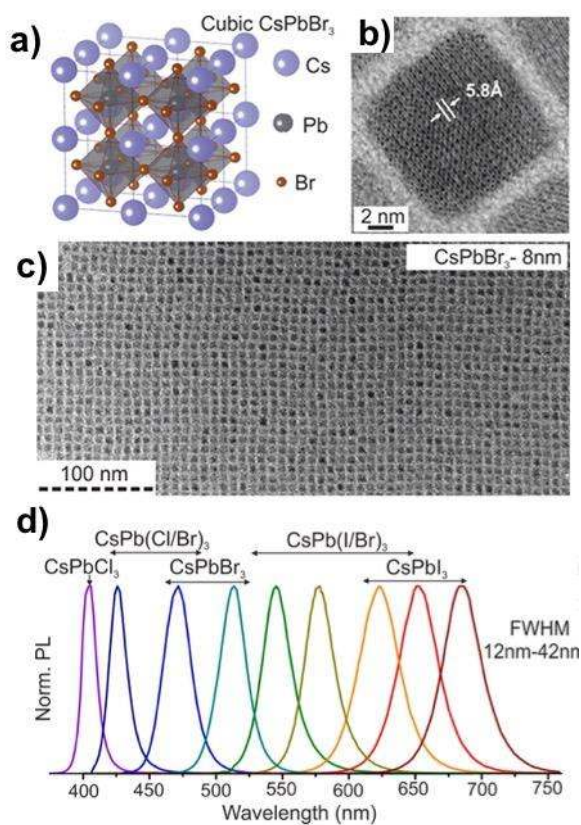


Figure 19. a) Schematic of the perovskite structure; b,c) transmission electron microscopy (TEM) images of CsPbBr_3 NCs; d) representative PL spectra of different halide perovskite nanocrystals¹²⁰. Reproduced from ref 123. Copyright 2015, American Chemical Society.

Tan and co-workers applied a trimethylaluminum crosslinking method to stabilize perovskite nanocrystal films. They were able as a result to deposit charge-injection layers but prevent damage to the perovskite layer¹²¹. The perovskite film showed excellent coverage, and efficient confinement of injected electron-holes led to an electroluminescence yield of 5.7%.

Song *et. al.* then reported perovskite LEDs that utilized CsPbX₃ nanocrystals. High-quality CsPbX₃ nanocrystals were synthesized via the hot injection of the cesium precursor into a PbBr₂ precursor solution at high temperature¹²². The emission wavelength was tuned through both perovskite nanocrystal size and halide composition (Cl, Br, and I). Quantum yields were impressive, in the range 60%–90%, especially strong in the case of the CsPbBr₃ films. In the blue, green, and orange spectral regions, LEDs based on a ITO/ PEDOT:PSS/PVK/QDs/TPBi/LiF/Al (PVK:Poly(9-vinylcarbazole), TPBi: 2,2',2''-(1,3,5-Benzinetriyl)-tris(1-phenyl-1-H-benzimidazole), PEDOT:PSS(poly(ethylenedioxythiophene):polystyrene sulfonate)) stack led to perovskite nanocrystal LEDs having a highest luminances of 528 cd m⁻², with EQE of 0.09%. The insulating organic ligands on the surface of nanocrystals suppressed – in these early studies – the efficient injection of current, accounting for these initial device performance levels.

Replacing these long ligands (usually oleylamine (OAm) and oleic acid (OA), used for protecting the surface of CsPbX₃), with shorter ligands, remains a challenge: it is imperative to achieve this without degrading or destabilizing perovskite nanocrystal films. Pan *et. al.* realized increased-stability films of CsPbX₃ NCs capped by using a halide ion pair (di-dodecyl dimethyl ammonium bromide (DDAB)), a relatively short ligand that facilitates carrier transport in NC films and enhances thereby LED device performance¹⁰⁹. The ligand-exchange strategy included an intermediate step to desorb protonated OAm. As a result of new ligand-exchange strategies, halide-ion-pair-capped CsPbBr₃ NCs have enabled fabrication of LEDs with the device structure indium

tin oxide (ITO)/ PEDOT:PSS/poly(9-vinylcarbazole)/NCs/TPBi/LiF/Al and achieved a maximum EQE and luminance of 3% and 330 cd m⁻², respectively.

Further progress toward CsPbBr₃ perovskite nanocrystal LEDs was made by Zeng and co-workers, who balanced surface passivation and carrier injection by controlling ligand density on perovskite nanocrystals¹²³. Using a hexane/ethyl acetate mixed solvent system, the authors controlled the surface ligand density: excess ligands had previously led to films with poor carrier injection and transport in device; while insufficient ligands caused the nanocrystals to have low PLQY and poor stability. The mixture of hexane/ethyl acetate was found to achieve improved control over the ligand density on nanocrystal surfaces, mainly due to the relationship between the polarity of solvents and the ionicity of perovskites. Perovskite nanocrystal LED performance reached > 6% in EQE and an emission peak of 512 nm. Mixed-cation strategies in perovskites have also employed nanocrystals based on FA_(1-x)Cs_xPbBr₃¹²⁴: the composition FA_{0.8}Cs_{0.2}PbBr₃ led to LEDs exhibiting an increased luminance of 55,000 cd m⁻² and a current efficiency exceeding 10 cd A⁻¹.

Most recently, core-shell CsPbBr₃ films were created using one-step precursor coating¹²⁵. The QDs were of small size (4.5 nm) and thus confined injected electron-holes. This enables green perovskite LEDs with EQE exceeding 15%.

Red-emitting CsPbI₃ nanocrystals have been shown phase transformation into a non-luminescent, wide-bandgap 1D polymorph phase, and MAPbI₃ exhibits poor chemical stability. Seeking to overcome this issue, Kovalenko and co-workers pursued a facile colloidal synthesis that led to FAPbI₃ and FA-doped CsPbI₃ nanocrystals having a uniform size distribution. These exhibited dramatically higher robustness than the corresponding MA and Cs only perovskites having similar sizes and morphologies¹²⁶. The FAPbI₃ nanocrystals have shown a cubic crystal

structure, while the $\text{FA}_{0.1}\text{Cs}_{0.9}\text{PbI}_3$ nanocrystals had an orthorhombic structure and the PLQY reached 70% and spanned the red (690 nm, $\text{FA}_{0.1}\text{Cs}_{0.9}\text{PbI}_3$) and near-infrared (780 nm, FAPbI_3) regions. The PLQY was stable for several months both in the colloidal state and in films. An EQE of 2.3% at current density 0.67 mA cm^{-2} was achieved in these FAPbI_3 nanocrystal LEDs.

Nanocrystals based on organic-inorganic hybrid nanocrystals have also been advanced in LEDs. Perovskites based on formamidinium lead bromide perovskite (FAPbBr_3) nanoparticles were improved with the aid of surface engineering¹²⁷. Work with the ligand allowed researchers to charge injection. They provided a current efficiency of 9 cd/A in LED, an important milestone. Researchers also advanced MAPbBr_3 nanoparticles having dimensions exceeding the exciton Bohr diameter (DB, regime beyond quantum size) by using a multifunctional buffer hole injection layer¹²⁸. These led to PLQYs exceeding 60% and did not rely on complex post-treatments nor multilayers. They gave an impressive current efficiency of 15.5 cd/A.

Self-assembly of 3D FAPbBr_3 nanocrystals of graded size – mixed micro-platelets of octylammonium lead bromide perovskites – were synthesized by Chin *et. al.*, enabling an energy cascade that yielded high efficiencies in green-emitting LEDs¹²⁹ (Figure 20). Transient optical spectroscopy revealed an energy cascade from high-bandgap 2D $(\text{OA})_2(\text{FA})_{n-1}\text{Pb}_n\text{Br}_{3n+1}$ platelets into progressively lower-bandgap FAPbBr_3 NCs, giving rise to high luminescence efficiency. Mesoscopic thin films comprising large plate-like domains of $(\text{OA})_2(\text{FA})_{n-1}\text{Pb}_n\text{Br}_{3n+1}$ were sandwiched between electron and hole transporting layers that enabled an EQE of 13.4% and $56,000 \text{ cd m}^{-2}$ luminance.

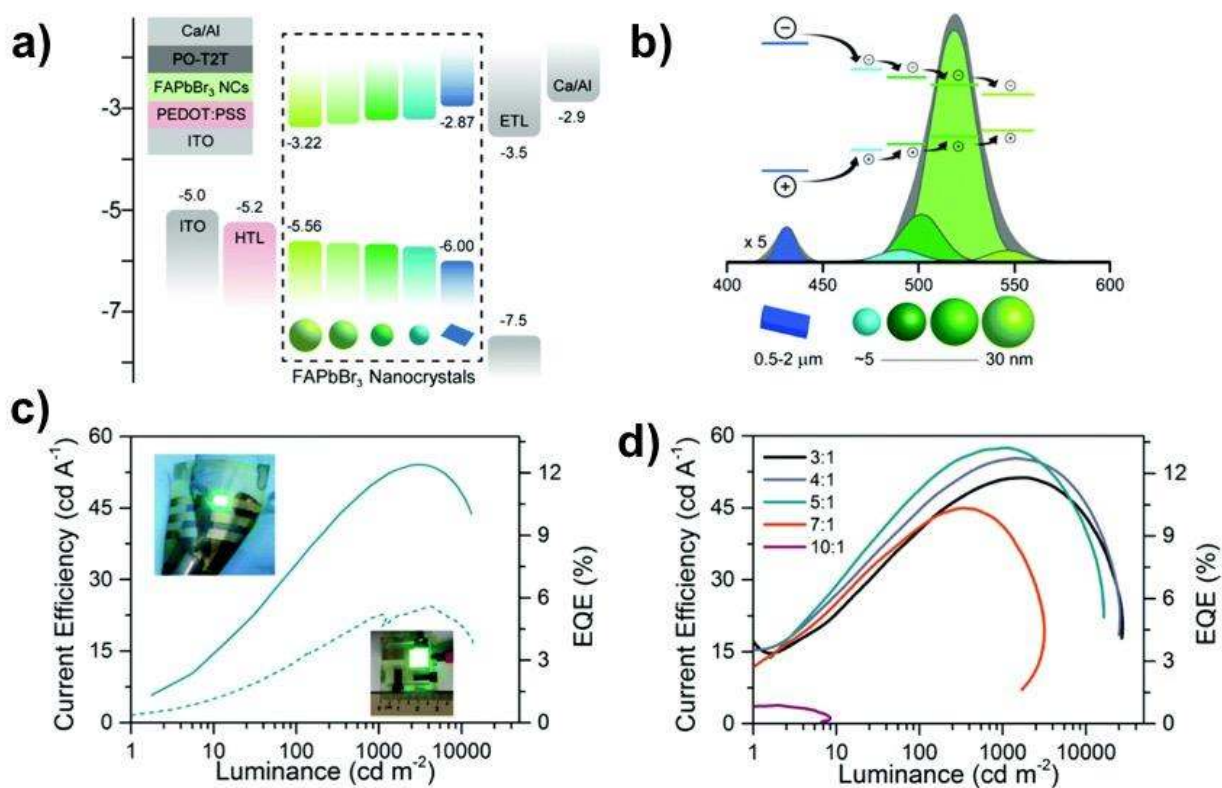


Figure 20. a) Band diagram of perovskite nanocrystal LEDs with energy cascade materials. b) The energy cascade from 2D microplatelets to FAPbBr₃ nanocrystals of graded size, where the deconvolution of the steady-state PL spectrum clearly displays the different PL contribution at varying nanocrystal sizes. c) Current efficiency/EQE versus luminance of flexible (3 mm²) and large area (95.2 mm²) LED devices. d) Characteristic current efficiency/EQE versus luminance¹²⁹. Reprinted with permission from ref 132. Copyright 2018, Royal Society of Chemistry.

4.2 Engineering Perovskite LEDs Towards High Efficiency

Numerous approaches used to improve perovskite LED efficiency, in addition to those focused on enhancing PLQY and/or film morphology or composition, have relied on improving electron and/or hole injection. We discuss strategies that improve perovskite LEDs by engineering

interfacial layers in device structures, and differences of perovskite LEDs compared with alternative thin film quantum dot LEDs (QLEDs) and organic LEDs (OLEDs).

4.2.1 Engineering Interfacial Layers

In the early stage of developing perovskite LEDs, device architectures were inspired from perovskite solar cells: they often employed ITO/TiO₂/perovskite/F8 (poly(9,9'-dioctylfluorene)/MoO₃/Ag; and also leveraged inverted structures such as ITO/PEDOT:PSS/perovskite/TPBi/LiF/Al (Figure 21). Wide-bandgap ZnO nanocrystals have been employed as electron-transporting / hole-blocking layers in solar cells and LEDs because of the combination of high electron mobility, excellent optical transparency, and a deep valence-band energy level. However, perovskites deposited atop ZnO decompose due to the residual hydroxyl groups and acetate ligands on the surface of alkaline ZnO¹³⁰.

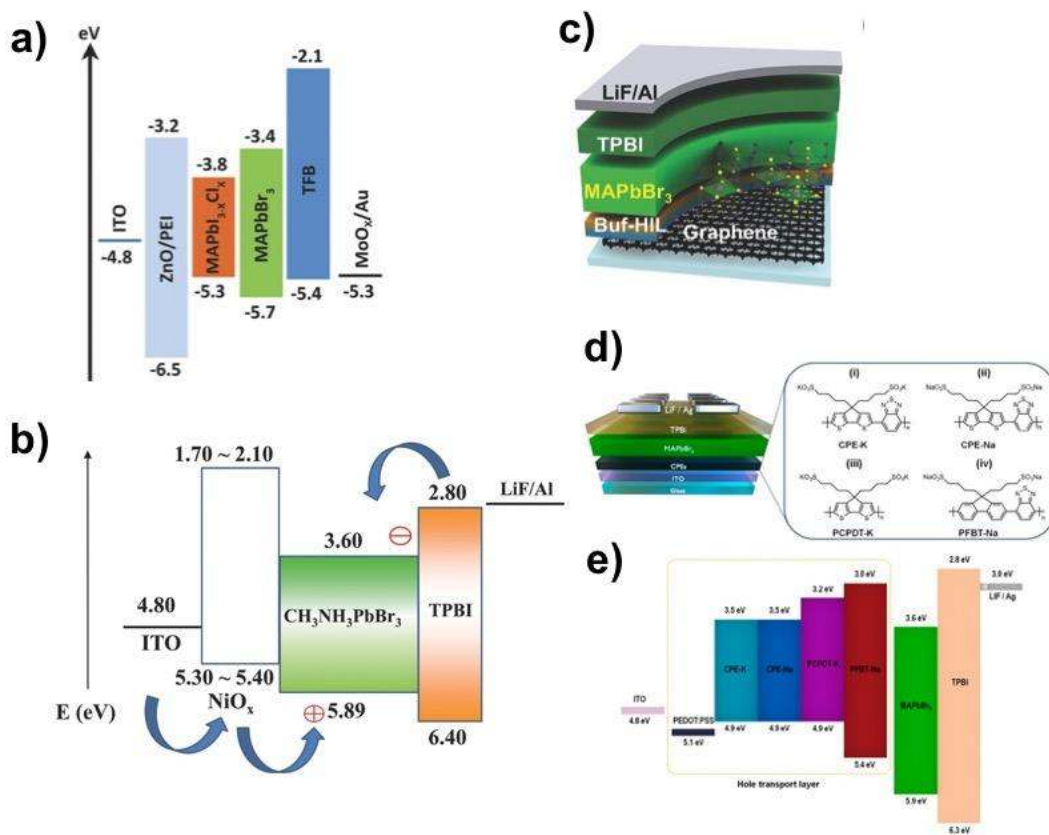


Figure 21. a) Flat-band energy level diagram of perovskite LEDs using modified ZnO using PEI¹³¹. Reprinted with permission from ref 134. Copyright 2015, Wiley-VCH. b) Energy diagram of perovskite devices using NiO_x as a HIL¹³². Reprinted with permission from ref 135. Copyright 2016, Wiley-VCH. c) Device structure of perovskite LED with graphene electrode and MAPbBr₃ emitter¹³³. Reprinted with permission from ref 136. Copyright 2017, Wiley-VCH. d) Schematic illustrations of perovskite LED devices with various conjugate polymers as HIL and e) related energy diagrams¹³⁴. Reproduced from ref 137. Copyright 2018, American Chemical Society.

Wang *et. al.* developed perovskite LED structures that incorporate a multifunctional polyethyleneimine (PEI) interlayer between the electron transporting layer and the perovskite layer¹³¹. Deposition of the PEI interlayer on top of ZnO following washing with N, N-dimethylformamide (DMF) enhanced the quality of the perovskite film during crystallization. The structure ultimately combined (ITO)/PEI-modified zinc oxide (ZnO, 20 nm)/ CH₃NH₃PbI_{3-x}Cl_x (50 nm)/poly(9,9-dioctyl-fluorene-co-N-(4-butylphenyl)diphenylamine)(TFB, 25 nm)/molybdenum oxide (MoO_x, 8 nm)/gold (Au, 100 nm). Using this interfacial engineering approach, the authors achieved green-emitting perovskite LEDs exhibiting a maximum luminous efficiency of 4.0 lm W⁻¹ at a maximum luminance of 20 000 cd m⁻² and a low voltage of 2.8 V.

The low efficiency observed in perovskite LEDs was traced to high leakage current due to poor perovskite morphology, and also to high nonradiative recombination at interfaces and perovskite grain boundaries that led to imbalanced charge injection. Zhang *et. al.* incorporated a small amount of MA into the CsPbBr₃ lattice; and also deposited a hydrophilic and insulating polyvinylpyrrolidone atop the ZnO electron-injection layer; all to overcome these issues¹³⁵.

Perovskite LEDs that used this strategy exhibited a high brightness of 91,000 cd m⁻² and

an EQE of 10.4% when the mixed-cation perovskite $\text{Cs}_{0.87}\text{MA}_{0.13}\text{PbBr}_3$ was used as the emitting layer. The polymer buffer layer and the MABr additive significantly reduced the injection current in device, suppressed current leakage, and enhanced charge injection balance. The turn-on voltage was also slightly increased after inserting a (thin but insulating) polymer buffer layer.

A suitably-designed *n*-type semiconductor consisting of Ca-doped ZnO nanoparticles was then developed for use as the electron transport layer in perovskite nanocrystal LEDs. The bandstructure of ZnO was modulated via Ca doping, creating a cascade of conduction energy levels from the cathode to the perovskite. The electron mobility was observed to increase progressively with increased doping of Ca in the ZnO nanoparticles. The carrier mobility in undoped ZnO was found to be $2.4 \times 10^{-3} \text{ cm}^2 \text{ V}^{-1} \text{ s}^{-1}$, and increased with the Ca doping level to a peak value of $\mu_{\text{max}} = 5.7 \times 10^{-2} \text{ cm}^2 \text{ V}^{-1} \text{ s}^{-1}$ at 50% doping. Red-emitting perovskite LEDs exhibited significantly improved luminance with 19 cd A^{-1} and EQE of 5.8%.

In the inverted device structure, TPBi is a widely-employed electron injection layer. Yan and co-workers used the blended electron injection layer B3PYMPM (4,6-bis(3,5-di(pyridin-3-yl)phenyl)-2-methylpyrimidine) and TPBi to tune the energy barrier between the ETL and the perovskite¹³⁶. In devices with TPBi as an ETL, the low electron conductivity ($4.2 \times 10^{-10} \text{ S cm}^{-1}$) and high energy barrier for electron injection caused by the high LUMO level of TPBi led to a higher driving voltage than in the B3PYMPM ETL device. PeLEDs with mixed ETLs showed reduced driving current density and an EQE_{max} of 12.9%, with a high η_{max} of 30.4 lm W^{-1} at high brightness above 1000 cd m^{-2} .

The judicious selection of hole transporting layers is important to balance charge injection and to form an ohmic contact with the active layer. The polymer F8, which has a deep ionization potential and a shallow electron affinity, was used to confine holes within the perovskite active

layer, blocking electron egress. The high-work function MoO₃/Ag anode provided ohmic hole injection into the device¹³⁷. Many perovskite LEDs and solar cells rely on expensive, unstable, and low-conductivity fluorenes for charge transport, such as spiro-OMeTAD (2,2',7,7'-tetrakis(N, N-di- p -methoxyphenylamine)-9,9'-spiro-bifluorene) or F8¹³⁸. Exploring new electrode materials that overcome these limitations is an important challenge. Dan and co-workers used atomic layer-deposited ZnO films that formed at 60 °C and were deposited directly onto MAPbBr₃ perovskite¹³⁹. The electron injection barrier with the perovskite was reduced by incorporating Mg into ZnO to produce Zn_{1-x}Mg_xO. This decreased the electron affinity from -3.6 to -3.35 eV relative to vacuum and reduced the LED turn-on voltage.

Insertion of a buffer layer between electrode and semiconducting layers is a widely-employed strategy to control interfacial properties and ultimately improve device characteristics. Perovskite nanocrystal films on conventional PEDOT:PSS hole injection layers (HILs) often led to an inhomogeneous surface morphology. Pinholes and aggregated nanoplatelets reduced LED device efficiency. Also, exciton quenching by PEDOT:PSS at the PEDOT:PSS/perovskite film interface needed to be addressed – and interface engineering provided an attractive approach. Kim *et. al.* used a multifunctional HTL to minimize exciton quenching at the perovskite/HTL interface¹²⁸. With the above strategies, a high PLQY (~60%) in compact perovskite particle films was achieved without further post-treatment; and LEDs based on colloidal perovskite nanocrystals reached a high current efficiency of 15.5 cd/A.

Other attempts at transport layers include the use of inorganic NiO_x as an hole injection layer. Chih *et. al.* reported that a NiO_x electrode interlayer enhances emission from a MAPbBr₃ film active layer, this finding attributed to suitable hole level alignment and improved electron blocking – together, that increased the probability of radiative recombination in the active layer¹⁴⁰.

Conjugated polyelectrolytes have been employed as the hole injection layer by Friend and co-workers¹³⁴. PCPDT-K (poly[2,6-(4,4- bis-potassium butanylsulfonate)-4H-cyclopenta-[2,1-b;3,4-b']-dithiophene)]) polyelectrolytes transfer holes efficiently, block electrons, and reduce luminescence quenching at the perovskite/PCPDT-K interface. Perovskite LEDs with PCPDT-K demonstrated a factor of approximately 4 increase in EQE compared to control devices that used PEDOT:PSS, reaching EQE of 5.7%, and with improved device stability.

Table 1. Device performance of perovskite LEDs (from blue to near-infrared wavelengths)

	Perovskite materials	Device structure	EL Wavelength (nm)	Max. EQE (%)	Max. Brightness (cd m ⁻²) R _{max} (W sr ⁻¹ m ⁻²)	Ref.
Blue	(PEA) ₂ PbBr ₄	ITO/PEDOT:PSS/perov/TPBi/Ca/Al	410	0.04	-	141
	IPA:PEA ₂ MA:Cs _{n-1} Pb _n Br _{3n+1}	ITO/PEDOT:PSS/perov/TPBi/LiF/Al	490	1.5	2,480	142
	Cs ₁₀ MA _{0.17} FA _{0.83} Pb(Cl _{1-x} Br _x) ₃	ITO/ZnO/perov/NPD/MoO ₃ /Al	475	1.7	3,567	143
	CsPbX ₃ NCs	ITO/PEDOT:PSS/PVK/perov/TPBi/LiF/Al	490	1.9	35	144
	CsMnPb(Br _{1-x} Cl _x) ₃	ITO/PEDOT:PSS/TFB:PFI/perov/TPBi/LiF/Al	466	2.12	245	145
	CsPbCl _{0.9} Br _{2.1}	ITO/PEDOT:PSS/perov/TPBi/LiF/Al	480	5.7	3,780	146
Green	MAPbBr ₃	ITO/PEDOT:PSS:PFI/perov/TPBi/LiF/Al	540	0.13	417	147
	MAPbBr ₃ :PIP	ITO/PEDOT:PSS/perov/F8/Ca/Ag	534	1.2	200	148
	FAPbBr ₃	ITO/ZnO/perov/poly-TPD/MoO ₃ /Al	540	1.16	13,062	149
	CsPbBr ₃ /PEO	ITO/PEDOT:PSS/perov/TPBi/LiF/Al	521	4.26	53,525	150
	CsPbBr ₃ NCs	ITO/ PEDOT:PSS/poly-TPD/perov/TPBi/LiF/Al	515	6.27	15,000	151
	Cs ₁₀ MA _{0.17} FA _{0.83} Pb(Br _{1-x} I _x) ₃	ITO/ZnO/perov/NPD/MoO ₃ /Al	569	7.3	19,420	115
	(PEABr) _{0.2} MAPbBr ₃	ITO/PVK/perov/TPBi/LiF/Al	515	7.0	11,400	152
	MAPbBr ₃	Glass/PEDOT:PSS:PFI/perov/TPBi/LiF/Al	542	8.53	10,000	153
	(BABr) _{0.2} MAPbBr ₃	ITO/PVK/perov/TPBi/LiF/Al	513	9.3	2,900	42
	Cs _{0.87} MA _{0.13} PbBr ₃	ITO/ZnO/PVP/perov/CBP/MoO ₃ /Al	520	10.43	91,000	135

	MAPbBr ₃ /Phenylmethylanine	ITO/PEDOT:PSS/perov/TPBi/LiF/Al	535	12.1	55,400	154
	MAPbBr ₃ NCs	ITO/PEDOT:PSS/perov/B3PYMPM:TPBi/ B3PYMPM: Cs ₂ CO ₃ /Al	524	12.9	22,830	155
	(OA) ₂ (FA) _{n-1} Pb _n Br _{3n+1} and FAPbBr ₃	ITO/PEIE/perov/PO-T2T/Ca/Al	530	13.4	56,143	129
	PEA ₂ CsPb ₂ Br ₇	ITO/PVK/perov/TPBi/LiF/Al	512	13.9	8,789	156
	PEA ₂ (FAPbBr ₃) _{n-1} PbBr ₄	ITO/PEDOT:PSS/perov/TPBi/LiF/Al	530	14.36	14,000	157
	CsPbBr ₃ /PEABr/polyethyleneglycol	ITO/PEDOT:PSS/perov/TPBi/LiF/Al	514	13.14	45,990	158
	CsPbBr ₃ /PEABr/1,4,7,10,13,16- hexaoxacyclooctadecane	ITO/poly-TPD/perov/TPBi/LiF/Al	510	15.5	7,000	159
	CsPbBr ₃ /PPABr NCs	ITO/PEDOT:PSS/PVK/perov/TPBi/LiF/Al	512	15.2	18,600	160
	CsPbBr ₃ /ZnBr ₂ NCs	ITO/PTAA/PVK/perov/TPBi/LiF/Al	518	16.5	76,940	161
	CsPbBr ₃ /MABr	ITO/PEDOT:PSS/perov/PMMA/B3PYMPM/TPBi/LiF/Al	525	20	14,000	162
Red	CsPbI ₃ NCs	ITO/ZnO/perov/TFB/MoO ₃ /Ag	698	5.7	206	163
	CsPbI _{2.25} Br _{0.75} NCs	ITO/ZnO/perov/TFB/MoO ₃ /Ag	619	1.4	1,559	163
	MAPbI _{1.05} Br _{1.95}	ITO/PEDOT:PSS/perov Ca:ZnO/Ca/Al	635	5.8	1,000	164
	CsPbI ₃ /Ag doped NCs	ITO/PEDOT:PSS/perov/TCTA/MoO ₃ /Au	690	11.2	1,106	165
	CsPbI ₃ /Sr doped NCs	ITO/ZnO/PEI/perov/TCTA/MoO ₃ /Au	691	13.5	1,152	166
	CsPbBr _x I _{3-x}	ITO/PEDOT:PSS/poly-TPD/perov/TPBi/LiF/Al	649	21.3	794	167
NIR	MAPbI _{3-x} Cl _x	ITO/TiO ₂ /perov/F8/MoO _x /Au	773	0.76	^R 13.2	168
	MAPbI _{3-x} Cl _x	ITO/ZnO/PEIE/perov/TFB/MoO _x /Au	768	3.5	^R 28	169

	(FPMAl) _{0.2} MAPbI ₃	ITO/polyTPD/perov/TPBi/LiF/Al	749	7.9	^R 72	152
	PEA ₂ MA ₄ Pb ₅ I ₁₆	ITO/TiO ₂ /perov/F8/MoO _x /Au	750	8.8	^R 80	170
	(BAI) _{0.2} MAPbI ₃	ITO/polyTPD/perov/TPBi/LiF/Al	748	10.4	^R 30	42
	FAPbI ₃ /5AVA	ITO/ZnO:PEIE/perov/TFB/MoO _x /Au	800	20.7	^R 390	171
	FAPbI ₃ /EDEA	ITO/ZnO:PEIE/perov/TFB/MoO ₃ /Au	800	21.6	^R 308	172

a) ITO = indium tin oxide; PEDOT:PSS = poly(3,4-ethylenedioxythiophene:polystyrene sulfonate); TPBi=[2,2',2''-(1,3,5-benzinetriyl)-tris(1-phenyl-1-H-benzimidazole)]; PEIE = polyethylenimine ethoxylated; TFB=Poly(9,9-dioctylfluorene-alt-N-(4-sec-butylphenyl)-diphenylamine); NPD = N,N'-bis(naphthalen-1-yl)-N,N'-bis(phenyl)benzidine; poly-TPD= Poly(4-butylphenyl-diphenyl-amine); CBP = 4,4-N,N'-dicarbazole-1,1'-biphenyl; B3PYMPM=4,6-Bis(3,5-di(pyridin-3-yl)phenyl)-2-methylpyrimidine; TPD = N,N'-bis(3-methylphenyl)-N,N'-diphenylbenzidine; PVK = poly(9-vinylcarbazole); PPA,Br-phenylalanine bromide; EDEA=2,2'-(ethylenedioxy)diethylamine; TCTA=4,4,4''-tris(carbazol-9-yl)triphenylamine; 5AVA= 5-aminovaleric acid, b) R = radiance

4.2.2 Comparison of Perovskite LED with QLED and OLEDs

We turn now to a discussion of traditional II-VI quantum dots and organic materials compared to perovskites in light-emitting applications (Table 2). Quantum dots' tunable bandgap, as governed by the quantum size effect, also poses challenges, for it mandates a high monodispersity in the population of dots.

A precisely tailored spectrum can be used to generate a specific color temperature of white light. The quality of white light is measured via the correlated color temperature (CCT) and color rendering index (CRI). For lower-CCT illumination at high temperature, high luminous efficiency and color quality are hard to achieve: the red luminophores require a very narrow emission linewidth. Conventional red phosphors have emission spectra that are very broad (>60 nm FWHM). The narrow spectral emission (~30 nm FWHM) of QDs offer more selective optical down-conversion of a portion of a backlight's bluer emission into redshifted light, leading to a CRI of >90% and a superior CCT of 2,700 K while maintaining a high luminance efficiency¹⁷³. This allows QDs to increase color quality while lowering power consumption in solid state light sources. QDs can also be utilized as backlights in high-color-quality liquid-crystal displays.

Table 2. Comparison of perovskite LED, QD LED and OLEDs.

	PeLEDs	QD LEDs	OLEDs
FWHM (nm)	~20	~28	>70
ELQY ^{red} (%)	13 ¹⁷⁴	20.5 ¹⁷⁵	29 ¹⁷⁶
L _{max} ^{red} (cd/m ²)	82Wsr ⁻¹ m ⁻² 43	42,000 ¹⁷⁵	1,000,000 ¹⁷⁶
ELQY ^{green} (%)	14 ¹⁵⁷	14.5 ¹⁷⁷	73,100 ¹⁷⁸
L _{max} ^{green} (cd/m ²)	9120 ¹⁵⁷	10,000 ¹⁷⁷	27.5 ¹⁷⁸
ELQY ^{blue} (%)	1.5 ¹⁷⁹	10.7 ¹⁷⁷	36.7 ¹⁸⁰
L _{max} ^{blue} (cd/m ²)	2480 ¹⁷⁹	4,000 ¹⁷⁷	10,000 ¹⁸⁰
Operational stability (h)	10 ¹⁸¹	100,000 ¹⁷⁵	600,000 ¹⁸²
Color tunability	400 nm ~ near IR		400 nm~700nm

QDs do come with challenges. The importance of monodispersity in QDs for electronics arises because a rough energy landscape impedes transport and enhances recombination due to the presence of small-bandgap inclusions. Charging can occur when under current injection – and this charging retards further injection, reducing electroluminescence (EL). The timescales associated with QD charging range from minutes to days¹⁸³. While the PLQY of QDs solution routinely often exceeds 95%, QDs deposited in a close-packed thin film exhibit lower – often by one order of magnitude – luminescence efficiency. Embedding QDs into an insulating polymer matrix decreases QD emission quenching^{184,185}; however, the electrical conductivity in these QD-polymer composites is impeded by the low conductance of the wide bandgap polymers. Förster resonant energy transfer (FRET) between closed-packed QDs can also reduce the PLQY of QD films¹⁸⁶.

While QDs are beginning to be deployed in applications such backlights in displays, organic LEDs (OLEDs) are already a multibillion dollar industry, with applications in displays, lighting, and consumer devices¹⁸⁷. Most applications of OLEDs could benefit from a solution-processed approach, (instead of the prevailing vacuum sublimation process) where roll-to-roll solution-processing and inkjet printing could potentially be employed¹⁸⁸⁻¹⁹¹. To achieve this, new high-performance active materials that are solution-processable would accelerate adoption. Efficiency roll-off represents another remaining area for improvement in OLEDs. This corresponds to both a lowered power conversion efficiency as well as added electrical stress to achieve a given brightness, which works against device lifetime.

Perovskites offer pathways to color-saturated emission in view of their narrow emission linewidths (<30 nm) and manifest the possibility for future high-color purity emitters. Ready wavelength tuning, and efficient charge injection/transport property with perovskites, have been studied as promising features to enable next-generation light emitters. Perovskite LEDs also have

shown sub-bandgap turn-on voltages, implying the possibility of achieving low operating voltages and high power conversion efficiencies in display applications. Perovskite LEDs, since they can be processed from the solution phase, can potentially be inkjet printed. Processing temperatures will likely be quite low (less than 150 °C), making fabrication compatible with flexible and lightweight plastic substrates.

4.3 Stability of Perovskite LEDs

The device stability in QD LEDs exhibit on the order of 100-1,000 hours when operated at relatively modest brightness (1000 cd m^{-2})¹⁷⁵. In contrast, the device stability of state-of-art OLEDs is in the range of 10,000 to 100,000 hours. Instability in early-generation OLED was triggered by dark-spot effects; however, device encapsulation and optimization enabled the community to overcome these issues¹⁹². The stability of lead halide based perovskite LEDs remains a major issue in this early-stage materials platform¹⁹³. Here we will discuss this challenge including recent studies towards increased device stability.

4.3.1 Status and Mechanisms Underpinning Stability in Perovskite LEDs

Perovskite solar cells' device lifetimes now exceeds one thousand hours under continuous operation while biased at the maximum power point.¹⁹⁴ Perovskite LEDs are at a less mature stage from the point of view of reliability: often devices have ~ sub-hour consistent operation under continuous electrical stress before degradation becomes observable at a brightness level higher than 100 cd m^{-2} .

Some issues in perovskite LEDs are likely shared with perovskite solar cells. From PV it became clear that some compositions of thin films lack chemical and structural stability especially in the presence of moisture or heat. The strong ionic character of perovskites is linked to phase segregation and ion migration as well as to various electrochemical reactions¹⁹⁵⁻¹⁹⁸ (Figure 22).

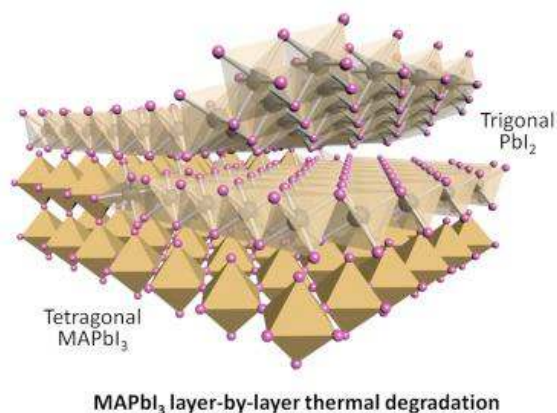
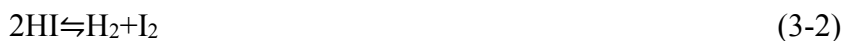
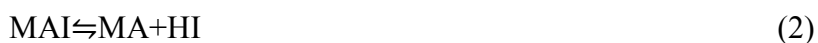


Figure 22. Structural degradation in MAPbI₃¹⁹⁹. Reprinted with permission from ref 162.

Copyright 2017, Wiley-VCH.

In early 2014, stability issues in perovskites for PV gained the attention of a number of research groups. Fundamental studies on instability in perovskite thin films in the presence of moisture and the surrounding environment were reported by Niu *et. al*²⁰⁰. Device fabrication needs to be carried out under controlled atmospheric conditions and with a humidity of <1% as shown by Gratzel and co-workers²⁰¹. The degradation process was proposed to follow this route:



In reaction (1), MAPbI₃ decomposes into MAI and PbI₂ in the presence of H₂O (Figure 23). In this process, the equilibrium constant is $k(1) = c(\text{MAI})$ and the Gibbs free energy is $\Delta G(1) = -RT \ln k(1)$. In reaction (2), MAI solution decomposes into MA solution and HI solution. Then

the equilibrium constant is $k(2) = c(\text{MA}) \times c(\text{HI})/c(\text{MAI})$ and Gibbs free energy is $\Delta G(2) = -RT \ln k(1)$. In reaction (3), there are two ways for HI to react. (3-1) represents the redox reaction and can move forward readily. (3-2) represents the photochemical reaction - experimental evidence revealed that HI can easily decompose into H_2 and I_2 under optical excitation. Ab initio molecular dynamics simulations further predicted surface reconstruction and light-assisted formation of hydrated species of $\text{MAPbI}_3 \cdot \text{H}_2\text{O}$ – a finding that agrees with the observation that exposure to water and light accelerates the degradation of perovskites^{202,203}.

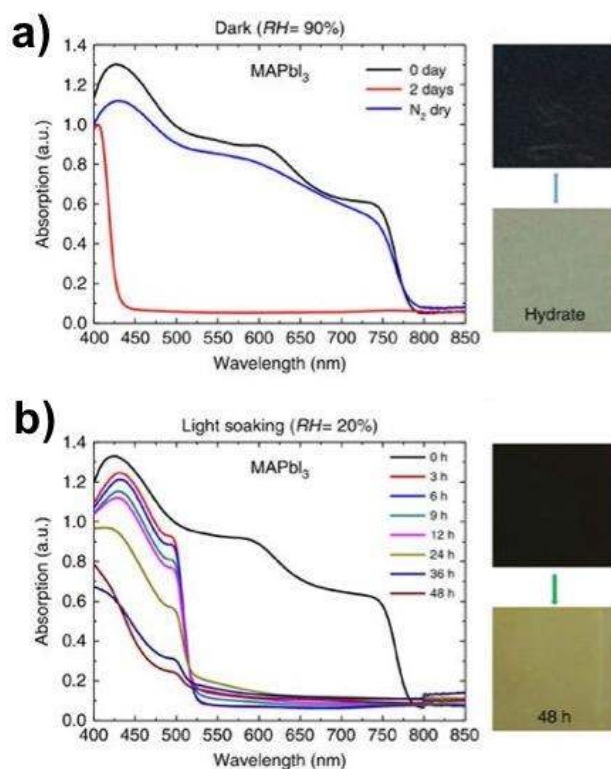


Figure 23. Hydration and light-induced degradation of perovskite materials. a) Absorption spectra and pictures of the MAPbI₃ perovskite film. Time evolution of absorption spectra and pictures of MAPbI₃ (h) before and (i) after degradation under light soaking at 20% RH²⁰⁴. Reprinted with permission from ref 167. Copyright 2016, Nature Publishing Group.

Charge trapping at the interface between perovskites and charge extraction materials are responsible for irreversible degradation due to moisture²⁰⁴. To understand charge-driven degradation mechanisms, it was important to develop controlled stability experiments both for commonly used MAPbI₃, which is known to form structurally distorted tetragonal crystals, and also for mixed perovskite materials having more enhanced structural stability. It was found that the mixed perovskite MA_{0.6}FA_{0.4}PbI_{2.9}Br_{0.1} still degraded, although its degradation speed was slower than that of conventional MAPbI₃. It was further shown that the irreversible degradation of the perovskites was triggered by trapped charges.

Oxygen, in addition to moisture, can also trigger degradation²⁰⁵. Darkening in PL also involved interaction with photogenerated carriers. The dynamics of PL in MAPbI₃ films were studied under continuous photoexcitation. The activation and darkening of the PL intensity was observed, and this was found to depend strongly on optical pump characteristics. When the optical photoexcitation intensity was increased, the perovskites PL increased linearly, and both activation and darkening dynamics in perovskite film is increased.

Photoactivation fills sub-gap trap states that otherwise limit the PL of the perovskite²⁰⁶. These states can be either shallow or deep, and photoactivation is more efficient in the presence of O₂ than it is with N₂. When and if the photoactivation process is in fact relevant to the filling of charge traps, oxygen plays a role in the process. Perovskite films under prolonged optical excitation may photodarken, a fact attributed to the decomposition of the perovskites under excitation. The hydrated compounds are easily formed upon photoexcitation, and this leads to a weakening of hydrogen bonds between PbI₆ and organic cations. This ultimately promotes the formation of complexes between H₂O and PbI₆^{207,208}. Further research is required to understand the mechanisms of H₂O and O₂ in the photoactivated processes.

The mechanistic process of degradation has been studied using super-resolution luminescence micro spectroscopy²⁰⁹. The degradation of the MAPbI₃ crystal structure starts locally due to the collapse to the layered PbI₂ structure; and then spreads across the crystal. The migration of MA ions can distort the perovskite lattice, and this leads to the loss of the crystal structure.

In addition to instabilities in perovskite materials, device instabilities can also come from interfacial layers and electrical stress during operation of device. Ionic processes, such as halide segregation, can destroy perovskites and generate defects,²¹⁰ some of which are voltage-induced and others spontaneous. Some examples include the corrosion/oxidation of electrodes²¹¹⁻²¹⁴, degradation of charge-transport layers²¹⁵, and the formation of charge-accumulated interfaces²⁰⁴ and p-i-n junctions^{150,216-218}. Furthermore, the diffusion of metallic species from electrodes, the origin of which is still unclear, can cause a significant decrease in device efficiency and accelerate the degradation of perovskite LEDs.

4.3.2 Strategies to Improve LED Stability

To improve LED stability, several approaches have been used. Inorganic CsPbX₃ based perovskites have been shown to improve LED stability compared with MA based perovskites¹⁴³, a finding associated with their enhanced thermal, structural, and chemical stability. The high thermal stability of CsPbBr₃ may improve the operational stability of perovskite LEDs, by suppressing degradation caused by thermal stresses, including Joule heating. Schaller and co-workers reported temperature-dependent PL below 450 K strongly affected by halide composition²¹⁹.

Another strategy to improve perovskite stability involves the use of layered perovskite structures. Perovskites of composition (PEA)₂(MA)₂[Pb₃I₁₀] have shown increased stability against moisture, attributed in part to the hydrophobic nature of the PEA layers. Using a density

functional theory (DFT) approach, Quan *et al.* proposed that the introduction of PEA layers can increase quantitatively van der Waals interactions. These provide an increased formation energy corresponding to improved materials stability²⁶.

Recently, quasi-2D perovskite/poly(ethylene oxide) (PEO) composite thin films were reported as the light-emitting layer in work by Ma and co-workers²²⁰ (Figure 24). Controlling the molar ratios of organic (benzylammonium iodide) to inorganic salts (CsI and PbI₂), the group obtained luminescent quasi-2D perovskite thin films exhibiting tunable emission colors from red to deep red. LEDs with an emission peaking at 680 nm exhibited a brightness of 1392 cd m⁻² and an EQE of 6.2%. The EL intensity dropped by 20% relative following 4 hours of continuous operation; and these devices exhibited enhanced spectral stability.

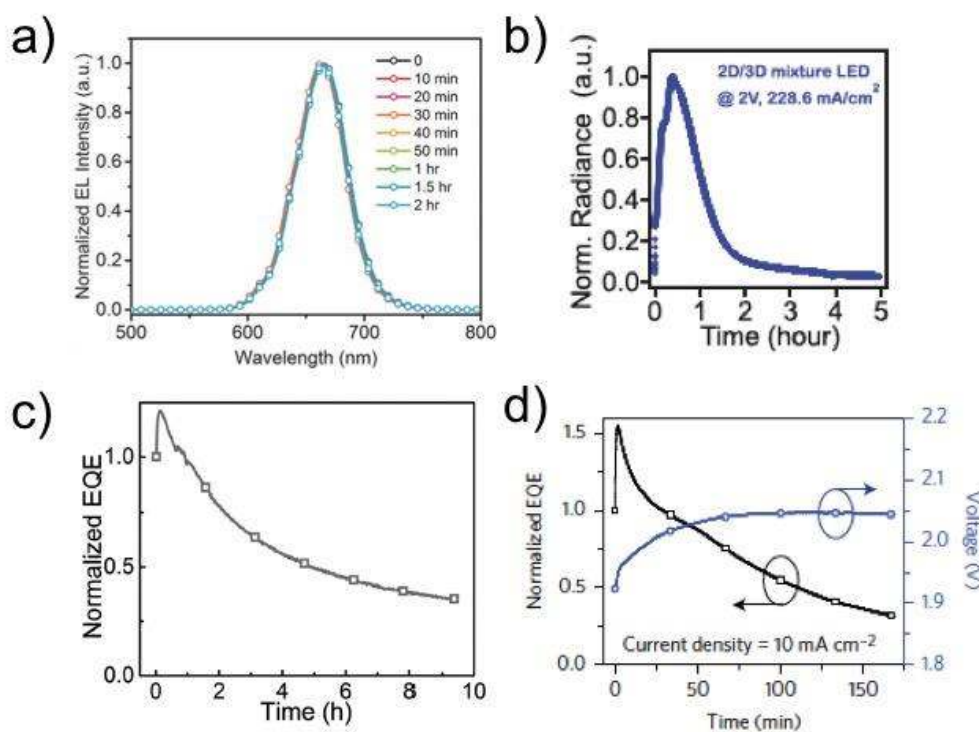


Figure 24. a) Perovskite LED spectral stability²²⁰ and b-d) device operational stability under constant bias^{43,117,221}. Reprinted with permission from ref 185. Copyright 2018, Wiley-VCH. Reprinted with permission from ref 43. Copyright 2018, Wiley-VCH. Reprinted with permission

from ref 120. Copyright 2016, Nature Publishing Group. Reprinted with permission from ref 186. Copyright 2017, Wiley-VCH.

Kim *et.al.*, reported the charge carrier recombination and ion migration induced by photo-excitation by analyzing steady-state and transient PL and photo-responsivity in perovskite nanoparticle films²²². These results indicate organic ligands in perovskite nanoparticle films efficiently prevent ion migration and ion-migration-induced defects. These efficient confinement of electron-hole pairs and prevention of ion migration in perovskite nanoparticle films induced high photo-stability, PLQY of the perovskite films.

5. Perovskites for Lasing

5.1 Optical Amplification Using Perovskites

Stimulated emission is the coherent photon emission process wherein an incident photon is amplified (gain) via downward radiative transitions from excited state levels. By studying charge transfer process in perovskite solar cells, researchers first observed stimulated emission in MAPbX₃ with the aid of ultrafast pump-probe spectroscopy².

Optical amplification, measured via gain per unit length (in cm⁻¹), can be studied by measuring the absorption spectra from the photoexcited gain medium. In perovskite thin films, optical gains have been reported²²³ in the range 3200 ± 800 cm⁻¹. This value is comparable to that of single-crystal GaAs, and agrees with the known high absorption coefficient of perovskite. Gain has been shown to be as long as 200 ps, with a threshold of ~ 16 $\mu\text{J cm}^{-2}$. When one varies the pump fluence, the emitted spectral intensity yields a threshold for amplified spontaneous emission (ASE). The luminescence becomes narrows and sharply increases above the ASE threshold. Reported ASE thresholds for halide perovskites are ranging from 12 $\mu\text{J cm}^{-2}$ under femtosecond excitation²²⁴ to

$60 \mu\text{J cm}^{-2}$ under nanosecond photoexcitation conditions²²⁵, and $7.6 \mu\text{J cm}^{-2}$ at pulse durations as long as 5 ns with a liquid crystal reflector²²⁶.

5.1.1 Original Reports of Perovskite Lasing

Solution-processed MAPbX₃ perovskite films were studied with an eye to lasing by Xing *et al.*²²⁴ (Figure 25). An increased pump fluence lead to the transition from spontaneous emission (SE) to ASE in MAPbI₃ thin film. Using the threshold fluence ($12 \pm 2 \mu\text{J cm}^{-2}$) and absorption coefficient ($\alpha = 5.7 \cdot 10^4 \text{ cm}^{-1}$ at 600 nm), the ASE threshold was calculated to be $\sim 1.7 \cdot 10^{18} \text{ cm}^{-3}$. The Auger recombination process in perovskites, dominant at high pump fluence, leads to lifetimes in the range of a few ps to ns, depending on the photogenerated charge carrier density. The low ASE threshold in perovskites is attributed in significant part to the low trap density in the best such films.

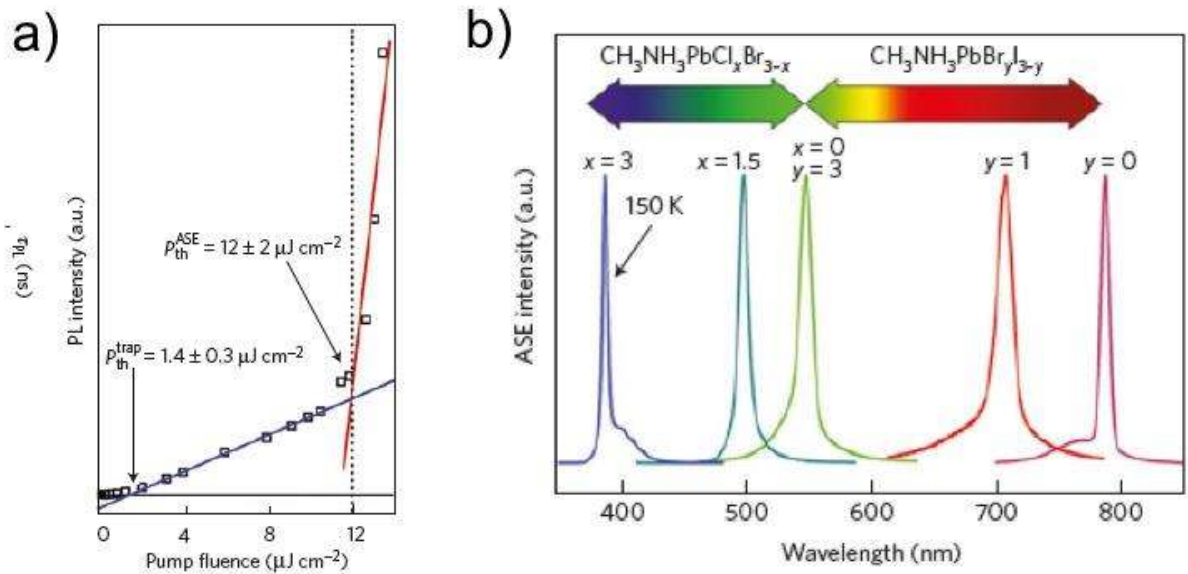


Figure 25. a) PL intensity of MAPbI₃ film as increase the pump fluence. b) ASE wavelength tunability across a wide visible wavelength range for the case of halide perovskite thin films²²⁴.

Reprinted with permission from ref 189. Copyright 2014, Nature Publishing Group.

The PLQY as a function of excitation fluence in $\text{CH}_3\text{NH}_3\text{PbI}_{3-x}\text{Cl}_x$ perovskite films was, as previously discussed, an impressive 70% at high excitation density. Friend and co-workers constructed and demonstrated the operation of vertical cavity lasers that employed a perovskite layer sandwiched between a dielectric mirror and a metal mirror¹⁰⁸.

The relation between the phase-transition of the perovskite film, and ASE mechanisms, was investigated by studying behavior in different phase states²²⁷. A sharp ASE peak with the maximum spectral intensity occurs at the temperature of 120 K. PL emission spectra show a notable variation of the spectral characteristics when moving from temperatures 120 K to 160 K, in which range the structural phase transformation from orthorhombic to tetragonal occurs. As the temperature exceeds 120 K, the lasing threshold continues to increase because of thermal broadening of the gain peak. Low-threshold ASE and lasing has also been reported from colloidal CsPbX_3 NCs having a 10 nm size²²⁸. Optical amplification in perovskite NCs was obtained with low pump thresholds ($5 \pm 1 \text{ mJ cm}^{-2}$) and across the visible spectral range (440–700 nm). Conformally-coated perovskite NCs on a high-finesse resonator, such as silica microspheres, have enabled the observation of whispering-gallery-mode lasing.

5.1.2 Effects of Perovskite Crystal Structures

MAPbI_3 exhibits a reversible phase transition between its tetragonal and cubic phases at $\sim 330 \text{ K}$, and is sensitive to oxygen, moisture and heat. As a result, all-inorganic CsPbX_3 has also been explored as an optical gain medium due to their narrow gain profiles and wavelength tunability²²⁸⁻²³¹.

A film consisting of close-packed CsPbBr_3 nanocrystals was photoexcited using a wavelength 400 nm in a stripe configuration. A narrower emission band located at 524.5 nm with FWHM of $\approx 5 \text{ nm}$ appears on the longer wavelength side when the pump intensity exceeds $\approx 22 \mu\text{J}$

cm^{-2} . These optical gain properties in CsPbBr_3 nanocrystals suggest a material of interest in lasing, especially in the green and blue spectral range, where II–VI group quantum dots show lower gain performance than their red counterparts²³². Nonradiative Auger recombination occurring at high excitation intensities has been recognized to be the main channel dissipating population inversion in quantum dots, hindering optical amplification. Excitation-intensity-dependent time-resolved PL measurements were performed on CsPbBr_3 nanocrystals to explore Auger recombination²²⁹. The PL decay of the CsPbBr_3 is relatively slow single-exciton recombination under low excitation intensities ($<4.5 \mu\text{J cm}^{-2}$), then a fast decay process emerges as the excitation intensity increases, corresponding to the Auger recombination, on the ~ 100 ps timescale.

ASE in the optically-pumped FAPbI_3 and MABr -stabilized FAPbI_3 films showed an impressively low threshold of $1.6 \mu\text{J}/\text{cm}^2$. FAPbI_3 films displayed more durable lasing emission than MAPbI_3 ²³³. The lasing threshold improved in FAPbI_3 films due to their low defect density and high thermal stability. High-quality low-dimensional single-crystals with lower defect densities and reduced scattering will support further threshold lowering.

The solution growth of high-quality single-crystal phase FAPbI_3 nanowires led to black-phase FAPbI_3 alloy nanowires in the cubic perovskite phase. These were made by incorporating a small amount of MABr into FAPbI_3 ²³⁴. Optically pumped lasing was reported from MABr -stabilized FAPbI_3 perovskites at room temperature with near-infrared (NIR) emission at ~ 800 nm, low lasing thresholds of a few $\mu\text{J}/\text{cm}^2$, and high quality factors of ~ 1500 . These FA-based perovskite NWs displayed improved photostability and wavelength tunability compared to MA-based perovskite NWs²³⁴.

Solution-processed lead-free Sn-based halide perovskites such as CsSnX_3 exhibit relatively poor photovoltaic performance²³⁵⁻²³⁸; however, they possess remarkable optical gain properties in

the NIR up to $\approx 1 \mu\text{m}$. Ultralow-threshold ($\approx 6 \mu\text{J cm}^{-2}$), large-gain (200 cm^{-1}) stimulated emission was seen in 20% $\text{SnF}_2\text{-CsSnI}_3$ samples, providing performance comparable to Pb counterparts. Transient spectroscopy on CsSnI_3 perovskite revealed that SnF_2 addition suppressed trap state, and that lasing originated from bimolecular recombination of free electron-holes with a high rate of $\approx 10^{-8} \text{ cm}^3 \text{ s}^{-1}$ (*i.e.*, 1–2 orders larger than MAPbI_3). Stable ($>20 \text{ h}$), room-temperature NIR coherent light emission (700–1000 nm) was achieved as a result. The ASE wavelength was tuned from 700 to 950 nm by varying bromide:iodide composition to obtain CsSnBr_3 , CsSnBr_2I , CsSnBrI_2 , and CsSnI_3 thin films.

Although multi quantum well structures of 2D layered perovskites exhibit strong light–matter interactions, room temperature optical gain in 2D layered perovskites have not been seen so far - likely a consequence of efficient nonradiative trapping of free excitons and/or biexcitons²³⁹.

Recently, $(\text{OA})_2(\text{MA})_{n-1}\text{Pb}_n\text{Br}_{3n+1}$ based mixed lower-dimensional perovskite layers (with larger bandgaps and smaller refractive index acting as cladding layers) provided enhanced exciton and photon confinement for higher-dimensional perovskite layers (the active layers)²⁴⁰ (Figure 26). The achievement of low-threshold ($\sim 7.8 \mu\text{J cm}^{-2}$) lasing from near-3D to quasi-2D perovskites is related to efficient exciton localization from lower-dimensional perovskite layers to the active layers in microplatelets.

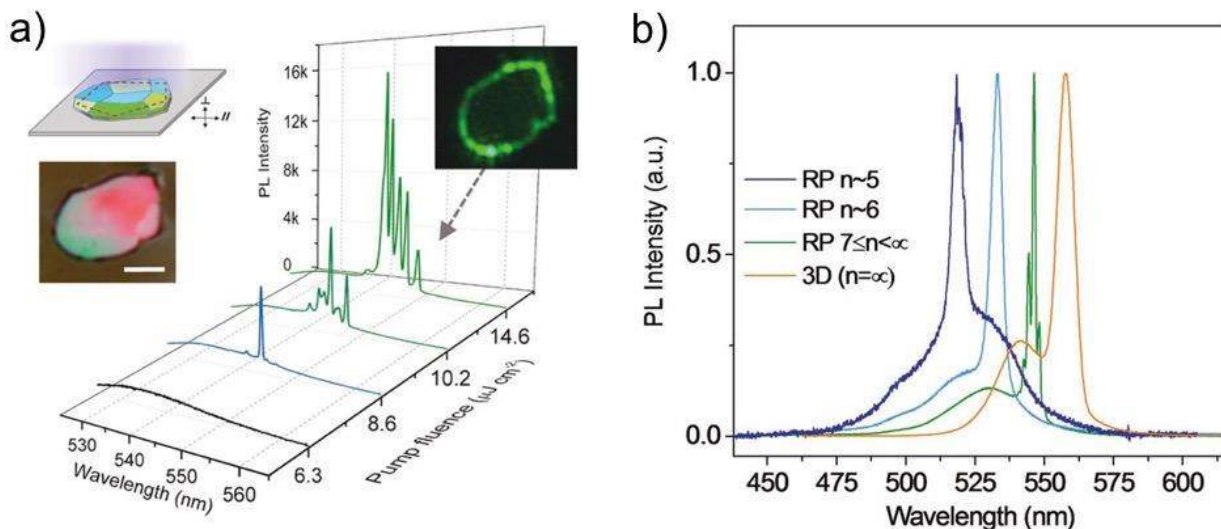


Figure 26. a) Lasing from a single low-dimensional perovskite microplate. Pump-fluence-dependent PL spectra of a single microplate. Left inset: Optical image, scale bar: 5 μm , and schematic illustration of lasing measurements of microplate on a substrate pumped by a 400 nm laser excitation (≈ 150 fs, 1 kHz). b) Normalized lasing spectra from 3D perovskite film to quasi-2D perovskite microplates²⁴⁰. Reprinted with permission from ref 195. Copyright 2018, Wiley-VCH.

5.2 Laser Cavity Structures in Perovskite Lasers

In semiconducting nanowires, waveguiding is provided along the axial direction, and the two end facets form a Fabry–Perot cavity. The growth of high-quality single-crystal nanowires from low-temperature solution-processing of MAPbX_3 perovskites was reported by Zhu and co-workers²⁴¹. The perovskite nanowires exhibited low lasing thresholds (200 nJ/cm^2); high quality factors ($Q \sim 3,600$); near-unity quantum yield; and wavelength tunability from the near-infrared to the visible wavelengths (Figure 27).

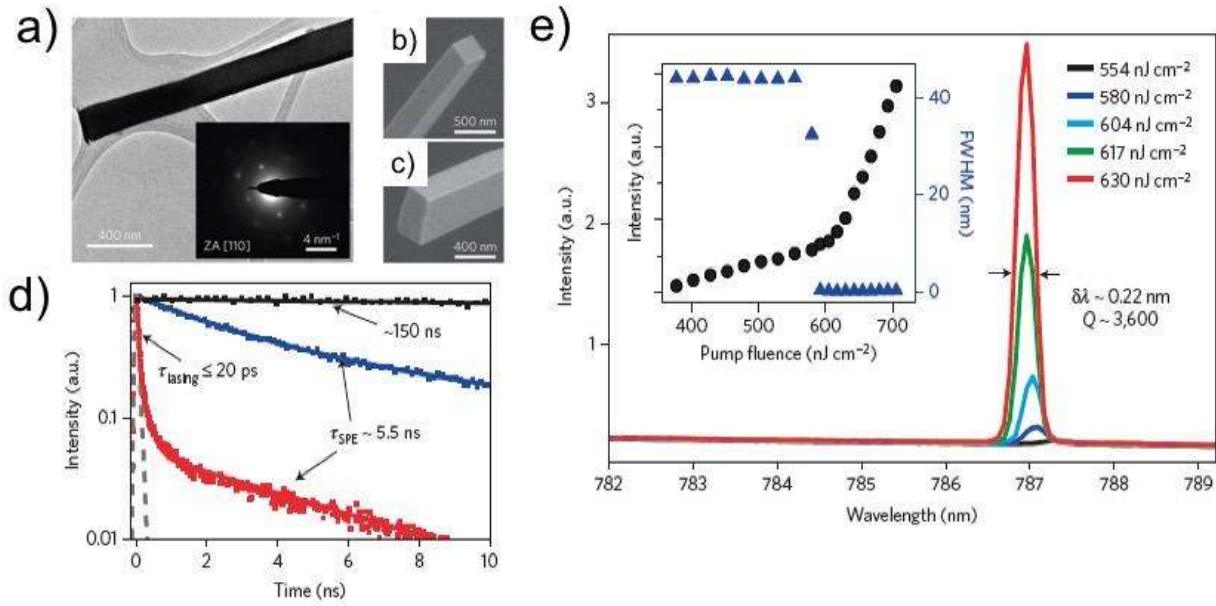


Figure 27. a) TEM images and selected-area electron diffraction patterns along the [110] zone axis (ZA). b,c) SEM images of perovskite nanowires. d) Transient decay kinetics of perovskite nanowires with different excitation fluence ($P \sim 0.85P_{\text{Th}}$, blue; $P \sim 1.1P_{\text{Th}}$, red). e) Emission spectra of perovskite nanowires near the lasing threshold²⁴¹. Reprinted with permission from ref 206. Copyright 2015, Nature Publishing Group.

Perovskite nanoplatelets were grown on mica substrates and formed whispering-gallery-mode (WGM) cavities as a result of the growth procedure²⁴². Individual perovskite nanoplatelets were photoexcited using a femtosecond-pulsed laser, and a lasing threshold of $37 \mu\text{J cm}^{-2}$ was achieved in MAPbI₃ nanoplatelets. Solution growth of MAPbBr₃ perovskite micro-disks – also a means to WGM microresonators – exhibited a quality factor of ~ 430 ²⁴³. Single-mode lasing at 558 nm was achieved in a $2 \times 2 \times 0.6 \mu\text{m}^3$ square micro-disk and exhibited a threshold of $3.6 \pm 0.5 \mu\text{J cm}^{-2}$. WGM lasers from planar perovskite nanoplatelets exhibit tunable optical modes and impressive optical gain, and offer a pathway to integration with Si technologies.

In distributed feedback (DFB) cavity structures, optical feedback is provided via Bragg scattering from an interference grating built either directly into the active medium, or in the vicinity of the resonator through periodic alternation of the refractive index. Jia *et.al.*, reported a metal-clad, second order DFB perovskite laser with a threshold of 5 kW/cm² for durations ≤ 25 ns. The work demonstrated that the substrate can be used to dissipate heat and offered thus a step in the direction of future electrically-driven architectures²⁴⁴. Saliba *et al*, reported perovskite DFB cavities made by nanoimprinting a corrugated structure onto a polymer template, after which they then introduced a conformal perovskite layer²⁴⁵. Significant narrowing of the linewidth of the ASE peak was observed with increased excitation fluence, and the wavelength redshifted as the grating periodicity of the DFB cavity increased. The fluence threshold diminished from 2.1 to 0.3 $\mu\text{J cm}^{-2}$ as the grating period decreased from 420 to 400 nm.

A new hybrid perovskite vertical cavity surface-emitting laser (VCSEL) was microfabricated based on a uniform perovskite thin (≈ 300 nm) film placed between two high-reflectivity ($\approx 99.5\%$) distributed Bragg reflectors (DBRs)²⁴⁶. This work leveraged gallium nitride semiconductor process innovations wherein a nanoporous-GaN (NP-GaN) provides the low-index layers in a NP-GaN/GaN (electrically conducting) multilayer stack. The perovskite VCSEL device enabled the study of gain dynamics on excitation timescales that are much longer than typically reported in femtosecond experiments in the perovskite literature. VCSEL lasing output as a function of pumping fluence indicated a lasing threshold of 7.6 $\mu\text{J cm}^{-2}$.

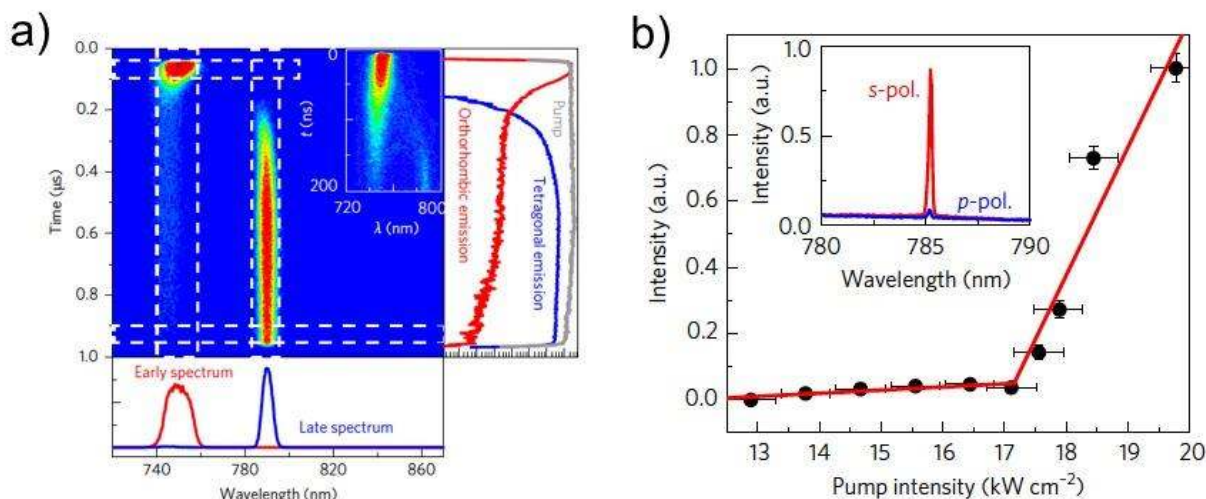


Figure 28. a) Streak camera image of emission from the MAPbI₃ film under the pump intensity 37.5 kWcm⁻² with InGaN diode laser with instantaneous intensity. The substrate temperature is lowered to $T = 106$ K. In this case, ASE from the orthorhombic phase of MAPbI₃ is observed at early times but evolves within ~ 200 ns. b) Input–output characteristic of the laser under continuous excitation by a $\lambda = 445$ nm InGaN pump diode at a substrate temperature of 102 K, demonstrating a clear threshold at $IP \approx 17$ kW/cm²²⁴⁷. Reprinted with permission from ref 212. Copyright 2017, Nature Publishing Group.

Continuous-wave (c.w.) operation of a perovskite methylammonium lead iodide (MAPbI₃)²⁴⁷ laser was recently reported (Figure 28). Under constant blue optical photoexcitation, devices emitted near-infrared (785 nm wavelength) laser light over the course of an hour when operated at 100 K. To achieve c.w. lasing, the authors sought a strategy to generate exciton/charge-trapping sites in the material. They took advantage of the phase transition in MAPbI₃: when the temperature is decreased to 160 K, the crystal structure of MAPbI₃ changes from tetragonal phase to the orthorhombic phase. A distributed feedback laser fabricated with MAPbI₃ was operated at 100 K, hence in orthorhombic phase. With a high excitation power (> 17 kW cm⁻²), the tetragonal phase

can transform to the orthorhombic lattice within a few 100 ns, due to local heating, and this provides a local heterostructure inside the perovskite film.

6 Conclusions and Outlook

The efficiencies of perovskite solar cells have advanced from 3.8 to a certified 23.3% in less than a decade of concerted worldwide effort. The materials rely upon facile low-temperature processing. Their structural flexibility and excellent optoelectronic properties have yielded efficient LEDs as well as lasers.

In optical sources, one central theme in perovskite light emission has been the move from the bulk (3D) materials widely used in solar cells towards instead the application of reduced-dimensional structures. Taken together with judicious compositional engineering, this has advanced perovskites across a wide range of emission wavelengths to near-unity PLQY. The same defect-tolerance that serves these materials so well in photovoltaics is a major factor enabling their bright PL. It will be important to improve further the photostability of reduced-dimensional perovskites. The passivation of grain boundaries is a particularly important priority.

Among these reduced-dimensional perovskite emitters, colloiddally-synthesized nanometer-scale nanocrystals have shown excellent quantum yield, and combine with other classes of solution-processed materials, such as polymers and small molecules, to enhanced optical and electronic functionalities. It will be essential to apply high-PLQY nanocrystals in displays, and generating new Pb-free materials options that exhibit excellent emission properties is a high priority as a result. Possibilities based upon Sn, Ge, Cu, Bi, and Sb have been explored, but lead-free perovskites today perform well below Pb-based device levels. Accelerated computational-experimental approaches could potentially contribute to addressing this important challenge.

Given the soft nature of the hybrid perovskite materials, their stability against moisture, heat, oxygen and electric field will continue to be an area of intense activity. Here the versatile chemistry of hybrid organic-inorganic perovskites will be leveraged on the path to further progress. Recent advances on this front are encouraging, including operating stability of 1,000 hours under 1 sun illumination. Integrated encapsulation strategies have increased stability against external humidity and heat. Compared with solar cells, though, LEDs still rely on charge injection rather than extraction; and also see higher fields in light of the > 3 V often used to drive devices. It will therefore be of urgent importance to enhance further the operational stability of perovskite LEDs.

Progress in perovskite LEDs has been uneven as a function of emission wavelength: the EQE in the green rapidly exceeded 20%^{43,135,159,162}; but in the blue emission resides in the 3% and below range¹⁷⁹. Recent reports of blue luminescence quantum yields of 80%²⁴⁸ are certainly encouraging, but such materials need to be married with enhanced carrier transport and suitable interlayer band alignment to translate into high device performance. Highly emissive, stable, and conductive blue emitting perovskite materials remain a frontier area of great applied importance and fundamental interest.

On lasing, room-temperature CW performance is a next frontier. Perovskite single crystals are promising candidates for CW lasing and their slower Auger recombination and lower thresholds offer encouragement on this path. Electrically-driven lasing is a next challenge: population inversion is required from a high-quality gain medium exhibiting slow Auger recombination. Electrical excitation demands high charge carrier mobilities as well as improved thermal stability, a larger gain and sharp absorption band tails. Perovskites have shown encouraging properties on many of these fronts, except that thermal stability and carrier mobility will likely need further improvement.

Biographies

Li Na Quan received her Ph.D. from Ewha Womans University, Korea in 2016 under the supervision of Prof. Dong Ha Kim. From 2014 to 2017, she worked at the University of Toronto with Prof. Edward. H. Sargent as a graduate student and postdoctoral researcher. Since 2018, she has worked with Prof. Peidong Yang at the University of California, Berkeley, as a postdoctoral fellow. Her research focuses on low-dimensional perovskites for light harvesting and optical source applications and photophysical studies.

Barry P. Rand earned a BE in electrical engineering from The Cooper Union in 2001. Then he received MA and PhD degrees in electrical engineering from Princeton University, in 2003 and 2007, respectively. From 2007 to 2013, he was at IMEC in Leuven, Belgium, ultimately as a principal scientist. Since 2013, he is in the Department of Electrical Engineering and Andlinger Center for Energy and the Environment at Princeton University, currently as an Associate Professor. He has authored more than 115 refereed journal publications, has 20 issued US patents, and has received the 3M Nontenured Faculty Award (2014), DuPont Young Professor Award (2015), DARPA Young Faculty Award (2015), and ONR Young Investigator Program Award (2016).

Tae-Woo Lee is an associate professor in the department of materials science and engineering at Seoul National University, Korea. He received his Ph.D in Chemical Engineering from KAIST, Korea in 2002. He joined Bell Laboratories, USA as a postdoctoral researcher in 2002 and worked at Samsung Advanced Institute of Technology as a member of research staff (2003-2008). He was an assistant and associate professor in the department of materials science and engineering at Pohang University of Science and Technology (POSTECH), Korea until August 2016. His research focuses on organic, organic-inorganic hybrid perovskite and carbon materials, and their

applications to flexible electronics, printed electronics, displays, solid-state lightings, solar energy conversion devices, and bio-inspired neuromorphic devices.

Subodh G. Mhaisalkar is the Tan Chin Tuan Centennial Professor in the School of Materials Science & Engineering at the Nanyang Technological University (NTU), Singapore. He is also the Executive Director of the Energy Research Institute at NTU (ERI@N), a pan-University multidisciplinary research institute for innovative energy solutions. Prior to joining NTU in 2001, he had over 10 years of research and engineering experience in the microelectronics industry. He received his Bachelors' degree from IIT-Bombay, India and his MS/Ph.D. degrees from The Ohio State University, USA.

Richard H. Friend is the Cavendish Professor of Physics at the University of Cambridge. His research interests relate to the optoelectronic properties of organic materials.

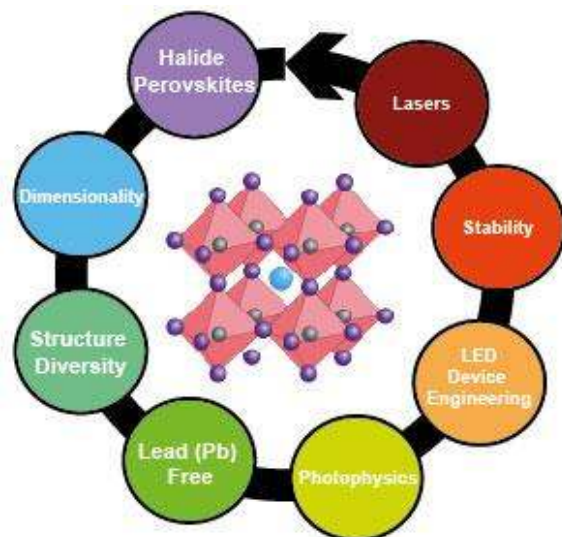
Edward H. Sargent is University Professor in Electrical and Computer Engineering at the University of Toronto. He holds the Canada Research Chair in Nanotechnology and also serves as Vice President - International for the University. He was founder and CTO of InVisage Technologies Inc. of Menlo Park.

Acknowledgements

B. P. R. acknowledges support from the US Office of Naval Research Young Investigator Program (Grant Award No. N00014-17-1-2005). R.H.F acknowledge support from the Engineering and Physical Sciences Research Council (EPSRC). S.G.M. acknowledges support from the US Office of Naval Research (ONRGNICOP-N62909-17-1-2155) and from the Singapore National Research (Program NRF-CRP14-2014-03). T.-W. L. acknowledges support from the National Research Foundation of Korea (NRF) grant funded by the Korea government (Ministry of Science, ICT &

Future Planning) (NRF-2016R1A3B1908431). E. H. S. acknowledges support from the US Office of Naval Research (Grant Award No.: N00014-17-1-2524).

TOC:



References

- (1) Kojima, A.; Teshima, K.; Shirai, Y.; Miyasaka, T. Organometal Halide Perovskites as Visible-Light Sensitizers for Photovoltaic Cells. *J. Am. Chem. Soc.* **2009**, *131*, 6050-6051.
- (2) Kim, H. S.; Lee, C. R.; Im, J. H.; Lee, K. B.; Moehl, T.; Marchioro, A.; Moon, S. J.; Humphry-Baker, R.; Yum, J. H.; Moser, J. E. et al. Lead Iodide Perovskite Sensitized All-Solid-State Submicron Thin Film Mesoscopic Solar Cell with Efficiency Exceeding 9%. *Sci. Rep.* **2012**, *2*, 591.
- (3) Lee, M. M.; Teuscher, J.; Miyasaka, T.; Murakami, T. N.; Snaith, H. J. Efficient Hybrid Solar Cells Based on Meso-Superstructured Organometal Halide Perovskites. *Science* **2012**, *338*, 643-647.
- (4) Abrusci, A.; Stranks, S. D.; Docampo, P.; Yip, H. L.; Jen, A. K.; Snaith, H. J. High-Performance Perovskite-Polymer Hybrid Solar Cells Via Electronic Coupling with Fullerene Monolayers. *Nano Lett.* **2013**, *13*, 3124-3128.
- (5) Burschka, J.; Pellet, N.; Moon, S. J.; Humphry-Baker, R.; Gao, P.; Nazeeruddin, M. K.; Gratzel, M. Sequential Deposition as a Route to High-Performance Perovskite-Sensitized Solar Cells. *Nature* **2013**, *499*, 316-319.
- (6) Liu, M.; Johnston, M. B.; Snaith, H. J. Efficient Planar Heterojunction Perovskite Solar Cells by Vapour Deposition. *Nature* **2013**, *501*, 395-398.
- (7) <https://www.nrel.gov/pv/cell-efficiency.html>. Best Research Cell Efficiencies. National Renewable Energy Laboratory. (accessed April 3, 2019).
- (8) Correa-Baena, J.-P.; Saliba, M.; Buonassisi, T.; Grätzel, M.; Abate, A.; Tress, W.; Hagfeldt, A. Promises and Challenges of Perovskite Solar Cells. *Science* **2017**, *358*, 739-744.

- (9) Stranks, S. D.; Eperon, G. E.; Grancini, G.; Menelaou, C.; Alcocer, M. J. P.; Leijtens, T.; Herz, L. M.; Petrozza, A.; Snaith, H. J. Electron-Hole Diffusion Lengths Exceeding 1 Micrometer in an Organometal Trihalide Perovskite Absorber. *Science* **2013**, *342*, 341-344.
- (10) Sutherland, B. R.; Sargent, E. H. Perovskite Photonic Sources. *Nat. Photonics* **2016**, *10*, 295-302.
- (11) Era, M.; Morimoto, S.; Tsutsui, T.; Saito, S. Organic - Inorganic Heterostructure Electroluminescent Device Using a Layered Perovskite Semiconductor (C₆H₅C₂H₄NH₃)₂PbI₄. *Appl. Phys. Lett.* **1994**, *65*, 676-678.
- (12) Tan, Z. K.; Moghaddam, R. S.; Lai, M. L.; Docampo, P.; Higler, R.; Deschler, F.; Price, M.; Sadhanala, A.; Pazos, L. M.; Credgington, D. et al. Bright Light-Emitting Diodes Based on Organometal Halide Perovskite. *Nat. Nanotechnol.* **2014**, *9*, 687-692.
- (13) Cho, H.; Jeong, S. H.; Park, M. H.; Kim, Y. H.; Wolf, C.; Lee, C. L.; Heo, J. H.; Sadhanala, A.; Myoung, N.; Yoo, S. et al. Overcoming the Electroluminescence Efficiency Limitations of Perovskite Light-Emitting Diodes. *Science* **2015**, *350*, 1222-1225.
- (14) Saliba, M.; Matsui, T.; Domanski, K.; Seo, J.-Y.; Ummadisingu, A.; Zakeeruddin, S. M.; Correa-Baena, J.-P.; Tress, W. R.; Abate, A.; Hagfeldt, A. Incorporation of Rubidium Cations into Perovskite Solar Cells Improves Photovoltaic Performance. *Science* **2016**, *354*, 206-209.
- (15) Ptak, M.; Mączka, M.; Gągor, A.; Sieradzki, A.; Stroppa, A.; Di Sante, D.; Perez-Mato, J. M.; Macalik, L. Experimental and Theoretical Studies of Structural Phase Transition in a Novel Polar Perovskite-Like [C₂H₅NH₃][Na_{0.5}Fe_{0.5}(Hcoo)₃] Formate. *Dalton transactions* **2016**, *45*, 2574-2583.
- (16) Frost, J. M.; Butler, K. T.; Brivio, F.; Hendon, C. H.; Van Schilfgaarde, M.; Walsh, A. Atomistic Origins of High-Performance in Hybrid Halide Perovskite Solar Cells. *Nano Lett.* **2014**, *14*, 2584-2590.
- (17) Anusca, I.; Balčiūnas, S.; Gemeiner, P.; Svirskas, Š.; Sanlialp, M.; Lackner, G.; Fettkenhauer, C.; Belovickis, J.; Samulionis, V.; Ivanov, M. Dielectric Response: Answer to Many Questions in the Methylammonium Lead Halide Solar Cell Absorbers. *Adv. Energy Mater.* **2017**, *7*, 1700600.
- (18) Tan, H.; Che, F.; Wei, M.; Zhao, Y.; Saidaminov, M. I.; Todorović, P.; Broberg, D.; Walters, G.; Tan, F.; Zhuang, T. Dipolar Cations Confer Defect Tolerance in Wide-Bandgap Metal Halide Perovskites. *Nat. commun.* **2018**, *9*, 3100-3108.
- (19) Družbicki, K.; Pinna, R. S.; Rudić, S.; Jura, M.; Gorini, G.; Fernandez-Alonso, F. Unexpected Cation Dynamics in the Low-Temperature Phase of Methylammonium Lead Iodide: The Need for Improved Models. *J. Phys. Chem. Lett.* **2016**, *7*, 4701-4709.
- (20) Brivio, F.; Frost, J. M.; Skelton, J. M.; Jackson, A. J.; Weber, O. J.; Weller, M. T.; Goni, A. R.; Leguy, A. M.; Barnes, P. R.; Walsh, A. Lattice Dynamics and Vibrational Spectra of the Orthorhombic, Tetragonal, and Cubic Phases of Methylammonium Lead Iodide. *Phys. Rev. B* **2015**, *92*, 144308.
- (21) Pérez-Osorio, M. A.; Milot, R. L.; Filip, M. R.; Patel, J. B.; Herz, L. M.; Johnston, M. B.; Giustino, F. Vibrational Properties of the Organic-Inorganic Halide Perovskite CH₃NH₃PbI₃ from Theory and Experiment: Factor Group Analysis, First-Principles Calculations, and Low-Temperature Infrared Spectra. *J. Phys. Chem. C* **2015**, *119*, 25703-25718.

- (22) Mattoni, A.; Filippetti, A.; Saba, M.; Caddeo, C.; Delugas, P. Temperature Evolution of Methylammonium Trihalide Vibrations at the Atomic Scale. *J. Phys. Chem. Lett.* **2016**, *7*, 529-535.
- (23) Leguy, A. M.; Goñi, A. R.; Frost, J. M.; Skelton, J.; Brivio, F.; Rodríguez-Martínez, X.; Weber, O. J.; Pallipurath, A.; Alonso, M. I.; Campoy-Quiles, M. Dynamic Disorder, Phonon Lifetimes, and the Assignment of Modes to the Vibrational Spectra of Methylammonium Lead Halide Perovskites. *Phys. Chem. Chem. Phys.* **2016**, *18*, 27051-27066.
- (24) Li, B.; Kawakita, Y.; Liu, Y.; Wang, M.; Matsuura, M.; Shibata, K.; Ohira-Kawamura, S.; Yamada, T.; Lin, S.; Nakajima, K. Polar Rotor Scattering as Atomic-Level Origin of Low Mobility and Thermal Conductivity of Perovskite $\text{CH}_3\text{NH}_3\text{PbI}_3$. *Nat. commun.* **2017**, *8*, 16086.
- (25) Lotsch, B. V. New Light on an Old Story: Perovskites Go Solar. *Angew. Chem. Int. Ed.* **2014**, *53*, 635-637.
- (26) Quan, L. N.; Yuan, M.; Comin, R.; Voznyy, O.; Beauregard, E. M.; Hoogland, S.; Buin, A.; Kirmani, A. R.; Zhao, K.; Amassian, A. et al. Ligand-Stabilized Reduced-Dimensionality Perovskites. *J. Am. Chem. Soc.* **2016**, *138*, 2649-2655.
- (27) De Wolf, S.; Holovsky, J.; Moon, S.-J.; Löper, P.; Niesen, B.; Ledinsky, M.; Haug, F.-J.; Yum, J.-H.; Ballif, C. Organometallic Halide Perovskites: Sharp Optical Absorption Edge and Its Relation to Photovoltaic Performance. *J. Phys. Chem. Lett.* **2014**, *5*, 1035-1039.
- (28) Shi, D.; Adinolfi, V.; Comin, R.; Yuan, M.; Alarousu, E.; Buin, A.; Chen, Y.; Hoogland, S.; Rothenberger, A.; Katsiev, K. et al. Low Trap-State Density and Long Carrier Diffusion in Organolead Trihalide Perovskite Single Crystals. *Science* **2015**, *347*, 519-522.
- (29) Senanayak, S. P.; Yang, B.; Thomas, T. H.; Giesbrecht, N.; Huang, W.; Gann, E.; Nair, B.; Goedel, K.; Guha, S.; Moya, X. Understanding Charge Transport in Lead Iodide Perovskite Thin-Film Field-Effect Transistors. *Science Advances* **2017**, *3*, e1601935.
- (30) Philippe, B.; Jacobsson, T. J.; Correa-Baena, J.-P.; Jena, N. K.; Banerjee, A.; Chakraborty, S.; Cappel, U. B.; Ahuja, R.; Hagfeldt, A.; Odelius, M. Valence Level Character in a Mixed Perovskite Material and Determination of the Valence Band Maximum from Photoelectron Spectroscopy: Variation with Photon Energy. *J. Phys. Chem. C* **2017**, *121*, 26655-26666.
- (31) Saliba, M.; Matsui, T.; Seo, J. Y.; Domanski, K.; Correa-Baena, J. P.; Nazeeruddin, M. K.; Zakeeruddin, S. M.; Tress, W.; Abate, A.; Hagfeldt, A. et al. Cesium-Containing Triple Cation Perovskite Solar Cells: Improved Stability, Reproducibility and High Efficiency. *Energy Environ. Sci.* **2016**, *9*, 1989-1997.
- (32) Abdi-Jalebi, M.; Andaji-Garmaroudi, Z.; Cacovich, S.; Stavrakas, C.; Philippe, B.; Richter, J. M.; Alsari, M.; Booker, E. P.; Hutter, E. M.; Pearson, A. J. Maximizing and Stabilizing Luminescence from Halide Perovskites with Potassium Passivation. *Nature* **2018**, *555*, 497.
- (33) Abdi-Jalebi, M.; Andaji-Garmaroudi, Z.; Cacovich, S.; Stavrakas, C.; Philippe, B.; Richter, J. M.; Alsari, M.; Booker, E. P.; Hutter, E. M.; Pearson, A. J. Maximizing and Stabilizing Luminescence from Halide Perovskites with Potassium Passivation. *Nature* **2018**, *555*, 497-501.

- (34) Xiao, Z.; Zhao, L.; Tran, N. L.; Lin, Y. L.; Silver, S. H.; Kerner, R. A.; Yao, N.; Kahn, A.; Scholes, G. D.; Rand, B. P. Mixed-Halide Perovskites with Stabilized Bandgaps. *Nano Lett.* **2017**, *17*, 6863-6869.
- (35) Li, N.; Zhu, Z.; Li, J.; Jen, A. K. Y.; Wang, L. Inorganic CsPbBr₃-XSnBr₂ for Efficient Wide - Bandgap Perovskite Solar Cells. *Adv. Energy Mater.* **2018**, 1800525.
- (36) Vorpahl, S. M.; Stranks, S. D.; Nagaoka, H.; Eperon, G. E.; Ziffer, M. E.; Snaith, H. J.; Ginger, D. S. Impact of Microstructure on Local Carrier Lifetime in Perovskite Solar Cells. *Science* **2015**, 683-686.
- (37) Mitzi, D. B. Synthesis, Structure, and Properties of Organic - Inorganic Perovskites and Related Materials. *Prog. Inorg. Chem.* **1999**, 1-121.
- (38) Mitzi, D. B.; Feild, C.; Harrison, W.; Guloy, A. Conducting Tin Halides with a Layered Organic-Based Perovskite Structure. *Nature* **1994**, *369*, 467-469.
- (39) Hong, X.; Ishihara, T.; Nurmikko, A. Photoconductivity and Electroluminescence in Lead Iodide Based Natural Quantum Well Structures. *Solid State Commun.* **1992**, *84*, 657-661.
- (40) Chondroudis, K.; Mitzi, D. B. Electroluminescence from an Organic- Inorganic Perovskite Incorporating a Quaterthiophene Dye within Lead Halide Perovskite Layers. *Chem. Mater.* **1999**, *11*, 3028-3030.
- (41) Yuan, M.; Quan, L. N.; Comin, R.; Walters, G.; Sabatini, R.; Voznyy, O.; Hoogland, S.; Zhao, Y.; Beauregard, E. M.; Kanjanaboos, P. et al. Perovskite Energy Funnels for Efficient Light-Emitting Diodes. *Nat. Nanotechnol.* **2016**, *11*, 872-877.
- (42) Xiao, Z.; Kerner, R. A.; Zhao, L.; Tran, N. L.; Lee, K. M.; Koh, T.-W.; Scholes, G. D.; Rand, B. P. Efficient Perovskite Light-Emitting Diodes Featuring Nanometre-Sized Crystallites. *Nat. Photonics* **2017**, *11*, 108-115.
- (43) Wang, N.; Cheng, L.; Ge, R.; Zhang, S.; Miao, Y.; Zou, W.; Yi, C.; Sun, Y.; Cao, Y.; Yang, R. et al. Perovskite Light-Emitting Diodes Based on Solution-Processed Self-Organized Multiple Quantum Wells. *Nat. Photonics* **2016**, *10*, 699-704.
- (44) Quan, L. N.; Zhao, Y.; Garcia de Arquer, F. P.; Sabatini, R.; Walters, G.; Voznyy, O.; Comin, R.; Li, Y.; Fan, J. Z.; Tan, H. et al. Tailoring the Energy Landscape in Quasi-2d Halide Perovskites Enables Efficient Green-Light Emission. *Nano Lett.* **2017**, *17*, 3701-3709.
- (45) Byun, J.; Cho, H.; Wolf, C.; Jang, M.; Sadhanala, A.; Friend, R. H.; Yang, H.; Lee, T. W. Efficient Visible Quasi - 2d Perovskite Light - Emitting Diodes. *Adv. Mater.* **2016**, *28*, 7515-7520.
- (46) Tsai, H.; Nie, W.; Blancon, J. C.; Stoumpos, C. C.; Asadpour, R.; Harutyunyan, B.; Neukirch, A. J.; Verduzco, R.; Crochet, J. J.; Tretiak, S. et al. High-Efficiency Two-Dimensional Ruddlesden-Popper Perovskite Solar Cells. *Nature* **2016**, *536*, 312-316.
- (47) Cao, D. H.; Stoumpos, C. C.; Farha, O. K.; Hupp, J. T.; Kanatzidis, M. G. 2d Homologous Perovskites as Light-Absorbing Materials for Solar Cell Applications. *J. Am. Chem. Soc.* **2015**, *137*, 7843-7850.
- (48) Mitzi, D.; Wang, S.; Feild, C.; Chess, C.; Guloy, A. Conducting Layered Organic-Inorganic Halides Containing < 110 >-Oriented Perovskite Sheets. *Science* **1995**, *267*, 1473-1476.
- (49) Li, Y.; Zheng, G.; Lin, C.; Lin, J. Synthesis, Structure and Optical Properties of Different Dimensional Organic-Inorganic Perovskites. *Solid State Sciences* **2007**, *9*, 855-861.

- (50) Sun, S.; Tominaka, S.; Lee, J.-H.; Xie, F.; Bristowe, P. D.; Cheetham, A. K. Synthesis, Crystal Structure, and Properties of a Perovskite-Related Bismuth Phase, $(\text{NH}_4)_3\text{Bi}_2\text{I}_9$. *Applied Physics Letter Materials* **2016**, *4*, 031101.
- (51) Zaleski, J.; Pietraszko, A. Structure at 200 and 298 K and X - Ray Investigations of the Phase Transition at 242 K of $[\text{NH}_2(\text{CH}_3)_2]_3\text{Sb}_2\text{Cl}_9$ (Dmaca). *Acta Crystallographica Section B* **1996**, *52*, 287-295.
- (52) Kallel, A.; Bats, J. Tris (Trimethylammonium) Nonachlorodiantimonate $(\text{NH}_4)_3[\text{Sb}_2\text{Cl}_9]$. *Acta Crystallographica Section C* **1985**, *41*, 1022-1024.
- (53) Dohner, E. R.; Hoke, E. T.; Karunadasa, H. I. Self-Assembly of Broadband White-Light Emitters. *J. Am. Chem. Soc.* **2014**, *136*, 1718-1721.
- (54) Dohner, E. R.; Jaffe, A.; Bradshaw, L. R.; Karunadasa, H. I. Intrinsic White-Light Emission from Layered Hybrid Perovskites. *J. Am. Chem. Soc.* **2014**, *136*, 13154-13157.
- (55) Hu, T.; Smith, M. D.; Dohner, E. R.; Sher, M.-J.; Wu, X.; Trinh, M. T.; Fisher, A.; Corbett, J.; Zhu, X.-Y.; Karunadasa, H. I. Mechanism for Broadband White-Light Emission from Two-Dimensional (110) Hybrid Perovskites. *J. Phys. Chem. Lett.* **2016**, *7*, 2258-2263.
- (56) Mao, L.; Wu, Y.; Stoumpos, C. C.; Wasielewski, M. R.; Kanatzidis, M. G. White-Light Emission and Structural Distortion in New Corrugated Two-Dimensional Lead Bromide Perovskites. *Journal of American Chemical Society* **2017**, *139*, 5210-5215.
- (57) Mao, L.; Wu, Y.; Stoumpos, C. C.; Wasielewski, M. R.; Kanatzidis, M. G. White-Light Emission and Structural Distortion in New Corrugated Two-Dimensional Lead Bromide Perovskites. *J. Am. Chem. Soc.* **2017**, *139*, 5210-5215.
- (58) Nikl, M.; Mihokova, E.; Nitsch, K.; Somma, F.; Giampaolo, C.; Pazzi, G.; Fabeni, P.; Zazubovich, S. Photoluminescence of Cs_4PbBr_6 Crystals and Thin Films. *Chem. Phys. Lett.* **1999**, *306*, 280-284.
- (59) Palazon, F.; Almeida, G.; Akkerman, Q. A.; De Trizio, L.; Dang, Z.; Prato, M.; Manna, L. Changing the Dimensionality of Cesium Lead Bromide Nanocrystals by Reversible Postsynthesis Transformations with Amines. *Chem. Mater.* **2017**, *29*, 4167-4171.
- (60) Wu, L.; Hu, H.; Xu, Y.; Jiang, S.; Chen, M.; Zhong, Q.; Yang, D.; Liu, Q.; Zhao, Y.; Sun, B. From Nonluminescent Cs_4PbX_6 (X= Cl, Br, I) Nanocrystals to Highly Luminescent CsPbX_3 Nanocrystals: Water-Triggered Transformation through a CsX-Stripping Mechanism. *Nano Lett.* **2017**, *17*, 5799-5804.
- (61) Palazon, F.; Urso, C.; De Trizio, L.; Akkerman, Q.; Marras, S.; Locardi, F.; Nelli, I.; Ferretti, M.; Prato, M.; Manna, L. Postsynthesis Transformation of Insulating Cs_4PbBr_6 Nanocrystals into Bright Perovskite CsPbBr_3 through Physical and Chemical Extraction of CsBr. *ACS Energy Lett.* **2017**, *2*, 2445-2448.
- (62) Liu, Z.; Bekenstein, Y.; Ye, X.; Nguyen, S. C.; Swabeck, J.; Zhang, D.; Lee, S.-T.; Yang, P.; Ma, W.; Alivisatos, A. P. Ligand Mediated Transformation of Cesium Lead Bromide Perovskite Nanocrystals to Lead Depleted Cs_4PbBr_6 Nanocrystals. *J. Am. Chem. Soc.* **2017**, *139*, 5309-5312.
- (63) Quan, L. N.; Quintero - Bermudez, R.; Voznyy, O.; Walters, G.; Jain, A.; Fan, J. Z.; Zheng, X.; Yang, Z.; Sargent, E. H. Highly Emissive Green Perovskite Nanocrystals in a Solid State Crystalline Matrix. *Adv. Mater.* **2017**, *29*, 1605945.
- (64) Chen, X.; Zhang, F.; Ge, Y.; Shi, L.; Huang, S.; Tang, J.; Lv, Z.; Zhang, L.; Zou, B.; Zhong, H. Centimeter - Sized Cs_4PbBr_6 Crystals with Embedded CsPbBr_3 Nanocrystals

- Showing Superior Photoluminescence: Nonstoichiometry Induced Transformation and Light - Emitting Applications. *Adv. Funct. Mater.* **2018**, *28*, 1706567.
- (65) Savory, C. N.; Walsh, A.; Scanlon, D. O. Can Pb-Free Halide Double Perovskites Support High-Efficiency Solar Cells? *ACS Energy Lett.* **2016**, *1*, 949-955.
- (66) Xiao, Z.; Zhou, Y.; Hosono, H.; Kamiya, T. Intrinsic Defects in a Photovoltaic Perovskite Variant Cs₂SnI₆. *Phys. Chem. Chem. Phys.* **2015**, *17*, 18900-18903.
- (67) Jain, A.; Voznyy, O.; Sargent, E. H. High-Throughput Screening of Lead-Free Perovskite-Like Materials for Optoelectronic Applications. *J. Phys. Chem. C* **2017**, *121*, 7183-7187.
- (68) Slavney, A. H.; Hu, T.; Lindenberg, A. M.; Karunadasa, H. I. A Bismuth-Halide Double Perovskite with Long Carrier Recombination Lifetime for Photovoltaic Applications. *J. Am. Chem. Soc.* **2016**, *138*, 2138-2141.
- (69) Shi, Z.; Guo, J.; Chen, Y.; Li, Q.; Pan, Y.; Zhang, H.; Xia, Y.; Huang, W. Lead - Free Organic-Inorganic Hybrid Perovskites for Photovoltaic Applications: Recent Advances and Perspectives. *Adv. Mater.* **2017**, *29*, 1605005.
- (70) Lee, S. J.; Shin, S. S.; Kim, Y. C.; Kim, D.; Ahn, T. K.; Noh, J. H.; Seo, J.; Seok, S. I. Fabrication of Efficient Formamidinium Tin Iodide Perovskite Solar Cells through SnF₂-Pyrazine Complex. *J. Am. Chem. Soc.* **2016**, *138*, 3974-3977.
- (71) Gupta, S.; Cahen, D.; Hodes, G. How SnF₂ Impacts the Material Properties of Lead-Free Tin Perovskites. *J. Phys. Chem. C* **2018**, *122*, 13926-13936.
- (72) Yuan, F.; Xi, J.; Dong, H.; Xi, K.; Zhang, W.; Ran, C.; Jiao, B.; Hou, X.; Jen, A. K. Y.; Wu, Z. All - Inorganic Hetero - Structured Cesium Tin Halide Perovskite Light - Emitting Diodes with Current Density over 900 a Cm⁻² and Its Amplified Spontaneous Emission Behaviors. *physica status solidi (RRL)-Rapid Research Letters* **2018**, *12*, 1800090.
- (73) Lanzetta, L.; Marin-Beloqui, J. M.; Sanchez-Molina, I.; Ding, D.; Haque, S. A. Two-Dimensional Organic Tin Halide Perovskites with Tunable Visible Emission and Their Use in Light-Emitting Devices. *ACS Energy Lett.* **2017**, *2*, 1662-1668.
- (74) Stoumpos, C. C.; Frazer, L.; Clark, D. J.; Kim, Y. S.; Rhim, S. H.; Freeman, A. J.; Ketterson, J. B.; Jang, J. I.; Kanatzidis, M. G. Hybrid Germanium Iodide Perovskite Semiconductors: Active Lone Pairs, Structural Distortions, Direct and Indirect Energy Gaps, and Strong Nonlinear Optical Properties. *J. Am. Chem. Soc.* **2015**, *137*, 6804-6819.
- (75) Filip, M. R.; Hillman, S.; Haghighirad, A. A.; Snaith, H. J.; Giustino, F. Band Gaps of the Lead-Free Halide Double Perovskites Cs₂BiAgCl₆ and Cs₂BiAgBr₆ from Theory and Experiment. *J. Phys. Chem. Lett.* **2016**, *7*, 2579-2585.
- (76) Vargas, B.; Ramos, E.; Pérez-Gutiérrez, E.; Alonso, J. C.; Solis-Ibarra, D. A Direct Bandgap Copper-Antimony Halide Perovskite. *J. Am. Chem. Soc.* **2017**, *139*, 9116-9119.
- (77) Leng, M.; Chen, Z.; Yang, Y.; Li, Z.; Zeng, K.; Li, K.; Niu, G.; He, Y.; Zhou, Q.; Tang, J. Lead - Free, Blue Emitting Bismuth Halide Perovskite Quantum Dots. *Angew. Chem. Int. Ed.* **2016**, *55*, 15012-15016.
- (78) Wehrenfennig, C.; Liu, M.; Snaith, H. J.; Johnston, M. B.; Herz, L. M. Charge-Carrier Dynamics in Vapour-Deposited Films of the Organolead Halide Perovskite CH₃NH₃PbI₃-XCl_x. *Energy Environ. Sci.* **2014**, *7*, 2269-2275.

- (79) Stranks, S. D.; Eperon, G. E.; Grancini, G.; Menelaou, C.; Alcocer, M. J.; Leijtens, T.; Herz, L. M.; Petrozza, A.; Snaith, H. J. Electron-Hole Diffusion Lengths Exceeding 1 Micrometer in an Organometal Trihalide Perovskite Absorber. *Science* **2013**, *342*, 341-344.
- (80) Brenner, T. M.; Egger, D. A.; Rappe, A. M.; Kronik, L.; Hodes, G.; Cahen, D. Are Mobilities in Hybrid Organic-Inorganic Halide Perovskites Actually "High"? *J. Phys. Chem. Lett.* **2015**, *6*, 4754-4757.
- (81) Oga, H.; Saeki, A.; Ogomi, Y.; Hayase, S.; Seki, S. Improved Understanding of the Electronic and Energetic Landscapes of Perovskite Solar Cells: High Local Charge Carrier Mobility, Reduced Recombination, and Extremely Shallow Traps. *J. Am. Chem. Soc.* **2014**, *136*, 13818-13825.
- (82) Sum, T. C.; Mathews, N.; Xing, G.; Lim, S. S.; Chong, W. K.; Giovanni, D.; Dewi, H. A. Spectral Features and Charge Dynamics of Lead Halide Perovskites: Origins and Interpretations. *Acc. Chem. Res.* **2016**, *49*, 294-302.
- (83) Manser, J. S.; Kamat, P. V. Band Filling with Free Charge Carriers in Organometal Halide Perovskites. *Nat. Photonics* **2014**, *8*, 737-743.
- (84) Saba, M.; Cadelano, M.; Marongiu, D.; Chen, F.; Sarritzu, V.; Sestu, N.; Figus, C.; Aresti, M.; Piras, R.; Lehmann, A. G. Correlated Electron-Hole Plasma in Organometal Perovskites. *Nat. commun.* **2014**, *5*, 5049.
- (85) Yamada, Y.; Nakamura, T.; Endo, M.; Wakamiya, A.; Kanemitsu, Y. Photocarrier Recombination Dynamics in Perovskite $\text{CH}_3\text{NH}_3\text{PbI}_3$ for Solar Cell Applications. *J. Am. Chem. Soc.* **2014**, *136*, 11610-11613.
- (86) Manger, L. H.; Rowley, M. B.; Fu, Y.; Foote, A. K.; Rea, M. T.; Wood, S. L.; Jin, S.; Wright, J. C.; Goldsmith, R. H. Global Analysis of Perovskite Photophysics Reveals Importance of Geminate Pathways. *J. Phys. Chem. C* **2017**, *121*, 1062-1071.
- (87) Stampelcoskie, K. G.; Manser, J. S.; Kamat, P. V. Dual Nature of the Excited State in Organic-Inorganic Lead Halide Perovskites. *Energy Environ. Sci.* **2015**, *8*, 208-215.
- (88) Wehrenfennig, C.; Eperon, G. E.; Johnston, M. B.; Snaith, H. J.; Herz, L. M. High Charge Carrier Mobilities and Lifetimes in Organolead Trihalide Perovskites. *Adv. Mater.* **2014**, *26*, 1584-1589.
- (89) Johnston, M. B.; Herz, L. M. Hybrid Perovskites for Photovoltaics: Charge-Carrier Recombination, Diffusion, and Radiative Efficiencies. *Acc. Chem. Res.* **2015**, *49*, 146-154.
- (90) Richter, J. M.; Abdi-Jalebi, M.; Sadhanala, A.; Tabachnyk, M.; Rivett, J. P.; Pazos-Outón, L. M.; Gödel, K. C.; Price, M.; Deschler, F.; Friend, R. H. Enhancing Photoluminescence Yields in Lead Halide Perovskites by Photon Recycling and Light out-Coupling. *Nat. commun.* **2016**, *7*, 13941.
- (91) Yang, Y.; Ostrowski, D. P.; France, R. M.; Zhu, K.; van de Lagemaat, J.; Luther, J. M.; Beard, M. C. Observation of a Hot-Phonon Bottleneck in Lead-Iodide Perovskites. *Nat. Photonics* **2015**, *10*, 53-59.
- (92) Rehman, W.; Milot, R. L.; Eperon, G. E.; Wehrenfennig, C.; Boland, J. L.; Snaith, H. J.; Johnston, M. B.; Herz, L. M. Charge - Carrier Dynamics and Mobilities in Formamidinium Lead Mixed - Halide Perovskites. *Adv. Mater.* **2015**, *27*, 7938-7944.
- (93) Beattie, A.; Landsberg, P. Auger Effect in Semiconductors. *Proc. R. Soc. London, Ser. A* **1959**, *249*, 16-29.

- (94) Sheik-Bahae, M.; Epstein, R. I. Can Laser Light Cool Semiconductors? *Phys. Rev. Lett.* **2004**, *92*, 247403.
- (95) Even, J.; Pedesseau, L.; Katan, C. Analysis of Multivalley and Multibandgap Absorption and Enhancement of Free Carriers Related to Exciton Screening in Hybrid Perovskites. *J. Phys. Chem. C* **2014**, *118*, 11566-11572.
- (96) Tanaka, K.; Takahashi, T.; Ban, T.; Kondo, T.; Uchida, K.; Miura, N. Comparative Study on the Excitons in Lead-Halide-Based Perovskite-Type Crystals $\text{CH}_3\text{NH}_3\text{PbBr}_3$ $\text{CH}_3\text{NH}_3\text{PbI}_3$. *Solid State Commun.* **2003**, *127*, 619-623.
- (97) Hirasawa, M.; Ishihara, T.; Goto, T.; Uchida, K.; Miura, N. Magnetoabsorption of the Lowest Exciton in Perovskite-Type Compound $(\text{CH}_3\text{NH}_3)\text{PbI}_3$. *Physica B: Condensed Matter* **1994**, *201*, 427-430.
- (98) Lin, Q.; Armin, A.; Nagiri, R. C. R.; Burn, P. L.; Meredith, P. Electro-Optics of Perovskite Solar Cells. *Nat. Photonics* **2015**, *9*, 106-112.
- (99) Miyata, A.; Mitoglu, A.; Plochocka, P.; Portugall, O.; Wang, J. T.-W.; Stranks, S. D.; Snaith, H. J.; Nicholas, R. J. Direct Measurement of the Exciton Binding Energy and Effective Masses for Charge Carriers in Organic-Inorganic Tri-Halide Perovskites. *Nat. Phys.* **2015**, *11*, 582-587.
- (100) D'Innocenzo, V.; Grancini, G.; Alcocer, M. J.; Kandada, A. R.; Stranks, S. D.; Lee, M. M.; Lanzani, G.; Snaith, H. J.; Petrozza, A. Excitons Versus Free Charges in Organo-Lead Tri-Halide Perovskites. *Nat. Commun.* **2014**, *5*, 3586.
- (101) Savenije, T. J.; Ponseca Jr, C. S.; Kunneman, L.; Abdellah, M.; Zheng, K.; Tian, Y.; Zhu, Q.; Canton, S. E.; Scheblykin, I. G.; Pullerits, T. Thermally Activated Exciton Dissociation and Recombination Control the Carrier Dynamics in Organometal Halide Perovskite. *J. Phys. Chem. Lett.* **2014**, *5*, 2189-2194.
- (102) Wu, K.; Bera, A.; Ma, C.; Du, Y.; Yang, Y.; Li, L.; Wu, T. Temperature-Dependent Excitonic Photoluminescence of Hybrid Organometal Halide Perovskite Films. *Phys. Chem. Chem. Phys.* **2014**, *16*, 22476-22481.
- (103) Sestu, N.; Cadelano, M.; Sarritzu, V.; Chen, F.; Marongiu, D.; Piras, R.; Mainas, M.; Quochi, F.; Saba, M.; Mura, A. Absorption F-Sum Rule for the Exciton Binding Energy in Methylammonium Lead Halide Perovskites. *J. Phys. Chem. Lett.* **2015**, *6*, 4566-4572.
- (104) Sun, S.; Salim, T.; Mathews, N.; Duchamp, M.; Boothroyd, C.; Xing, G.; Sum, T. C.; Lam, Y. M. The Origin of High Efficiency in Low-Temperature Solution-Processable Bilayer Organometal Halide Hybrid Solar Cells. *Energy Environ. Sci.* **2014**, *7*, 399-407.
- (105) Nah, S.; Spokoyny, B.; Stoumpos, C.; Soe, C. M. M.; Kanatzidis, M.; Harel, E. Spatially Segregated Free-Carrier and Exciton Populations in Individual Lead Halide Perovskite Grains. *Nat. Photonics* **2017**, *11*, 285-288.
- (106) Gélvez-Rueda, M. C.; Hutter, E. M.; Cao, D. H.; Renaud, N.; Stoumpos, C. C.; Hupp, J. T.; Savenije, T. J.; Kanatzidis, M. G.; Grozema, F. C. Interconversion between Free Charges and Bound Excitons in 2d Hybrid Lead Halide Perovskites. *J. Phys. Chem. C* **2017**, *121*, 26566-26574.
- (107) de Mello, J. C.; Wittmann, H. F.; Friend, R. H. An Improved Experimental Determination of External Photoluminescence Quantum Efficiency. *Adv. Mater.* **1997**, *9*, 230-232.
- (108) Deschler, F.; Price, M.; Pathak, S.; Klintberg, L. E.; Jarausch, D.-D.; Högler, R.; Hüttner, S.; Leijtens, T.; Stranks, S. D.; Snaith, H. J. et al. High Photoluminescence Efficiency and Optically Pumped Lasing in Solution-Processed Mixed Halide Perovskite Semiconductors. *J. Phys. Chem. Lett.* **2014**, *5*, 1421-1426.

- (109) Pan, J.; Quan, L. N.; Zhao, Y.; Peng, W.; Murali, B.; Sarmah, S. P.; Yuan, M.; Sinatra, L.; Alyami, N. M.; Liu, J. et al. Highly Efficient Perovskite-Quantum-Dot Light-Emitting Diodes by Surface Engineering. *Adv. Mater.* **2016**, *28*, 8718-8725.
- (110) Liu, F.; Zhang, Y.; Ding, C.; Kobayashi, S.; Izuishi, T.; Nakazawa, N.; Toyoda, T.; Ohta, T.; Hayase, S.; Minemoto, T. Highly Luminescent Phase-Stable CsPbI₃ Perovskite Quantum Dots Achieving near 100% Absolute Photoluminescence Quantum Yield. *ACS nano* **2017**, *11*, 10373-10383.
- (111) Hattori, T.; Taira, T.; Era, M.; Tsutsui, T.; Saito, S. Highly Efficient Electroluminescence from a Heterostructure Device Combined with Emissive Layered-Perovskite and an Electron-Transporting Organic Compound. *Chem. Phys. Lett.* **1996**, *254*, 103-108.
- (112) Kim, Y. H.; Cho, H.; Heo, J. H.; Kim, T. S.; Myoung, N.; Lee, C. L.; Im, S. H.; Lee, T. W. Multicolored Organic/Inorganic Hybrid Perovskite Light-Emitting Diodes. *Adv. Mater.* **2015**, *27*, 1248.
- (113) Li, G.; Tan, Z. K.; Di, D.; Lai, M. L.; Jiang, L.; Lim, J. H.; Friend, R. H.; Greenham, N. C. Efficient Light-Emitting Diodes Based on Nanocrystalline Perovskite in a Dielectric Polymer Matrix. *Nano Lett.* **2015**, *15*, 2640-2644.
- (114) Li, J.; Bade, S. G.; Shan, X.; Yu, Z. Single-Layer Light-Emitting Diodes Using Organometal Halide Perovskite/Poly(Ethylene Oxide) Composite Thin Films. *Adv. Mater.* **2015**, *27*, 5196.
- (115) Park, M.-H.; Jeong, S.-H.; Seo, H.-K.; Wolf, C.; Kim, Y.-H.; Kim, H.; Byun, J.; Kim, J. S.; Cho, H.; Lee, T.-W. Unravelling Additive-Based Nanocrystal Pinning for High Efficiency Organic-Inorganic Halide Perovskite Light-Emitting Diodes. *Nano Energy* **2017**, *42*, 157-165.
- (116) Cho, H.; Kim, J. S.; Wolf, C.; Kim, Y.-H.; Yun, H. J.; Jeong, S.-H.; Sadhanala, A.; Venugopalan, V.; Choi, J. W.; Lee, C.-L. et al. High-Efficiency Polycrystalline Perovskite Light-Emitting Diodes Based on Mixed Cations. *ACS nano* **2018**, *12*, 2883-2892.
- (117) Zhang, S.; Yi, C.; Wang, N.; Sun, Y.; Zou, W.; Wei, Y.; Cao, Y.; Miao, Y.; Li, R.; Yin, Y. et al. Efficient Red Perovskite Light-Emitting Diodes Based on Solution-Processed Multiple Quantum Wells. *Adv. Mater.* **2017**, *29*.
- (118) Rehman, W.; McMeekin, D. P.; Patel, J. B.; Milot, R. L.; Johnston, M. B.; Snaith, H. J.; Herz, L. M. Photovoltaic Mixed-Cation Lead Mixed-Halide Perovskites: Links between Crystallinity, Photo-Stability and Electronic Properties. *Energy Environ. Sci.* **2017**, *10*, 361-369.
- (119) Kulkarni, S. A.; Muduli, S.; Xing, G.; Yantara, N.; Li, M.; Chen, S.; Sum, T. C.; Mathews, N.; White, T. J.; Mhaisalkar, S. G. Modulating Excitonic Recombination Effects through One - Step Synthesis of Perovskite Nanoparticles for Light - Emitting Diodes. *ChemSusChem* **2017**, *10*, 3818-3824.
- (120) Protesescu, L.; Yakunin, S.; Bodnarchuk, M. I.; Krieg, F.; Caputo, R.; Hendon, C. H.; Yang, R. X.; Walsh, A.; Kovalenko, M. V. Nanocrystals of Cesium Lead Halide Perovskites (CsPbX₃, X = Cl, Br, and I): Novel Optoelectronic Materials Showing Bright Emission with Wide Color Gamut. *Nano Lett.* **2015**, *15*, 3692-3696.
- (121) Li, G.; Rivarola, F. W.; Davis, N. J.; Bai, S.; Jellicoe, T. C.; de la Pena, F.; Hou, S.; Ducati, C.; Gao, F.; Friend, R. H. et al. Highly Efficient Perovskite Nanocrystal Light-Emitting Diodes Enabled by a Universal Crosslinking Method. *Adv. Mater.* **2016**, *28*, 3528-3534.

- (122) Song, J.; Li, J.; Li, X.; Xu, L.; Dong, Y.; Zeng, H. Quantum Dot Light-Emitting Diodes Based on Inorganic Perovskite Cesium Lead Halides (CsPbX₃). *Adv. Mater.* **2015**, *27*, 7162-7167.
- (123) Li, J.; Xu, L.; Wang, T.; Song, J.; Chen, J.; Xue, J.; Dong, Y.; Cai, B.; Shan, Q.; Han, B. et al. 50-Fold EQE Improvement up to 6.27% of Solution Processed All-Inorganic Perovskite CsPbBr₃ QLEDs Via Surface Ligand Density Control. *Adv. Mater.* **2017**, *29*, 1603885.
- (124) Zhang, X.; Liu, H.; Wang, W.; Zhang, J.; Xu, B.; Karen, K. L.; Zheng, Y.; Liu, S.; Chen, S.; Wang, K. et al. Hybrid Perovskite Light-Emitting Diodes Based on Perovskite Nanocrystals with Organic-Inorganic Mixed Cations. *Adv. Mater.* **2017**, *29*, 1606405.
- (125) Yuan, S.; Wang, Z.-K.; Zhuo, M.-P.; Tian, Q.; Jin, Y.; Liao, L.-S. Self-Assembled High Quality CsPbBr₃ Quantum Dot Films toward Highly Efficient Light-Emitting Diodes. *ACS nano* **2018**, *12*, 9541-9548.
- (126) Protesescu, L.; Yakunin, S.; Kumar, S.; Bär, J.; Bertolotti, F.; Masciocchi, N.; Guagliardi, A.; Grotevent, M.; Shorubalko, I.; Bodnarchuk, M. I. Dismantling the “Red Wall” of Colloidal Perovskites: Highly Luminescent Formamidinium and Formamidinium-Cesium Lead Iodide Nanocrystals. *ACS nano* **2017**, *11*, 3119-3134.
- (127) Kim, Y.-H.; Lee, G.-H.; Kim, Y.-T.; Wolf, C.; Yun, H. J.; Kwon, W.; Park, C. G.; Lee, T.-W. High Efficiency Perovskite Light-Emitting Diodes of Ligand-Engineered Colloidal Formamidinium Lead Bromide Nanoparticles. *Nano Energy* **2017**, *38*, 51-58.
- (128) Kim, Y.-H.; Wolf, C.; Kim, Y.-T.; Cho, H.; Kwon, W.; Do, S.; Sadhanala, A.; Park, C. G.; Rhee, S.-W.; Im, S. H. Highly Efficient Light-Emitting Diodes of Colloidal Metal-Halide Perovskite Nanocrystals Beyond Quantum Size. *ACS nano* **2017**, *11*, 6586-6593.
- (129) Chin, X. Y.; Perumal, A.; Bruno, A.; Yantara, N.; Veldhuis, S. A.; Martínez-Sarti, L.; Chandran, B.; Chirvony, V.; Lo, A. S.-Z.; So, J. Self-Assembled Hierarchical Nanostructured Perovskites Enable Highly Efficient LEDs Via an Energy Cascade. *Energy Environ. Sci.* **2018**, *11*, 1770-1778.
- (130) Yang, J.; Siempelkamp, B. D.; Mosconi, E.; De Angelis, F.; Kelly, T. L. Origin of the Thermal Instability in CH₃NH₃PbI₃ Thin Films Deposited on ZnO. *Chem. Mater.* **2015**, *27*, 4229-4236.
- (131) Wang, J.; Wang, N.; Jin, Y.; Si, J.; Tan, Z. K.; Du, H.; Cheng, L.; Dai, X.; Bai, S.; He, H. et al. Interfacial Control toward Efficient and Low-Voltage Perovskite Light-Emitting Diodes. *Adv. Mater.* **2015**, *27*, 2311.
- (132) Chih, Y. K.; Wang, J. C.; Yang, R. T.; Liu, C. C.; Chang, Y. C.; Fu, Y. S.; Lai, W. C.; Chen, P.; Wen, T. C.; Huang, Y. C. et al. NiO_x Electrode Interlayer and CH₃NH₂/CH₃NH₃PbBr₃ Interface Treatment to Markedly Advance Hybrid Perovskite-Based Light-Emitting Diodes. *Adv. Mater.* **2016**, *28*, 8687-8694.
- (133) Seo, H. K.; Kim, H.; Lee, J.; Park, M. H.; Jeong, S. H.; Kim, Y. H.; Kwon, S. J.; Han, T. H.; Yoo, S.; Lee, T. W. Efficient Flexible Organic/Inorganic Hybrid Perovskite Light - Emitting Diodes Based on Graphene Anode. *Adv. Mater.* **2017**, *29*, 1605587.
- (134) Lee, B. R.; Yu, J. C.; Park, J. H.; Lee, S.; Mai, C.-K.; Zhao, B.; Wong, M. S.; Jung, E. D.; Nam, Y. S.; Park, S. Y. Conjugated Polyelectrolytes as Efficient Hole Transport Layers in Perovskite Light-Emitting Diodes. *ACS nano* **2018**, *12*, 5826-5833.

- (135) Zhang, L.; Yang, X.; Jiang, Q.; Wang, P.; Yin, Z.; Zhang, X.; Tan, H.; Yang, Y. M.; Wei, M.; Sutherland, B. R. et al. Ultra-Bright and Highly Efficient Inorganic Based Perovskite Light-Emitting Diodes. *Nat. commun.* **2017**, *8*, 15640.
- (136) Yan, F.; Xing, J.; Xing, G.; Quan, L.; Tan, S. T.; Zhao, J.; Su, R.; Zhang, L.; Chen, S.; Zhao, Y. Highly Efficient Visible Colloidal Lead-Halide Perovskite Nanocrystal Light-Emitting Diodes. *Nano Lett.* **2018**, *18*, 3157-3164.
- (137) Lu, L. P.; Kabra, D.; Johnson, K.; Friend, R. H. Charge - Carrier Balance and Color Purity in Polyfluorene Polymer Blends for Blue Light - Emitting Diodes. *Adv. Funct. Mater.* **2012**, *22*, 144-150.
- (138) Nguyen, W. H.; Bailie, C. D.; Unger, E. L.; McGehee, M. D. Enhancing the Hole-Conductivity of Spiro-Ometad without Oxygen or Lithium Salts by Using Spiro (Tfsi) 2 in Perovskite and Dye-Sensitized Solar Cells. *J. Am. Chem. Soc.* **2014**, *136*, 10996-11001.
- (139) Hoyer, R. L.; Chua, M. R.; Musselman, K. P.; Li, G.; Lai, M. L.; Tan, Z. K.; Greenham, N. C.; MacManus-Driscoll, J. L.; Friend, R. H.; Credgington, D. Enhanced Performance in Fluorene-Free Organometal Halide Perovskite Light-Emitting Diodes Using Tunable, Low Electron Affinity Oxide Electron Injectors. *Adv. Mater.* **2015**, *27*, 1414-1419.
- (140) Chih, Y. K.; Wang, J. C.; Yang, R. T.; Liu, C. C.; Chang, Y. C.; Fu, Y. S.; Lai, W. C.; Chen, P.; Wen, T. C.; Huang, Y. C. NiOx Electrode Interlayer and CH₃NH₂/CH₃NH₃PbBr₃ Interface Treatment to Markedly Advance Hybrid Perovskite - Based Light - Emitting Diodes. *Adv. Mater.* **2016**, *28*, 8687-8694.
- (141) Liang, D.; Peng, Y.; Fu, Y.; Shearer, M. J.; Zhang, J.; Zhai, J.; Zhang, Y.; Hamers, R. J.; Andrew, T. L.; Jin, S. Color-Pure Violet-Light-Emitting Diodes Based on Layered Lead Halide Perovskite Nanoplates. *ACS nano* **2016**, *10*, 6897-6904.
- (142) Xing, J.; Zhao, Y. B.; Askerka, M.; Quan, L. N.; Gong, X. W.; Zhao, W. J.; Zhao, J. X.; Tan, H. R.; Long, G. K.; Gao, L. et al. Color-Stable Highly Luminescent Sky-Blue Perovskite Light-Emitting Diodes. *Nat. commun.* **2018**, *9*.
- (143) Kim, H. P.; Kim, J.; Kim, B. S.; Kim, H.-M.; Kim, J.; Yusoff, A. R. b. M.; Jang, J.; Nazeeruddin, M. K. High-Efficiency, Blue, Green, and near-Infrared Light-Emitting Diodes Based on Triple Cation Perovskite. *Adv. Optical Mater.* **2017**, *5*, 1600920.
- (144) Pan, J.; Quan, L. N.; Zhao, Y.; Peng, W.; Murali, B.; Sarmah, S. P.; Yuan, M.; Sinatra, L.; Alyami, N. M.; Liu, J. Highly Efficient Perovskite - Quantum - Dot Light - Emitting Diodes by Surface Engineering. *Adv. Mater.* **2016**, *28*, 8718-8725.
- (145) Hou, S. C.; Gangishetty, M. K.; Quan, Q. M.; Congreve, D. N. Efficient Blue and White Perovskite Light-Emitting Diodes Via Manganese Doping. *Joule* **2018**, *2*, 2421-2433.
- (146) Li, Z. C.; Chen, Z. M.; Yang, Y. C.; Xue, Q. F.; Yip, H. L.; Cao, Y. Modulation of Recombination Zone Position for Quasi-Two-Dimensional Blue Perovskite Light-Emitting Diodes with Efficiency Exceeding 5%. *Nat. commun.* **2019**, *10*.
- (147) Kim, Y. H.; Cho, H.; Heo, J. H.; Kim, T. S.; Myoung, N.; Lee, C. L.; Im, S. H.; Lee, T. W. Multicolored Organic/Inorganic Hybrid Perovskite Light - Emitting Diodes. *Adv. Mater.* **2015**, *27*, 1248-1254.
- (148) Li, G.; Tan, Z.-K.; Di, D.; Lai, M. L.; Jiang, L.; Lim, J. H.-W.; Friend, R. H.; Greenham, N. C. Efficient Light-Emitting Diodes Based on Nanocrystalline Perovskite in a Dielectric Polymer Matrix. *Nano Lett.* **2015**, *15*, 2640.

- (149) Meng, L.; Yao, E. P.; Hong, Z.; Chen, H.; Sun, P.; Yang, Z.; Li, G.; Yang, Y. Pure Formamidinium - Based Perovskite Light - Emitting Diodes with High Efficiency and Low Driving Voltage. *Adv. Mater.* **2017**, *29*, 1603826.
- (150) Li, J.; Bade, S. G. R.; Shan, X.; Yu, Z. Single - Layer Light - Emitting Diodes Using Organometal Halide Perovskite/Poly (Ethylene Oxide) Composite Thin Films. *Adv. Mater.* **2015**, *27*, 5196-5202.
- (151) Li, J.; Xu, L.; Wang, T.; Song, J.; Chen, J.; Xue, J.; Dong, Y.; Cai, B.; Shan, Q.; Han, B. 50 - Fold E_q Improvement up to 6.27% of Solution - Processed All - Inorganic Perovskite CsPbBr₃ QLEDs Via Surface Ligand Density Control. *Adv. Mater.* **2017**, *29*, 1603885.
- (152) Zhao, L.; Yeh, Y.-W.; Tran, N. L.; Wu, F.; Xiao, Z.; Kerner, R. A.; Lin, Y. L.; Scholes, G. D.; Yao, N.; Rand, B. P. In Situ Preparation of Metal Halide Perovskite Nanocrystal Thin Films for Improved Light-Emitting Devices. *ACS nano* **2017**, *11*, 3957.
- (153) Cho, H.; Jeong, S.-H.; Park, M.-H.; Kim, Y.-H.; Wolf, C.; Lee, C.-L.; Heo, J. H.; Sadhanala, A.; Myoung, N.; Yoo, S. et al. Overcoming the Electroluminescence Efficiency Limitations of Perovskite Light-Emitting Diodes. *Science* **2015**, *350*, 1222-1225.
- (154) Lee, S.; Park, J. H.; Nam, Y. S.; Lee, B. R.; Zhao, B.; Di Nuzzo, D.; Jung, E. D.; Jeon, H.; Kim, J.-Y.; Jeong, H. Y. Growth of Nanosized Single Crystals for Efficient Perovskite Light-Emitting Diodes. *ACS nano* **2018**, *12*, 3417-3423.
- (155) Yan, F.; Xing, J.; Xing, G.; Quan, L. N.; Tan, S. T.; Zhao, J.; Su, R.; Zhang, L.; Chen, S.; Zhao, Y. Highly Efficient Visible Colloidal Lead-Halide Perovskite Nanocrystal Light-Emitting Diodes. *Nano Lett.* **2018**, *18*, 3157.
- (156) Zou, Y.; Huang, Q.; Yang, Y.; Ban, M.; Li, S.; Han, Y.; Wu, T.; Tan, Y.; Gao, X.; Song, T. Efficient Perovskite Light - Emitting Diodes Via Tuning Nanoplatelet Distribution and Crystallinity Orientation. *Adv. Mater. Interfaces* **2018**, 1801030.
- (157) Yang, X.; Zhang, X.; Deng, J.; Chu, Z.; Jiang, Q.; Meng, J.; Wang, P.; Zhang, L.; Yin, Z.; You, J. Efficient Green Light-Emitting Diodes Based on Quasi-Two-Dimensional Composition and Phase Engineered Perovskite with Surface Passivation. *Nat. commun.* **2018**, *9*, 570.
- (158) Cheng, L. P.; Huang, J. S.; Shen, Y.; Li, G. P.; Liu, X. K.; Li, W.; Wang, Y. H.; Li, Y. Q.; Jiang, Y.; Gao, F. et al. Efficient CsPbBr₃ Perovskite Light-Emitting Diodes Enabled by Synergetic Morphology Control. *Adv. Optical Mater.* **2019**, *7*.
- (159) Ban, M.; Zou, Y.; Rivett, J. P.; Yang, Y.; Thomas, T. H.; Tan, Y.; Song, T.; Gao, X.; Credington, D.; Deschler, F. Solution-Processed Perovskite Light Emitting Diodes with Efficiency Exceeding 15% through Additive-Controlled Nanostructure Tailoring. *Nat. commun.* **2018**, *9*, 3892.
- (160) Yuan, S.; Wang, Z. K.; Zhuo, M. P.; Tian, Q. S.; Jin, Y.; Liao, L. S. Self-Assembled High Quality CsPbBr₃ Quantum Dot Films toward Highly Efficient Light-Emitting Diodes. *ACS Nano* **2018**, *12*, 9541-9548.
- (161) Song, J. Z.; Fang, T.; Li, J. H.; Xu, L. M.; Zhang, F. J.; Han, B. N.; Shan, Q. S.; Zeng, H. B. Organic-Inorganic Hybrid Passivation Enables Perovskite QLEDs with an E_q of 16.48%. *Adv. Mater.* **2018**, *30*.
- (162) Lin, K.; Xing, J.; Quan, L. N.; de Arquer, F. P. G.; Gong, X.; Lu, J.; Xie, L.; Zhao, W.; Zhang, D.; Yan, C. Perovskite Light-Emitting Diodes with External Quantum Efficiency Exceeding 20 Per Cent. *Nature* **2018**, *562*, 245-248.

- (163) Li, G.; Rivarola, F. W. R.; Davis, N. J.; Bai, S.; Jellicoe, T. C.; de la Peña, F.; Hou, S.; Ducati, C.; Gao, F.; Friend, R. H. Highly Efficient Perovskite Nanocrystal Light - Emitting Diodes Enabled by a Universal Crosslinking Method. *Adv. Mater.* **2016**, *28*, 3528-3534.
- (164) Qasim, K.; Wang, B.; Zhang, Y.; Li, P.; Wang, Y.; Li, S.; Lee, S. T.; Liao, L. S.; Lei, W.; Bao, Q. Solution - Processed Extremely Efficient Multicolor Perovskite Light - Emitting Diodes Utilizing Doped Electron Transport Layer. *Adv. Funct. Mater.* **2017**, *27*, 1606874.
- (165) Lu, M.; Zhang, X.; Bai, X.; Wu, H.; Shen, X.; Zhang, Y.; Zhang, W.; Zheng, W.; Song, H.; Yu, W. W. et al. Spontaneous Silver Doping and Surface Passivation of CsPbI₃ Perovskite Active Layer Enable Light-Emitting Devices with an External Quantum Efficiency of 11.2. *ACS Energy Lett.* **2018**, *3*, 1571-1577.
- (166) Lu, M.; Zhang, X. Y.; Zhang, Y.; Guo, J.; Shen, X. Y.; Yu, W. W.; Rogach, A. L. Simultaneous Strontium Doping and Chlorine Surface Passivation Improve Luminescence Intensity and Stability of CsPbI₃ Nanocrystals Enabling Efficient Light-Emitting Devices. *Adv. Mater.* **2018**, *30*.
- (167) Chiba, T.; Hayashi, Y.; Ebe, H.; Hoshi, K.; Sato, J.; Sato, S.; Pu, Y. J.; Ohisa, S.; Kido, J. Anion-Exchange Red Perovskite Quantum Dots with Ammonium Iodine Salts for Highly Efficient Light-Emitting Devices. *Nat. Photonics* **2018**, *12*, 681-+.
- (168) Tan, Z.-K.; Moghaddam, R. S.; Lai, M. L.; Docampo, P.; Higler, R.; Deschler, F.; Price, M.; Sadhanala, A.; Pazos, L. M.; Credgington, D. Bright Light-Emitting Diodes Based on Organometal Halide Perovskite. *Nat. Nanotechnol.* **2014**, *9*, 687-692.
- (169) Wang, J.; Wang, N.; Jin, Y.; Si, J.; Tan, Z. K.; Du, H.; Cheng, L.; Dai, X.; Bai, S.; He, H. Interfacial Control toward Efficient and Low - Voltage Perovskite Light - Emitting Diodes. *Adv. Mater.* **2015**, *27*, 2311-2316.
- (170) Yuan, M.; Quan, L. N.; Comin, R.; Walters, G.; Sabatini, R.; Voznyy, O.; Hoogland, S.; Zhao, Y.; Beauregard, E. M.; Kanjanaboos, P. Perovskite Energy Funnels for Efficient Light-Emitting Diodes. *Nat. Nanotechnol.* **2016**, *11*, 872.
- (171) Cao, Y.; Wang, N.; Tian, H.; Guo, J.; Wei, Y.; Chen, H.; Miao, Y.; Zou, W.; Pan, K.; He, Y. et al. Perovskite Light-Emitting Diodes Based on Spontaneously Formed Submicrometre-Scale Structures. *Nature* **2018**, *562*, 249-253.
- (172) Xu, W.; Hu, Q.; Bai, S.; Bao, C.; Miao, Y.; Yuan, Z.; Borzda, T.; Barker, A. J.; Tyukalova, E.; Hu, Z. et al. Rational Molecular Passivation for High-Performance Perovskite Light-Emitting Diodes. *Nat. Photonics* **2019**, DOI:10.1038/s41566-019-0390-x 10.1038/s41566-019-0390-x.
- (173) Wood, V.; Bulović, V. Colloidal Quantum Dot Light-Emitting Devices. *Nano reviews* **2010**, *1*, 5202.
- (174) Zhao, L.; Rolston, N.; Lee, K. M.; Zhao, X.; Reyes - Martinez, M. A.; Tran, N. L.; Yeh, Y. W.; Yao, N.; Scholes, G. D.; Loo, Y. L. Influence of Bulky Organo - Ammonium Halide Additive Choice on the Flexibility and Efficiency of Perovskite Light - Emitting Devices. *Adv. Funct. Mater.* **2018**, 1802060.
- (175) Dai, X.; Zhang, Z.; Jin, Y.; Niu, Y.; Cao, H.; Liang, X.; Chen, L.; Wang, J.; Peng, X. Solution-Processed, High-Performance Light-Emitting Diodes Based on Quantum Dots. *Nature* **2014**, *515*, 96-99.
- (176) Zeng, W.; Lai, H. Y.; Lee, W. K.; Jiao, M.; Shiu, Y. J.; Zhong, C.; Gong, S.; Zhou, T.; Xie, G.; Sarma, M. Achieving Nearly 30% External Quantum Efficiency for Orange - Red

- Organic Light Emitting Diodes by Employing Thermally Activated Delayed Fluorescence Emitters Composed of 1, 8 - Naphthalimide - Acridine Hybrids. *Adv. Mater.* **2018**, *30*, 1704961.
- (177) Yang, Y.; Zheng, Y.; Cao, W.; Titov, A.; Hyvonen, J.; Manders, J. R.; Xue, J.; Holloway, P. H.; Qian, L. High-Efficiency Light-Emitting Devices Based on Quantum Dots with Tailored Nanostructures. *Nat. Photonics* **2015**, *9*, 259-266.
- (178) Di, D.; Romanov, A. S.; Yang, L.; Richter, J. M.; Rivett, J. P.; Jones, S.; Thomas, T. H.; Jalebi, M. A.; Friend, R. H.; Linnolahti, M. High-Performance Light-Emitting Diodes Based on Carbene-Metal-Amides. *Science* **2017**, *356*, 159-163.
- (179) Xing, J.; Zhao, Y.; Askerka, M.; Quan, L. N.; Gong, X.; Zhao, W.; Zhao, J.; Tan, H.; Long, G.; Gao, L. Color-Stable Highly Luminescent Sky-Blue Perovskite Light-Emitting Diodes. *Nat. commun.* **2018**, *9*, 3541.
- (180) Lee, C. W.; Lee, J. Y. Above 30% External Quantum Efficiency in Blue Phosphorescent Organic Light - Emitting Diodes Using Pyrido [2, 3 - B] Indole Derivatives as Host Materials. *Adv. Mater.* **2013**, *25*, 5450-5454.
- (181) Zhao, L.; Yeh, Y. W.; Tran, N. L.; Wu, F.; Xiao, Z.; Kerner, R. A.; Lin, Y. L.; Scholes, G. D.; Yao, N.; Rand, B. P. In Situ Preparation of Metal Halide Perovskite Nanocrystal Thin Films for Improved Light-Emitting Devices. *ACS Nano* **2017**, *11*, 3957-3964.
- (182) <http://www.udcoled.com/>. Universal Display Corporation. (accessed April 3, 2019).
- (183) Morgan, N. Y.; Leatherdale, C.; Drndić, M.; Jarosz, M. V.; Kastner, M. A.; Bawendi, M. Electronic Transport in Films of Colloidal Cdse Nanocrystals. *Phys. Rev. B* **2002**, *66*, 075339.
- (184) Lee, J.; Sundar, V. C.; Heine, J. R.; Bawendi, M. G.; Jensen, K. F. Full Color Emission from Ii-Vi Semiconductor Quantum Dot-Polymer Composites. *Adv. Mater.* **2000**, *12*, 1102-1105.
- (185) Wood, V.; Panzer, M. J.; Chen, J.; Bradley, M. S.; Halpert, J. E.; Bawendi, M. G.; Bulović, V. Inkjet - Printed Quantum Dot-Polymer Composites for Full - Color Ac - Driven Displays. *Adv. Mater.* **2009**, *21*, 2151-2155.
- (186) Kagan, C.; Murray, C.; Bawendi, M. Long-Range Resonance Transfer of Electronic Excitations in Close-Packed Cdse Quantum-Dot Solids. *Phys. Rev. B* **1996**, *54*, 8633.
- (187) Borchardt, J. K. Developments in Organic Displays. *Mater. Today* **2004**, *7*, 42-46.
- (188) Reineke, S.; Lindner, F.; Schwartz, G.; Seidler, N.; Walzer, K.; Lüssem, B.; Leo, K. White Organic Light-Emitting Diodes with Fluorescent Tube Efficiency. *Nature* **2009**, *459*, 234-238.
- (189) Kabra, D.; Lu, L. P.; Song, M. H.; Snaith, H. J.; Friend, R. H. Efficient Single - Layer Polymer Light - Emitting Diodes. *Adv. Mater.* **2010**, *22*, 3194-3198.
- (190) Shimada, Y.; Ishino, J.; Shirasaki, S.; Irie, T.; Kikuchi, A. Effect of MgZnO-Bilayer/Ba-Ch3 Combination Interlayer on Emission Characteristics of MoO₃/F8bt/ZnO Hybrid Light Emitting Diodes Fabricated on ZnO/Ag/ZnO Transparent Cathode. *Displays* **2013**, *34*, 437-441.
- (191) Bharathan, J.; Yang, Y. Polymer Electroluminescent Devices Processed by Inkjet Printing: I. Polymer Light-Emitting Logo. *Appl. Phys. Lett.* **1998**, *72*, 2660-2662.
- (192) Aziz, H.; Popovic, Z. D.; Hu, N.-X.; Hor, A.-M.; Xu, G. Degradation Mechanism of Small Molecule-Based Organic Light-Emitting Devices. *Science* **1999**, *283*, 1900-1902.

- (193) Cho, H.; Kim, Y. H.; Wolf, C.; Lee, H. D.; Lee, T. W. Improving the Stability of Metal Halide Perovskite Materials and Light - Emitting Diodes. *Adv. Mater.* **2018**, 1704587.
- (194) Arora, N.; Dar, M. I.; Hinderhofer, A.; Pellet, N.; Schreiber, F.; Zakeeruddin, S. M.; Grätzel, M. Perovskite Solar Cells with Cuscn Hole Extraction Layers Yield Stabilized Efficiencies Greater Than 20%. *Science* **2017**, 5655.
- (195) Bryant, D.; Aristidou, N.; Pont, S.; Sanchez-Molina, I.; Chotchunangatchaval, T.; Wheeler, S.; Durrant, J. R.; Haque, S. A. Light and Oxygen Induced Degradation Limits the Operational Stability of Methylammonium Lead Triiodide Perovskite Solar Cells. *Energy Environ. Sci.* **2016**, 9, 1655-1660.
- (196) Eames, C.; Frost, J. M.; Barnes, P. R.; O'regan, B. C.; Walsh, A.; Islam, M. S. Ionic Transport in Hybrid Lead Iodide Perovskite Solar Cells. *Nat. commun.* **2015**, 6, 7497.
- (197) Ahn, N.; Kwak, K.; Jang, M. S.; Yoon, H.; Lee, B. Y.; Lee, J.-K.; Pikhitsa, P. V.; Byun, J.; Choi, M. Trapped Charge-Driven Degradation of Perovskite Solar Cells. *Nat. commun.* **2016**, 7, 13422.
- (198) Aristidou, N.; Eames, C.; Sanchez-Molina, I.; Bu, X.; Kosco, J.; Islam, M. S.; Haque, S. A. Fast Oxygen Diffusion and Iodide Defects Mediate Oxygen-Induced Degradation of Perovskite Solar Cells. *Nat. commun.* **2017**, 8, 15218.
- (199) Fan, Z.; Xiao, H.; Wang, Y.; Zhao, Z.; Lin, Z.; Cheng, H.-C.; Lee, S.-J.; Wang, G.; Feng, Z.; Goddard III, W. A. Layer-by-Layer Degradation of Methylammonium Lead Tri-Iodide Perovskite Microplates. *Joule* **2017**, 1, 548-562.
- (200) Niu, G.; Li, W.; Meng, F.; Wang, L.; Dong, H.; Qiu, Y. Study on the Stability of $\text{CH}_3\text{NH}_3\text{PbI}_3$ Films and the Effect of Post-Modification by Aluminum Oxide in All-Solid-State Hybrid Solar Cells. *J. Mater. Chem. A* **2014**, 2, 705-710.
- (201) Burschka, J.; Pellet, N.; Moon, S.-J.; Humphry-Baker, R.; Gao, P.; Nazeeruddin, M. K.; Grätzel, M. Sequential Deposition as a Route to High-Performance Perovskite-Sensitized Solar Cells. *Nature* **2013**, 499, 316-319.
- (202) Zhang, L.; Ju, M.-G.; Liang, W. The Effect of Moisture on the Structures and Properties of Lead Halide Perovskites: A First-Principles Theoretical Investigation. *Phys. Chem. Chem. Phys.* **2016**, 18, 23174-23183.
- (203) Habisreutinger, S. N.; Leijtens, T.; Eperon, G. E.; Stranks, S. D.; Nicholas, R. J.; Snaith, H. J. Carbon Nanotube/Polymer Composites as a Highly Stable Hole Collection Layer in Perovskite Solar Cells. *Nano Lett.* **2014**, 14, 5561-5568.
- (204) Ahn, N.; Kwak, K.; Jang, M. S.; Yoon, H.; Lee, B. Y.; Lee, J. K.; Pikhitsa, P. V.; Byun, J.; Choi, M. Trapped Charge-Driven Degradation of Perovskite Solar Cells. *Nat. commun.* **2016**, 7, 13422.
- (205) Galisteo-López, J. F.; Anaya, M.; Calvo, M.; Míguez, H. Environmental Effects on the Photophysics of Organic-Inorganic Halide Perovskites. *J. Phys. Chem. Lett.* **2015**, 6, 2200-2205.
- (206) Stranks, S. D.; Burlakov, V. M.; Leijtens, T.; Ball, J. M.; Goriely, A.; Snaith, H. J. Recombination Kinetics in Organic-Inorganic Perovskites: Excitons, Free Charge, and Subgap States. *Phys. Rev. Appl.* **2014**, 2, 034007.
- (207) Christians, J. A.; Miranda Herrera, P. A.; Kamat, P. V. Transformation of the Excited State and Photovoltaic Efficiency of $\text{CH}_3\text{NH}_3\text{PbI}_3$ Perovskite Upon Controlled Exposure to Humidified Air. *J. Am. Chem. Soc.* **2015**, 137, 1530-1538.

- (208) Gottesman, R.; Haltzi, E.; Gouda, L.; Tirosh, S.; Bouhadana, Y.; Zaban, A.; Mosconi, E.; De Angelis, F. Extremely Slow Photoconductivity Response of $\text{CH}_3\text{NH}_3\text{PbI}_3$ Perovskites Suggesting Structural Changes under Working Conditions. *J. Phys. Chem. Lett.* **2014**, *5*, 2662-2669.
- (209) Merdasa, A.; Bag, M.; Tian, Y.; Källman, E.; Dobrovolsky, A.; Scheblykin, I. G. Super-Resolution Luminescence Microspectroscopy Reveals the Mechanism of Photoinduced Degradation in $\text{CH}_3\text{NH}_3\text{PbI}_3$ Perovskite Nanocrystals. *J. Phys. Chem. C* **2016**, *120*, 10711-10719.
- (210) Yuan, Y.; Huang, J. Ion Migration in Organometal Trihalide Perovskite and Its Impact on Photovoltaic Efficiency and Stability. *Acc. Chem. Res.* **2016**, *49*, 286-293.
- (211) Lee, S.; Park, J. H.; Lee, B. R.; Jung, E. D.; Yu, J. C.; Di Nuzzo, D.; Friend, R. H.; Song, M. H. Amine-Based Passivating Materials for Enhanced Optical Properties and Performance of Organic-Inorganic Perovskites in Light-Emitting Diodes. *J. Phys. Chem. Lett.* **2017**, *8*, 1784-1792.
- (212) Back, H.; Kim, G.; Kim, J.; Kong, J.; Kim, T. K.; Kang, H.; Kim, H.; Lee, J.; Lee, S.; Lee, K. Achieving Long-Term Stable Perovskite Solar Cells Via Ion Neutralization. *Energy Environ. Sci.* **2016**, *9*, 1258-1263.
- (213) Besleaga, C.; Abramiuc, L. E.; Stancu, V.; Tomulescu, A. G.; Sima, M.; Trinca, L.; Plugaru, N.; Pintilie, L.; Nemnes, G. A.; Iliescu, M. Iodine Migration and Degradation of Perovskite Solar Cells Enhanced by Metallic Electrodes. *J. Phys. Chem. Lett.* **2016**, *7*, 5168-5175.
- (214) Zhao, L.; Kerner, R. A.; Xiao, Z.; Lin, Y. L.; Lee, K. M.; Schwartz, J.; Rand, B. P. Redox Chemistry Dominates the Degradation and Decomposition of Metal Halide Perovskite Optoelectronic Devices. *ACS Energy Lett.* **2016**, *1*, 595-602.
- (215) Carrillo, J.; Guerrero, A.; Rahimnejad, S.; Almora, O.; Zarazua, I.; Mas - Marza, E.; Bisquert, J.; Garcia - Belmonte, G. Ionic Reactivity at Contacts and Aging of Methylammonium Lead Triiodide Perovskite Solar Cells. *Adv. Energy Mater.* **2016**, *6*, 1502246.
- (216) Li, J.; Shan, X.; Bade, S. G. R.; Geske, T.; Jiang, Q.; Yang, X.; Yu, Z. Single-Layer Halide Perovskite Light-Emitting Diodes with Sub-Band Gap Turn-on Voltage and High Brightness. *J. Phys. Chem. Lett.* **2016**, *7*, 4059-4066.
- (217) Shan, X.; Li, J.; Chen, M.; Geske, T.; Bade, S. G. R.; Yu, Z. Junction Propagation in Organometal Halide Perovskite-Polymer Composite Thin Films. *J. Phys. Chem. Lett.* **2017**, *8*, 2412-2419.
- (218) Wang, X.; Ling, Y.; Chiu, Y.-C.; Du, Y.; Barreda, J. L.; Perez-Orive, F.; Ma, B.; Xiong, P.; Gao, H. Dynamic Electronic Junctions in Organic-Inorganic Hybrid Perovskites. *Nano Lett.* **2017**, *17*, 4831-4839.
- (219) Diroll, B. T.; Nedelcu, G.; Kovalenko, M. V.; Schaller, R. D. High-Temperature Photoluminescence of CsPbX_3 (X = Cl, Br, I) Nanocrystals. *Adv. Funct. Mater.* **2017**, *27*, 1606750.
- (220) Tian, Y.; Zhou, C.; Worku, M.; Wang, X.; Ling, Y.; Gao, H.; Zhou, Y.; Miao, Y.; Guan, J.; Ma, B. Highly Efficient Spectrally Stable Red Perovskite Light - Emitting Diodes. *Adv. Mater.* **2018**, *30*, 1707093.

- (221) Tsai, H.; Nie, W.; Blancon, J. C.; Stoumpos, C. C.; Soe, C. M. M.; Yoo, J.; Crochet, J.; Tretiak, S.; Even, J.; Sadhanala, A. Stable Light - Emitting Diodes Using Phase - Pure Ruddlesden-Popper Layered Perovskites. *Adv. Mater.* **2018**, *30*, 1704217.
- (222) Kim, Y.-H.; Wolf, C.; Kim, H.; Lee, T.-W. Charge Carrier Recombination and Ion Migration in Metal-Halide Perovskite Nanoparticle Films for Efficient Light-Emitting Diodes. *Nano Energy* **2018**, *52*, 329-335.
- (223) Sutherland, B. R.; Hoogland, S.; Adachi, M. M.; Kanjanaboos, P.; Wong, C. T.; McDowell, J. J.; Xu, J.; Voznyy, O.; Ning, Z.; Houtepen, A. J. Perovskite Thin Films Via Atomic Layer Deposition. *Adv. Mater.* **2015**, *27*, 53-58.
- (224) Xing, G.; Mathews, N.; Lim, S. S.; Yantara, N.; Liu, X.; Sabba, D.; Grätzel, M.; Mhaisalkar, S.; Sum, T. C. Low-Temperature Solution-Processed Wavelength-Tunable Perovskites for Lasing. *Nat. Mater.* **2014**, *13*, 476-480.
- (225) Sutherland, B. R.; Hoogland, S.; Adachi, M. M.; Wong, C. T.; Sargent, E. H. Conformal Organohalide Perovskites Enable Lasing on Spherical Resonators. *ACS nano* **2014**, *8*, 10947-10952.
- (226) Stranks, S. D.; Wood, S. M.; Wojciechowski, K.; Deschler, F.; Saliba, M.; Khandelwal, H.; Patel, J. B.; Elston, S. J.; Herz, L. M.; Johnston, M. B. Enhanced Amplified Spontaneous Emission in Perovskites Using a Flexible Cholesteric Liquid Crystal Reflector. *Nano Lett.* **2015**, *15*, 4935-4941.
- (227) Kao, T. S.; Chou, Y.-H.; Chou, C.-H.; Chen, F.-C.; Lu, T.-C. Lasing Behaviors Upon Phase Transition in Solution-Processed Perovskite Thin Films. *Appl. Phys. Lett.* **2014**, *105*, 231108.
- (228) Yakunin, S.; Protesescu, L.; Krieg, F.; Bodnarchuk, M. I.; Nedelcu, G.; Humer, M.; De Luca, G.; Fiebig, M.; Heiss, W.; Kovalenko, M. V. Low-Threshold Amplified Spontaneous Emission and Lasing from Colloidal Nanocrystals of Caesium Lead Halide Perovskites. *Nat. commun.* **2015**, *6*, 8056.
- (229) Wang, Y.; Li, X.; Song, J.; Xiao, L.; Zeng, H.; Sun, H. All-Inorganic Colloidal Perovskite Quantum Dots: A New Class of Lasing Materials with Favorable Characteristics. *Adv. Mater.* **2015**, *27*, 7101-7108.
- (230) Pan, J.; Sarmah, S. P.; Murali, B.; Dursun, I.; Peng, W.; Parida, M. R.; Liu, J.; Sinatra, L.; Alyami, N.; Zhao, C. Air-Stable Surface-Passivated Perovskite Quantum Dots for Ultra-Robust, Single-and Two-Photon-Induced Amplified Spontaneous Emission. *J. Phys. Chem. Lett.* **2015**, *6*, 5027-5033.
- (231) Eaton, S. W.; Lai, M.; Gibson, N. A.; Wong, A. B.; Dou, L.; Ma, J.; Wang, L.-W.; Leone, S. R.; Yang, P. Lasing in Robust Cesium Lead Halide Perovskite Nanowires. *Proceedings of the National Academy of Sciences* **2016**, *113*, 1993-1998.
- (232) Klimov, V. I. Spectral and Dynamical Properties of Multiexcitons in Semiconductor Nanocrystals. *Annu. Rev. Phys. Chem.* **2007**, *58*, 635-673.
- (233) Yuan, F.; Wu, Z.; Dong, H.; Xi, J.; Xi, K.; Divitini, G.; Jiao, B.; Hou, X.; Wang, S.; Gong, Q. High Stability and Ultralow Threshold Amplified Spontaneous Emission from Formamidinium Lead Halide Perovskite Films. *J. Phys. Chem. C* **2017**, *121*, 15318-15325.
- (234) Fu, Y.; Zhu, H.; Schrader, A. W.; Liang, D.; Ding, Q.; Joshi, P.; Hwang, L.; Zhu, X. Y.; Jin, S. Nanowire Lasers of Formamidinium Lead Halide Perovskites and Their Stabilized Alloys with Improved Stability. *Nano Lett.* **2016**, *16*, 1000-1008.

- (235) Shum, K.; Chen, Z.; Qureshi, J.; Yu, C.; Wang, J. J.; Pfenninger, W.; Vockic, N.; Midgley, J.; Kenney, J. T. Synthesis and Characterization of CsSnI₃ Thin Films. *Appl. Phys. Lett.* **2010**, *96*, 221903.
- (236) Lee, B.; He, J.; Chang, R. P.; Kanatzidis, M. G. All-Solid-State Dye-Sensitized Solar Cells with High Efficiency. *Nature* **2012**, *485*, 486-489.
- (237) Huang, L.-y.; Lambrecht, W. R. Electronic Band Structure, Phonons, and Exciton Binding Energies of Halide Perovskites CsSnCl₃, CsSnBr₃, and CsSnI₃. *Phys. Rev. B* **2013**, *88*, 165203.
- (238) Hao, F.; Stoumpos, C. C.; Cao, D. H.; Chang, R. P.; Kanatzidis, M. G. Lead-Free Solid-State Organic-Inorganic Halide Perovskite Solar Cells. *Nat. Photonics* **2014**, *8*, 489-494.
- (239) Chong, W. K.; Thirumal, K.; Giovanni, D.; Goh, T. W.; Liu, X.; Mathews, N.; Mhaisalkar, S.; Sum, T. C. Dominant Factors Limiting the Optical Gain in Layered Two-Dimensional Halide Perovskite Thin Films. *Phys. Chem. Chem. Phys.* **2016**, *18*, 14701-14708.
- (240) Li, M.; Wei, Q.; Muduli, S. K.; Yantara, N.; Xu, Q.; Mathews, N.; Mhaisalkar, S. G.; Xing, G.; Sum, T. C. Enhanced Exciton and Photon Confinement in Ruddlesden - Popper Perovskite Microplatelets for Highly Stable Low - Threshold Polarized Lasing. *Adv. Mater.* **2018**, *30*, 1707235.
- (241) Zhu, H.; Fu, Y.; Meng, F.; Wu, X.; Gong, Z.; Ding, Q.; Gustafsson, M. V.; Trinh, M. T.; Jin, S.; Zhu, X. Y. Lead Halide Perovskite Nanowire Lasers with Low Lasing Thresholds and High Quality Factors. *Nat. Mater.* **2015**, *14*, 636-642.
- (242) Zhang, Q.; Ha, S. T.; Liu, X.; Sum, T. C.; Xiong, Q. Room-Temperature near-Infrared High-Q Perovskite Whispering-Gallery Planar Nanolasers. *Nano Lett.* **2014**, *14*, 5995-6001.
- (243) Liao, Q.; Hu, K.; Zhang, H.; Wang, X.; Yao, J.; Fu, H. Perovskite Microdisk Microlasers Self-Assembled from Solution. *Adv. Mater.* **2015**, *27*, 3405-3410.
- (244) Jia, Y.; Kerner, R. A.; Grede, A. J.; Brigeman, A. N.; Rand, B. P.; Giebink, N. C. Diode-Pumped Organo-Lead Halide Perovskite Lasing in a Metal-Clad Distributed Feedback Resonator. *Nano Lett.* **2016**, *16*, 4624-4629.
- (245) Saliba, M.; Wood, S. M.; Patel, J. B.; Nayak, P. K.; Huang, J.; Alexander-Webber, J. A.; Wenger, B.; Stranks, S. D.; Horantner, M. T.; Wang, J. T. et al. Structured Organic-Inorganic Perovskite toward a Distributed Feedback Laser. *Adv. Mater.* **2016**, *28*, 923-929.
- (246) Chen, S.; Zhang, C.; Lee, J.; Han, J.; Nurmikko, A. High-Q, Low-Threshold Monolithic Perovskite Thin-Film Vertical-Cavity Lasers. *Adv. Mater.* **2017**, *29*, 1604781.
- (247) Jia, Y.; Kerner, R. A.; Grede, A. J.; Rand, B. P.; Giebink, N. C. Continuous-Wave Lasing in an Organic-Inorganic Lead Halide Perovskite Semiconductor. *Nat. Photonics* **2017**, *11*, 784-788.
- (248) Gong, X.; Voznyy, O.; Jain, A.; Liu, W.; Sabatini, R.; Piontkowski, Z.; Walters, G.; Bappi, G.; Nokhrin, S.; Bushuyev, O. Electron-Phonon Interaction in Efficient Perovskite Blue Emitters. *Nat. Mater.* **2018**, *17*, 550-556.